A Method for Computing Horizontal Pressure-Gradient Force in an Oceanic Model with a Non-Aligned Vertical Coordinate

Alexander F. Shchepetkin and James C. McWilliams

Institute of Geophysics and Planetary Physics, University of California at Los Angeles,
405 Hilgard Avenue, Los Angeles, CA 90095-1567 e-mail: *alex@atmos.ucla.edu* *jcm@atmos.ucla.edu*

Abstract. Discretization of the pressure-gradient force is a long-standing problem in terrain-following (or σ) coordinate oceanic modeling. When the isosurfaces of the vertical coordinate are not aligned with either geopotential surfaces or isopycnals, the horizontal pressure gradient consists of two large terms that tend to cancel; the associated pressure-gradient error stems from interference of the discretization errors of these terms. The situation is further complicated by the non-orthogonality of the coordinate system and by the common practice of using highly non-uniform stretching for the vertical grids, which, unless special precautions are taken, causes both a loss of discretization accuracy overall and an increase in interference of the component errors. In the present study we design a pressure-gradient algorithm which achieves more accurate hydrostatic balance between the two components and does not lose as much accuracy with non-uniform vertical grids at relatively coarse resolution. This algorithm is based on the reconstruction of the density field and the physical z-coordinate as continuous functions of transformed coordinates with subsequent analytical integration to compute the pressure-gradient force. This approach allows not only a formally higher order of accuracy, but it also retains and expands to high orders several important symmetries of the original second-order scheme (Mellor *et al*, 1994, Song, 1998), which is used as a prototype, as well as it has build-in monotonicity constraining algorithm which prevents appearance of spurious oscillations of polynomial interpolant, and, consequently, insures numerical stability and robustness of the model under the conditions of non-smooth density field and coarse grid resolution. We further incorporate an alternative method of dealing with compressibility of seawater which escapes pressure-gradient errors associated with interference of the nonlinear nature of equation of state and difficulties to achieve accurate polynomial fits of resultant *in situ* density profiles. In doing so, we generalized the monotonicity constraint to guarantee non-negative physical stratification of the reconstructed density profile in the case of compressible equation of state. To verify the new method, we perform traditional idealized (Seamount) and realistic test problems.

keywords:	sigma-coordinate pressure gradient error	compressibility of seawater
	high-order, monotonic interpolation	adiabatic differencing

AGU index terms:	4255	Numerical modeling
	4528	Fronts and jets
	4271	Physical and chemical properties of seawater
	4532	General circulation

Received 3 July 2001; revised 20 August 2002; accepted 5 September 2002; published 20 March 2003.

Citation: Shchepetkin, A. F., and J. C. McWilliams, A method for compu ting horizontal pressure-gradient force in an oceanic model with a non aligned vertical coordinate, *J. Geophys. Res.,* 108(C3), 3090, doi:10.1 029/2001JC001047, 2003.

1. Introduction

Discrete approximation of horizontal pressure-gradient force (PGF) topography-following coordinates has been a long-standing problem in atmospheric and oceanic modeling (Gary, 1973; Mesinger & Arakawa, 1976; Janjic, 1977; Mesinger, 1982; Arakawa & Suarez, 1983; Mesinger & Janjic, 1985; Michailovich & Janjic, 1986; Blumberg & Mellor, 1987; Haney, 1991; Mellor *et al*, 1994; Stelling & van Kester, 1994; Song & Haidvogel, 1994; Lin, 1997, 1998; Slordal, 1997; Janjic, T., 1998; Mellor *et al*, 1998; Song, 1998; Song & Wright, 1998; Kliem & Pietrzak, 1999). The main difficulty is attributed to *hydrostatic inconsistency*, i.e., failure of the discretized PGF to vanish in the case when isopycnals are horizontal. This effect causes spurious geostrophically balanced flows, which in oceanic model applications may be as large as 10 cm/s or more, degrading the quality of the solution beyond an acceptable limit. The problem arises from the deviation of quasi-horizontal coordinates from either geopotential or isopycnal surfaces, so that the PGF in the momentum equations appears in the form of two large terms which tend to cancel each other,

$$-\frac{1}{\rho_0}\frac{\partial P}{\partial x}\bigg|_z = -\frac{1}{\rho_0}\frac{\partial P}{\partial x}\bigg|_s + \frac{1}{\rho_0}\cdot\frac{\partial P}{\partial z}\cdot\frac{\partial z}{\partial x}\bigg|_s , \qquad (1.1)$$

where P is pressure, $\rho_0 = \text{const}$ is mean density in a Boussinesq approximation, and z is vertical coordinate in non-transformed (i.e., physical) space. Subscript z in $\partial/\partial x|_z$ means that the associated partial derivative is computed with respect to a constant geopotential surface, $z = \text{const}$, and a similar subscript s means that the differentiation is performed along the transformed coordinate surface, $s = \text{const}$.

In the present study we are not limited to the traditional σ-coordinate,

$$z(x,y,\sigma) = h(x,y)\cdot f(\sigma)\,, \qquad -1 \le \sigma \le 0\,, \qquad (1.2)$$

where $h(x,y)$ is oceanic bottom depth, and $f(\sigma)$ is a monotonic mapping function independent of horizontal coordinates that controls vertical-coordinate (hence grid) stretching. Instead we assume that the three-dimensional mapping function $z = Z(x,y,s,t)$ is both monotonic (i.e., $\partial Z\big/\partial s > 0$) and nonseparable, while usually

$$\frac{\partial Z}{\partial x}\bigg|_s \ne 0\,. \qquad (1.3)$$

Moreover, it is assumed that (1.1) may be stiff in the sense that

$$\epsilon \equiv \frac{\left|\frac{\partial P}{\partial x}\big|_s - \frac{\partial P}{\partial z}\cdot\frac{\partial z}{\partial x}\big|_s\right|}{\left|\frac{\partial P}{\partial x}\big|_s\right| + \left|\frac{\partial P}{\partial z}\cdot\frac{\partial z}{\partial x}\big|_s\right|} \ll 1\,, \qquad (1.4)$$

which indicates that special precautions need to be taken to avoid loss of accuracy [1].

P is computed from the hydrostatic equation,

$$P(x,y,z) = g\int_z^{\zeta}\rho(x,y,z')\mathrm{d}z'\,, \qquad (1.5)$$

where $\rho(x,y,z)$ is density; ζ is free-surface elevation; and g is gravitational acceleration. One might be tempted to replace (1.1) with

$$-\frac{1}{\rho_0}\frac{\partial P}{\partial x}\bigg|_z = -\frac{1}{\rho_0}\frac{\partial P}{\partial x}\bigg|_s - \frac{g\rho}{\rho_0}\cdot\frac{\partial z}{\partial x}\bigg|_s , \qquad (1.6)$$

and discretize it in a straightforward way using second-order averaging and differencing operators. This was shown to be prone to hydrostatic consistency error (cf., Mesinger & Arakawa, 1976), caused mainly by the vertical averaging of P and horizontal averaging of ρ in (1.6) in order to co-locate them with horizontal velocity components on a staggered grid.

Practical experience has resulted in essentially two approaches to overcome this problem:

(i) In each vertical column compute a set of values of pressure $P_{k+\frac{1}{2}}$ naturally located half-way between the density points on a staggered vertical grid; then for each two neighboring columns, interpolate this P field to an appropriate common geopotential level; and then subtract the interpolated values. Note, that after computation of P, the density field ρ_k does not participate in any further computation. Obviously, in this approach the two terms in (1.1) become inseparable. The different methods of this family may vary in details of the choice of the common level as well as interpolation technique, which is linear in most cases (Janjic, 1977; Arakawa & Suarez, 1983; Lin, 1997) or parabolic (Michailovich & Janjic, 1986). Overall, the overwhelming majority of atmospheric models use schemes belonging to this class.

(ii) Following Blumberg & Mellor, 1987, and Song, 1998, Eqs. (1.1)—(1.5) are first transformed into

$$-\frac{1}{\rho_0}\frac{\partial P}{\partial x}\bigg|_z = -\frac{1}{\rho_0}\frac{\partial P}{\partial x}\bigg|_{z=\zeta} - \frac{g}{\rho_0}\int_z^{\zeta}\frac{\partial\rho}{\partial x}\bigg|_z \mathrm{d}z' \qquad (1.7)$$

$$= -\frac{g\rho(\zeta)}{\rho_0}\frac{\partial\zeta}{\partial x} - \frac{g}{\rho_0}\int_z^{\zeta}\left[\frac{\partial\rho}{\partial x}\bigg|_s - \frac{\partial\rho}{\partial z'}\,\frac{\partial z'}{\partial x}\bigg|_s\right]\mathrm{d}z'\,,$$

[1] We will use the terminology of σ-coordinate and σ-modeling throughout this paper in a broad sense referring to the whole class of models with a non-aligned vertical coordinate

where the expression in square brackets is similar to (1.1), except that P is replaced with ρ. Eq. (1.7) is then discretized in a manner similar to that described above, except that now vertical integration becomes the second step rather than the first and P never appears explicitly in the model. Because of the form of (1.7), these methods are often referred as *density-Jacobian*, opposite to the *pressure-Jacobian* family described above. The PGF schemes in two commonly used terrain-following oceanic models (POM and SCRUM)[2] belong to this class.

Song, 1998, and Song & Wright, 1998, argue that a density-Jacobian method is inherently more accurate than a pressure-Jacobian. Indeed, it is easy to see that, if the basic second-order approximations (2-point differencing, interpolation and trapezoidal integration) are used and if ρ is a linear function of z, then the error of a density-Jacobian method vanishes identically, while a linear ρ corresponds to a quadratic P; therefore, discretizations based on a linear fit for P (cf., Janjic, 1977, Lin, 1997, Janjic, T., 1998) are not able to capture this correctly resulting in hydrostatic error for this particular profile. On the other hand, Lin, 1997, argues that it is advantageous to discretize PGF using a finite-volume method. An attractive feature of this approach is that the discretized PGF naturally appears in flux-divergent form, which makes the proof of momentum and bottom-torque consistency [cf., Arakawa & Suarez, 1983; Song & Wright, 1998] simple. There is no obvious way to cast a density-Jacobian scheme into the form of a difference of P fluxes. This conflict between accuracy and conservation properties of σ-coordinate PGF schemes is not unnoticed in the literature (e.g., Beckmann & Haidvogel, 1993; Song & Wright, 1998). It is also not surprising that oceanic models tend to use density-Jacobian, while atmospheric models use pressure-Jacobian. In comparison with the atmosphere, the ocean is often more strongly stratified, and the stratification is much more spatially variable: it is not unusual to see a change of Brunt-Väisäla frequency by two orders of magnitude throughout a vertical column. While most of the vertical density gradient in atmospheric models is due to the compressibility effect, which may be absorbed by special mapping techniques as well as by the choice of vertical coordinate system (e.g., pressure instead of geopotential; Arakawa & Suarez, 1983), the relative complexity of the equation of state for seawater makes such procedures much harder in oceanic models, shifting the priority toward an accurate representation of $\rho(z)$ profiles and a preference for the density-Jacobian.

[2]POM – Princeton Ocean Model, Blumberg & Mellor, 1987; SCRUM – S-Coordinate Rutgers University Model, Song & Haidvogel, 1994.

The high-order PGF schemes available to date follow the path of straightforward discretization of (1.6) using a spectral method in the vertical direction in combination with either conventional or compact forth-order finite differences and interpolations in the horizontal (McCalpin, 1994) or spectral in combination with compact differencing up to sixth-order accuracy (Chu & Fan, 1997, 1998). The approach relies exclusively on the smallness of the truncation errors of the elementary discretizations (computation of the first derivative and mid-point interpolation), which is justifiable only when the density field is smooth on the grid scale. This is reasonably successful for idealized test problems, but practically useless for real-world simulations where fields are not smooth on affordable grids. A comprehensive comparison of performance of schemes available to date may be found in Kliem & Pietrzak, 1999, for various test problems. Although one might argue, that the analytical density profiles used in this reference are discontinuous in the first derivatives, and therefore the posedness of the problem is prejudicial against high-order methods, their inherent nonrobustness is consistent with the more general experience in realistic basin-scale simulations, resulting in the fact that, to our best knowledge, to date none of such simulations were performed using PGF scheme of higher than the basic second-order accuracy.

In the present study we describe the symmetry properties of the second-order density-Jacobian scheme and analyze sources of numerical errors. We then seek a high-order accuracy extension to this method which retains most of the symmetries and is both accurate and robust in situations where ρ changes sharply from one grid point to another with nonuniformly stretched grids. The methodology we employ is based on the reconstruction of both ρ and z as continuous functions of the transformed coordinates, which are then analytically integrated along the contours bounding the grid cells surrounding the velocity components. Since, in this approach, all steps after ρ reconstruction are exact (since ρ is treated as a continuous analytical function), the resultant algorithm can be equivalently reformulated in either Jacobian (1.7) or σ-coordinate primitive form (1.6) (reflecting the fact that these two are equivalent at the level of continuous equations), which in effect disproves the long-standing belief that a Jacobian formulation is inherently more accurate.

2. Second-order Density Jacobian

The density-Jacobian discretization is based on a continuous expression for the PGF,

$$-\left.\frac{\partial P}{\partial x}\right|_z = -\rho_s g\frac{\partial \zeta}{\partial x} - g\int_z^{\zeta} \mathcal{J}(\rho,z)ds\,, \tag{2.1}$$

where

$$\mathcal{J}(\rho,z) = \left.\frac{\partial \rho}{\partial x}\right|_s \frac{\partial z}{\partial s} - \frac{\partial \rho}{\partial s}\left.\frac{\partial z}{\partial x}\right|_s, \tag{2.2}$$

ζ is free-surface elevation, ρ_s is density at the surface, and g is acceleration of gravity. POM/SCRUM use the most straightforward second-order accuracy method to approximate (2.2) [3],

$$\begin{aligned}-\Delta x\Delta s\;\mathcal{J}(\rho,z) = \frac{1}{4}\,[&(\rho_1+\rho_2-\rho_3-\rho_4)\\ &\times(z_2-z_1+z_4-z_3)\\ &-(\rho_2-\rho_1+\rho_4-\rho_3)\\ &\times(z_1+z_2-z_3-z_4)]\,,\end{aligned} \tag{2.3}$$

where placement of values with indices 1,2,3,4 is shown on Fig. 1. Since (2.3) treats ρ and z in a symmetric way, it has the property of antisymmetry,

$$\mathcal{J}(\rho,z) = -\mathcal{J}(z,\rho)\,, \tag{2.4}$$

and, obviously, it vanishes identically if ρ is a linear function of z.

This discretization can be rewritten in four algebraically equivalent forms **(i)**–**(iv)**:

(i) "Diagonal" Jacobian:

$$\begin{aligned}-\Delta x\Delta s\;\mathcal{J}(\rho,z) = \frac{1}{2}\,[&(\rho_2-\rho_3)(z_4-z_1)\\ &+(\rho_1-\rho_4)(z_2-z_3)]\,,\end{aligned} \tag{2.5}$$

(ii) Horizontal (along-geopotential) differencing of ρ linearly interpolated or extrapolated within each vertical column to a common level z_*:

$$-\Delta x\Delta s\;\mathcal{J}(\rho,z) = \mathcal{A}\left(\rho_*^L - \rho_*^R\right)\,, \tag{2.6}$$

where

$$\mathcal{A} = \Delta x\frac{z_2-z_1+z_4-z_3}{2} \tag{2.7}$$

is the area of trapezoidal element (z_1,z_3,z_4,z_2),

$$\rho_*^L = \frac{\rho_1(z_2-z_*)+\rho_2(z_*-z_1)}{z_2-z_1}$$

$$\rho_*^R = \frac{\rho_3(z_4-z_*)+\rho_4(z_*-z_3)}{z_4-z_3}\,,$$

[3]Here we follow notation of Song, 1998. Eq. (5) from Mellor *et al*, 1994 becomes equivalent to (2.3) after it is recognized that $z_{i,k} = H_i\sigma_k$ in their notation.

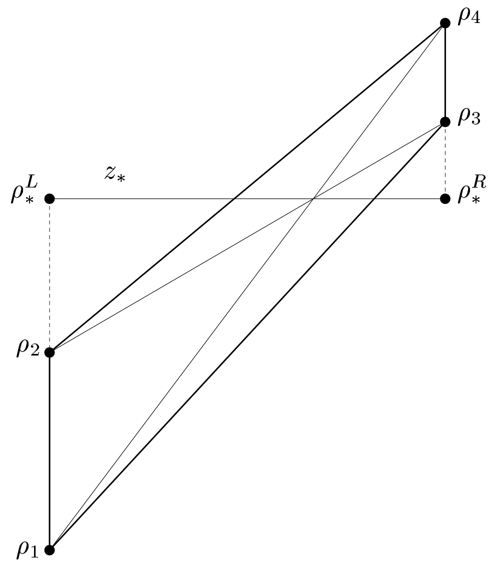

Figure 1. An elementary computational stencil of POM density Jacobian.

and

$$z_* = \frac{z_4z_2 - z_3z_1}{z_4-z_3+z_2-z_1}\,, \tag{2.8}$$

which coincides with the level of intersection of diagonals of trapezoidal element (Fig. 1). This choice of z_* also has the property,

$$\frac{z_*-\frac{1}{2}(z_1+z_2)}{z_2-z_1} = \frac{\frac{1}{2}(z_3+z_4)-z_*}{z_4-z_3}\,, \tag{2.9}$$

which implies that offsets from mid-level to z_* are proportional to grid-box height in each vertical column of ρ locations. The possibility to rewrite (2.3) into (2.6)–(2.8) indicates that, unlike stated in Mellor *et al*, 1994, 1998, and Song, 1998, Jacobian formulation by itself does not offer any relief from violation of hydrostatic consistency condition (Haney, 1991) when

$$r_x = \frac{z_4+z_3-z_2-z_1}{z_4-z_3+z_2-z_1} > 1 \tag{2.10}$$

becomes greater than one and vertical interpolation of ρ turns into extrapolation. However, this choice of z_* delays this moment as much as possible among all possible schemes using the stencil shown on Fig. 1, since proportionality (2.9) makes the transition from interpolation to extrapolation occur at the same time for both left and right vertical columns at ρ locations. (Any choice of z_* other than (2.8) would cause the transition to occur earlier at one end.) Note that violation of the hydrostatic consistency criterion (2.10) does not mean immediate hydrostatic instability because after vertical integration of

$\mathcal{J}(\rho,z)$ is performed, the overall PGF scheme retains positive definiteness in sense that the addition of a positive ρ perturbation at any point on one side and above the velocity point at which the PGF is evaluated always causes an increment in PGF directed away from that side, as it should be; instead it merely degrades the accuracy of the scheme. Another consequence of (2.9) is the effect of cancellation of hydrostatic error if either $z_2 = z_3$ or $z_1 = z_4$, (cf., Mellor *et al*, 1998); in this case, z_* is equal to common value of $z_2 = z_3$ or $z_1 = z_4$, and ρ interpolation to z_* becomes exact. This property is also obvious from the diagonal form (2.5).

(iii) "Pseudo-flux" form:

$$-\Delta x \Delta s\ \mathcal{J}(\rho,z) = F_{21} + F_{42} - F_{43} - F_{31}\ , \qquad (2.11)$$

where

$$\begin{aligned} F_{21} &= \frac{\rho_1+\rho_2}{2}\,(z_2-z_1) \\ F_{42} &= \frac{\rho_2+\rho_4}{2}\,(z_4-z_2) \\ F_{43} &= \frac{\rho_3+\rho_4}{2}\,(z_4-z_3) \\ F_{31} &= \frac{\rho_1+\rho_3}{2}\,(z_3-z_1)\ , \end{aligned} \qquad (2.12)$$

are called fluxes because they are shared by two grid elements adjacent either in horizontal or vertical direction. This form is not equivalent to a true finite-volume flux form (Lin, 1997), where the net force applied to a control volume element around velocity point is expressed as sum of P fluxes applied to all facets of the element; e.g., (2.11)–(2.12) does not have property that summation of PGFs applied to adjacent velocity elements can be expressed in terms of integral along the outer surface enclosing all elements included into summation. The rewriting of (2.3) into (2.11) is a discrete analog of Green's theorem,

$$\iint_{\mathcal{A}} \mathcal{J}(\rho,z)\,dx\,ds = \oint \rho(\mathbf{k},\mathbf{l})dl\,, \qquad (2.13)$$

or, more simply,

$$\iint_{\mathcal{A}} \left.\frac{\partial \rho}{\partial x}\right|_z dx\,dz = \oint \rho\,\mathbf{dz}\,, \qquad (2.14)$$

where $\mathbf{k}$ is the unit vector pointing in positive z-direction (upward) and $\mathbf{l}$ is unit vector along the contour of trapezoidal element. Eqs. (2.11)–(2.12) can be viewed as trapezoidal rule approximation to (2.14), which leads to graphical explanation of leading-order hydrostatic error second-order Jacobian resulting from terms associated with second vertical derivative of ρ (Fig. 2).

(iv) σ-coordinate primitive form:

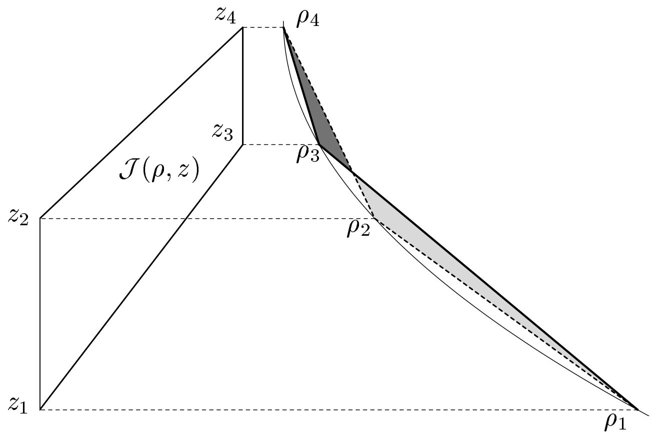

Figure 2. Explanation of appearance of hydrostatic error of second-order density-Jacobian scheme: Eqs (2.12) assume that density is distributed linearly along each edge of the trapezoidal element shown on the left. If, in contrast, density is a quadratic function of z shown as smooth curve on the right, the trapezoidal segments do not conicide with the true profile leading to a noncancellation error which appears as the difference between dark and light shaded areas, which is the difference of areas left from the solid and dashed thick lines respectively. (Note that error cancels out if $z_2 = z_3$, despite the fact that there are still errors of integral approximation along each side taken separately.)

Since F_{21} and F_{43} involve points only within their respective vertical columns and, since during vertical summation of $\mathcal{J}(\rho,z)$ cancellations occur such that only the first and the last vertical fluxes are present in the resultant expression for PGF, one can rearrange the order of operation of vertical integration and horizontal differencing and evaluate P at all $\rho_{i,k}$ locations first, using

$$P_{i,k} = P_{i,N} + g\sum_{k'=k}^{N-1} \frac{\rho_{i,k'}+\rho_{i,k'+1}}{2}\,(z_{i,k'+1}-z_{i,k'})\ , \qquad (2.15)$$

then

$$\begin{aligned} -\left.\frac{\partial P}{\partial x}\right|_z &= \frac{P_{i,k}-P_{i+1,k}}{\Delta x} \\ &\quad - g\frac{\rho_{i,k}+\rho_{i+1,k}}{2}\cdot\frac{z_{i+1,k}-z_{i,k}}{\Delta x}\,. \end{aligned} \qquad (2.16)$$

This shows that density Jacobian is just a special form of straightforward discretization of σ-coordinate PGF that naturally appears to be in the form of a P derivative along a σ surface and compensating hydrostatic term, which is the product of ρ and coordinate slope[4].

In (2.15) $P_{i,N}$ is pressure in the middle of the topmost grid box, where a special formula must be used (simi-

[4] A B-grid version of (2.15)–(2.16) appears in Gerdes, 1993, which in effect brings that study into the framework discussed here.

larly, PGF at the topmost grid box cannot be computed via regular Jacobian scheme because this would require values of ρ above or at the surface that are not available). POM/SCRUM simply use the nearest available value $\rho_{i,N}$,

$$P_{i,N} = g\rho_{i,N}\left(\zeta_i - z_{i,N}\right) \,, \tag{2.17}$$

which is equivalent to the assumption that ρ is vertically uniform within the topmost grid box. In terms of the resultant PGF at the topmost grid box, this assumption neglects the hydrostatic compensation term, effectively neglecting the σ-coordinate slope within the topmost grid box. A more accurate treatment of the topmost grid box is given by (A.21) in Appendix A.

Representation of (2.3) in pseudo-flux form (2.11)–(2.12) and in σ-coordinate primitive form opens the possibility to proof that a model which uses this PGF discretization and a second-order centered advection scheme for the density equation is energetically consistent in the sense that it conserves exactly the sum of discrete kinetic and potential energy (Song & Wright, 1998). This property is often invoked as useful for long-term stability of integration. The practical usefulness of this property, as well as the possibility to extend its proof to higher orders of accuracy, will is discussed later.

3. Weighted Jacobian of Song (1998)

Song (1998) proposes replacing equal-weight vertical averages in (2.3) with weighting according to

$$\begin{aligned} -\Delta x\Delta s\ \mathcal{J}(\rho,z) = \frac{1}{2}\,&[(\alpha\rho_1+\beta\rho_2-\alpha\rho_3-\beta\rho_4) \\ &\qquad\times(z_2-z_1+z_4-z_3) \\ &-(\rho_2-\rho_1+\rho_4-\rho_3) \\ &\qquad\times(\alpha z_1+\beta z_2-\alpha z_3-\beta z_4)]\,, \end{aligned} \tag{3.1}$$

where α and $\beta\equiv 1-\alpha$ are chosen from the condition that the scheme is able to produce exact dynamic PGF at the location

$$z_C = \frac{z_1+z_2+z_3+z_4}{4} \tag{3.2}$$

if ρ is a bi-linear function of x and z. This choice results in $\alpha=\frac{1}{2}-\epsilon$, $\beta=\frac{1}{2}+\epsilon$, where

$$\epsilon = \frac{(z_4+z_3-z_2-z_1)\,(z_4-z_3-z_2+z_1)}{8\,(z_4-z_3)\,(z_2-z_1)}\,, \tag{3.3}$$

which is (2.15) from Song, 1998, rewritten in our notation.

The weighting (3.1) destroys the antisymmetry property (2.4) of the original Jacobian, as well as the possibility to rewrite it into diagonal, pseudo-flux, and *sigma*-coordinate primitive forms. Hence, it is no longer possible

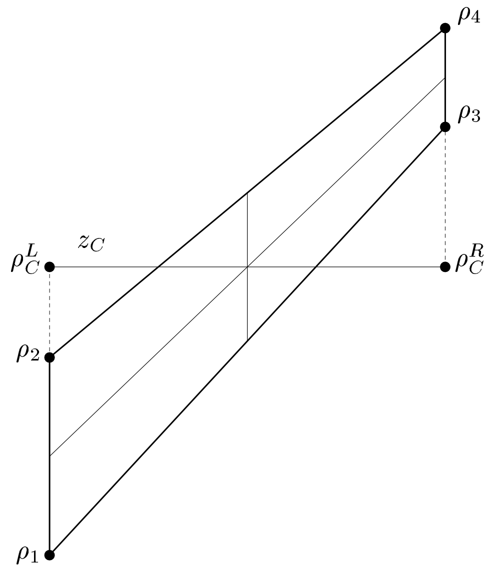

Figure 3. Explanation of Weighted Jacobian of Song (1998): at each side density is interpolated or extrapolated linearly toward common level z_C, which is chosen to be at the midlevel, after which the interpolated values are differenced horizontally.

to prove energetic consistency in a manner similar to Song & Wright, 1998. Also lost is the property of hydrostatic error cancellation when $z_2=z_3$ or $z_1=z_4$. However, the property of zero error if ρ is linear function of z is maintained. Examination of (3.3) reveals that the scheme is equivalent to (2.6)–(2.8), when z_* is replaced with z_C, the derivation of which is evident from Fig. 3.

In retrospect one can conclude that the original equally-weighted Jacobian evaluates the horizontal (along-geopotential) ρ gradient exactly at level z_*, which is the level of intersection of diagonals, if ρ is a bi-linear function of x and z. Therefore, contrary to the claim of Song, 1998, weighted Jacobian does not offer any theoretical advantage over the standard Jacobian in the case where a more general ρ perturbation is present; instead, these two schemes correspond to just two *ad hoc* choices for the common level z_* (or z_C) to which ρ is interpolated before horizontal differencing, and they both are exact in special cases described above.

4. Sensitivity to Choice of z_*: Seamount Test Problem

One might guess that the difference between standard and weighted Jacobians is minor, because it is nothing more than a particular choice of the common level z_*, and

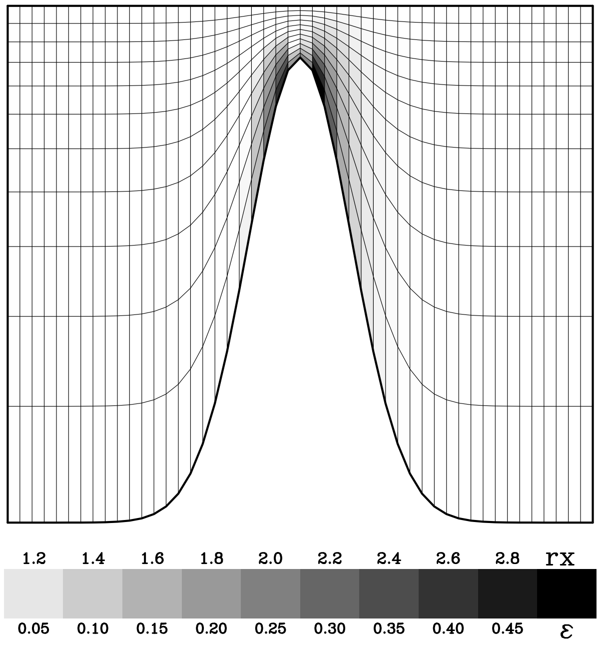

Figure 4. Vertical crossection of grid for the seamount test problem. On the left half of the plot, elements where hydrostatic consistency criterion is violated are shaded according to their value of r_x defined by (2.10), and color scheme below (with corresponging values shown above color bar). Shading on the right half of the plot shows values of geometric parameter ϵ defined by (3.3).

neither one has obvious advantage. It turns out that this is not the case, and the choice of z_* produces a significant effect in practice. To illustrate this we set up a seamount test problem and run test cases corresponding to different choices of common level according to

$$z_\gamma = (1-\gamma)z_* + \gamma z_C \,, \tag{4.1}$$

where $\gamma = \{0, 0.1, 0.2, \ldots 0.9, 1\}$; if $\gamma = 0$, the scheme is equivalent to the original Jacobian, while if $\gamma = 1$, it becomes the weighted Jacobian. The seamount problem set up is similar to that of Beckmann & Haidvogel, 1993, Chu & Fan, 1997, Mellor *et al*, 1998, and Song, 1998, with a few exceptions specified below.

The bottom topography is defined as

$$h(x,y) = D_0 - H \exp\left\{\frac{x^2+y^2}{L^2}\right\} \tag{4.2}$$

where $D_0 = 5000\,m$ is the depth far away from the seamount; $H = 4500\,m$ and $L = 40\,km$ are the seamount height and width, respectively; and the model domain is $320 \times 320\,km$ wide and has horizontal boundary conditions of periodicity in x and walls in y. An f-plane approximation is made with Coriolis frequency $10^{-4}\,s^{-1}$.

The uniform horizontal grid resolution for the base case is 48×48, implying $6.7\,km$ grid spacing. The vertical resolution for the base case is 11 non-uniformly spaced σ-levels generated by the transformation (Song & Haidvogel, 1994),

$$Z(x,y,\sigma) = \sigma h_{\min} + C(\sigma)\,(h(x,y) - h_{\min}) \,, \tag{4.3}$$

where

$$C(\sigma) = (1-\theta_b)\frac{\sinh(\theta\sigma)}{\sinh(\theta)} + \frac{1}{2}\theta_b\left[\frac{\tanh[\theta(\sigma+1/2)]}{\tanh(\theta/2)} - 1\right] ,$$

$-1 \le \sigma \le 0$ is discretized uniformly, and θ and θ_b are two non-dimensional parameters controlling the vertical coordinate stretching. In all calculations performed here we use values $\theta = 3$, $\theta_b = 0$ and $h_{\min} = 500\,m$, which results in violation of hydrostatic consistency (2.10) with a maximum value

$$r_{\max} = 2.4 \tag{4.4}$$

(this is comparable to, but somewhat smaller than that used in Song, 1998, and Mellor *et al*, 1998). A vertical cross-section of the grid and distributions of r_x and geometric parameter ϵ defined by (3.3) are shown in Fig. 4. Since ϵ is well correlated with r_x, it is naturally expected that method of Song, 1998 deviates most from the original Jacobian where r_x is the largest. Fig. 4 also shows that in such places biases from equal weighting in (3.1) may be significant, especially where vertical interpolation turns into extrapolation. To examine further this correlation we note that

$$\frac{\epsilon}{r_x} = \frac{(z_4-z_3)^2 - (z_2-z_1)^2}{8\,(z_4-z_3)\,(z_2-z_1)} = \frac{\Delta z_R^2 - \Delta z_L^2}{8\Delta z_R \Delta z_L} \,, \tag{4.5}$$

where Δz_L and Δz_R are grid-box heights on the left and right sides of the trapezoidal element. In the case of a separable σ-coordinate, these two are proportional to total depth D, hence

$$\frac{\epsilon}{r_x} = \frac{D_R^2 - D_L^2}{8 D_R D_L} \approx \frac{1}{2}\cdot\frac{D_R - D_L}{D_R + D_L} = \frac{1}{2} r_D \,, \tag{4.6}$$

where the approximation is valid as long as $D_R - D_L \ll D_R + D_L$. The expression on the right is recognized as the topographic-stiffness ratio (Beckmann & Haidvogel, 1993) which relates change in topography per horizontal grid point to locally averaged depth. Since this ratio proportionally decreases with increase of horizontal resolution and r_x stays the same as long as refinements of vertical and horizontal grids are proportional, one can see that ϵ decreases with grid refinement, which means that coefficients of weighted Jacobian asymptotically converge to that of the original one. This also means that in the seamount experiments, extreme values of ϵ occur on the coarsest grid and decline with refinement.

The initial ρ profile is defined by

$$\rho(z) = 3e^{z/\delta}\,, \quad -h(x,y) \le z \le 0\,, \tag{4.7}$$

where, as in the more oceanographically realistic study of Beckmann & Haidvogel, 1997, we chose $\delta = 500\,m$ which results in twice as steeper stratification of ρ in comparison with previous idealized studies cited above. Eq. (4.7) results in a Burger number,

$$S = \frac{\sqrt{gh\cdot\Delta\rho/\rho}}{fL} \approx \frac{\left(9.81\cdot 5\times 10^3\cdot 3/10^3\right)^{1/2}}{10^{-4}\cdot 40\times 10^3} \approx 3.1\,, \tag{4.8}$$

which is a typical midrange value among those used in Beckmann & Haidvogel, 1993, Mellor *et al*, 1998.

A horizontal Laplacian viscosity is set to $50\,m^2/s$ in all calculations presented here. This value is chosen to be comparable with that used in realistic simulations at similar resolution, and it is 40 times smaller that reported in Mellor *et al*, 1998, and 10 times smaller than in Song, 1998. Vertical viscosity, and horizontal and vertical diffusivities for tracers are all set to zero.

Tracer advection (here for ρ) is discretized using monotonized, fourth-order, centered scheme, i.e., in order to compute advective flux at the velocity component location $u_{i+\frac{1}{2},j,k}$, we use an interpolation scheme,

$$\rho_{i+\frac{1}{2},j,k} = \frac{\rho_{i,j,k}+\rho_{i+1,j,k}}{2} - \frac{\delta\rho_{i+1,j,k}-\delta\rho_{i,j,k}}{6}\,, \tag{4.9}$$

where $\delta\rho_{i,j,k}$ is mean slope defined at the location of $\rho_{i,j,k}$ using a harmonic average,

$$\delta\rho_{i,j,k} = \frac{2\Delta\rho_{i+\frac{1}{2},j,k}\Delta\rho_{i-\frac{1}{2},j,k}}{\Delta\rho_{i+\frac{1}{2},j,k}+\Delta\rho_{i-\frac{1}{2},j,k}}\,, \tag{4.10}$$

if $\Delta\rho_{i+\frac{1}{2},j,k}$ and $\Delta\rho_{i-\frac{1}{2},j,k}$ have the same sign and

$$\delta\rho_{i,j,k} = 0\,, \tag{4.11}$$

if the signs are different, and

$$\Delta\rho_{i+\frac{1}{2},j,k} = \rho_{i+1,j,k} - \rho_{i,j,k} \tag{4.12}$$

are elementary differences of ρ. Obviously, if (4.10) is replaced with algebraic mean of $\Delta\rho_{i+\frac{1}{2},j,k}$ and $\Delta\rho_{i-\frac{1}{2},j,k}$, then (4.9) becomes equivalent to a more familiar fourth-order interpolation scheme,

$$\rho_{i+\frac{1}{2},j,k} = \frac{-\rho_{i-1,j,k}+7\rho_{i,j,k}+7\rho_{i+1,j,k}-\rho_{i+2,j,k}}{12}\,. \tag{4.13}$$

The use of (4.10) guarantees that the averaged value of slope never exceeds twice the smaller of the two adjacent elementary differences. It also makes the interpolated value $\rho_{i+\frac{1}{2},j,k}$ be always between $\rho_{i,j,k}$ and $\rho_{i+1,j,k}$ regardless of sharp changes in the slope of the interpolated field (cf., van Leer, 1977). In places where the advected field $\rho_{i,j,k}$ is sufficiently smooth, these consecutive differences are comparable, and the difference between algebraic and harmonic means disappears, making the scheme behave like a fourth-order accurate scheme. In the next section we will discuss the effect of using harmonic averaging in more detail. The ρ advection used here is non-dissipative, since neither explicit diffusion nor an upstream-biased advection scheme is used.

The present setup differs substantially from all similar previous studies in two aspects:

- We do not subtract any background $\rho(z)$ profile when computing PGF; rather the full *in situ* ρ is used.
- Our primary criterion in evaluating the results is not the initial hydrostatic error, but rather long-term behavior of the solution. Therefore we carry out all our test runs to relatively large time of 6 months, which is sufficient to ensure that there is no further error growth (typically the duration of the test runs was 5, 10, 20 and 30 days in the previous studies cited here).

In our seamount experiment we compute time of histories the following quantities:

kinetic energy,

$$\mathcal{E}_{\text{kin}} = \frac{1}{2\mathcal{V}}\sum_{i,j,k}\Big[\Delta\mathcal{V}_{i+\frac{1}{2},j,k}u^2_{i+\frac{1}{2},j,k} + \Delta\mathcal{V}_{i,j+\frac{1}{2},k}v^2_{i,j+\frac{1}{2},k}\Big]\,, \tag{4.14}$$

barotropic kinetic energy fraction,

$$f_{\text{bar}} = \mathcal{E}_{\text{bar}}/\mathcal{E}_{\text{kin}}\,, \tag{4.15}$$

where $\mathcal{E}_{\text{bar}}$ is barotropic kinetic energy,

$$\mathcal{E}_{\text{bar}} = \frac{1}{2\mathcal{V}}\sum_{i,j}\Big[\overline{\Delta\mathcal{V}}_{i+\frac{1}{2},j}\overline{u}^2_{i+\frac{1}{2},j} + \overline{\Delta\mathcal{V}}_{i,j+\frac{1}{2}}\overline{v}^2_{i,j+\frac{1}{2}}\Big]\,, \tag{4.16}$$

maximum velocity,

$$V_{\max} = \max\Big\{u_{i+\frac{1}{2},j,k}\,,\ v_{i,j+\frac{1}{2},k}\Big\} \tag{4.17}$$

maximum barotropic velocity,

$$\langle V\rangle_{\max} = \max\Big\{\overline{u}_{i+\frac{1}{2},j}\,,\ \overline{v}_{i,j+\frac{1}{2}}\Big\}\,, \tag{4.18}$$

maximum baroclinic velocity,

$$|V - \langle V\rangle|_{\max} = \max\Big\{u_{i+\frac{1}{2},j,k} - \overline{u}_{i+\frac{1}{2},j}\,, \qquad v_{i,j+\frac{1}{2},k} - \overline{v}_{i,j+\frac{1}{2}}\Big\}\,. \tag{4.19}$$

(In (4.14)–(4.19) above $\Delta\mathcal{V}_{i,j,k}$, $\Delta\mathcal{V}_{i+\frac{1}{2},j,k}$, and $\Delta\mathcal{V}_{i,j+\frac{1}{2},k}$ are control volumes of ρ and velocity component grid boxes,

$$\mathcal{V} = \sum_{i,j,k} \Delta\mathcal{V}_{i,j,k} \tag{4.20}$$

is total volume of the domain,

$$\overline{u}_{i+\frac{1}{2},j} = \frac{1}{\overline{\Delta\mathcal{V}}_{i+\frac{1}{2},j}} \sum_{k=1}^{N} \Delta\mathcal{V}_{i+\frac{1}{2},j,k} u_{i+\frac{1}{2},j,k} \tag{4.21}$$

$$\overline{v}_{i,j+\frac{1}{2}} = \frac{1}{\overline{\Delta\mathcal{V}}_{i,j+\frac{1}{2}}} \sum_{k=1}^{N} \Delta\mathcal{V}_{i,j+\frac{1}{2},k} v_{i,j+\frac{1}{2},k}$$

are barotropic velocity components, and

$$\overline{\Delta\mathcal{V}}_{i+\frac{1}{2},j} = \sum_{k=1}^{N} \Delta\mathcal{V}_{i+\frac{1}{2},j,k} \tag{4.22}$$

$$\overline{\Delta\mathcal{V}}_{i,j+\frac{1}{2}} = \sum_{k=1}^{N} \Delta\mathcal{V}_{i,j+\frac{1}{2},k}$$

are barotropic control volumes.)

From our experiments we find four of these quantities, $\mathcal{E}_{\mathrm{kin}}$, f_{bar}, $V_{\max}$, and $|V - \langle V\rangle|_{\max}$, as the most informative, Fig. 5 . Behavior of the remaining $\mathcal{E}_{\mathrm{bar}}$ and $\langle V\rangle_{\max}$ qualitatively follow $\mathcal{E}_{\mathrm{kin}}$ and $V_{\max}$, hence we chose not to report them. We might also report on the baroclinic part of kinetic energy,

$$\mathcal{E}_{\mathrm{bcn}} = \frac{1}{2\mathcal{V}} \sum_{i,j,k} \left[\Delta\mathcal{V}_{i+\frac{1}{2},j,k}\left(u_{i+\frac{1}{2},j,k} - \overline{u}_{i+\frac{1}{2},j}\right)^2 + \Delta\mathcal{V}_{i,j+\frac{1}{2},k}\left(v_{i,j+\frac{1}{2},k} - \overline{v}_{i,j+\frac{1}{2}}\right)^2\right], \tag{4.23}$$

but it is redundant with (4.14) and (4.16), since $\mathcal{E}_{\mathrm{bcn}} = \mathcal{E}_{\mathrm{kin}} - \mathcal{E}_{\mathrm{bar}}$.

Since ideally the fluid should remain at rest, values above zero should be interpreted as due to numerical errors, Fig. 5 leads to the following observations:

- The overall level of error after long time exceeds by at least one order of magnitude the initial hydrostatic PGF error (measured by holding the ρ field at its initial state and then running the model in a so-called diagnostic regime, resulting in velocity field geostrophically balanced with spurious PGF).
- The long-term error is predominantly barotropic, with 90% of total kinetic energy. Compared to barotropic energy, the energy of the baroclinic component (not shown) and maximum baroclinic velocity error show lesser sensitivity to the choice of z_*. Furthermore, evolution of baroclinic error shows evidence of advective compensation (Mellor *et al*, 1998), so that after initial growth it reaches a maximum and then relaxes to a smaller level. No such compensation occurs for the barotropic error measures.
- The the results show a major sensitivity to the choice of z_*, with total velocity error differences among the cases as much as factor of 4 and error kinetic energy one order of magnitude.
- $\gamma = 0.5$, which corresponds to the "half-and-half" blend of standard and weighted Jacobians, clearly shows the optimum levels of error by all measures.

The first remark partially explains the fact that many attempts to introduce better PGF schemes failed to produce a practically useful result: most of the effort was spent in trying to improve accuracy of hydrostatic balance, while the error level in realistic simulations is controlled primarily by the behavior of the whole model, including not only PGF, but also tracer advection scheme, forms of diffusivity, and viscosity operators.

This might suggest that the solution to the PGF error dilemma lies in the consideration of energetic consistency, which links the design of PGF discretization with the form of advection scheme for tracers (Mesinger & Arakawa, 1976; Janjic, 1977; Arakawa & Suarez, 1983; Michailovich & Janjic, 1986; and Song & Wright, 1998[5]). This consideration appeals to the fact that in a stratified fluid ρ is redistributed predominantly by vertical velocity[6], and since vertical velocity is obtained from divergence of horizontal velocities, which in turn is controlled by the horizontal PGF, failure to obtain cancellation of potential and kinetic energy conversion terms (the "omega-alpha" terms, Janjic, 1977) for the discretized of ρ and momentum equations may cause computational instability. As the result, the discrete computation of P from ρ is linked with vertical interpolation of ρ to compute vertical advective fluxes. This relation exists in any model, including those with a

[5] Song & Wright, 1998, contains proof of energetic, momentum, and bottom torque consistency for the standard Jacobian only. No such proof is available for the weighted Jacobian.

[6] In the case of linearized momentum equations, the only mechanism for changing ρ is due to interaction of background stratification and vertical velocity. This is often the dominant mechanism in the general case too.

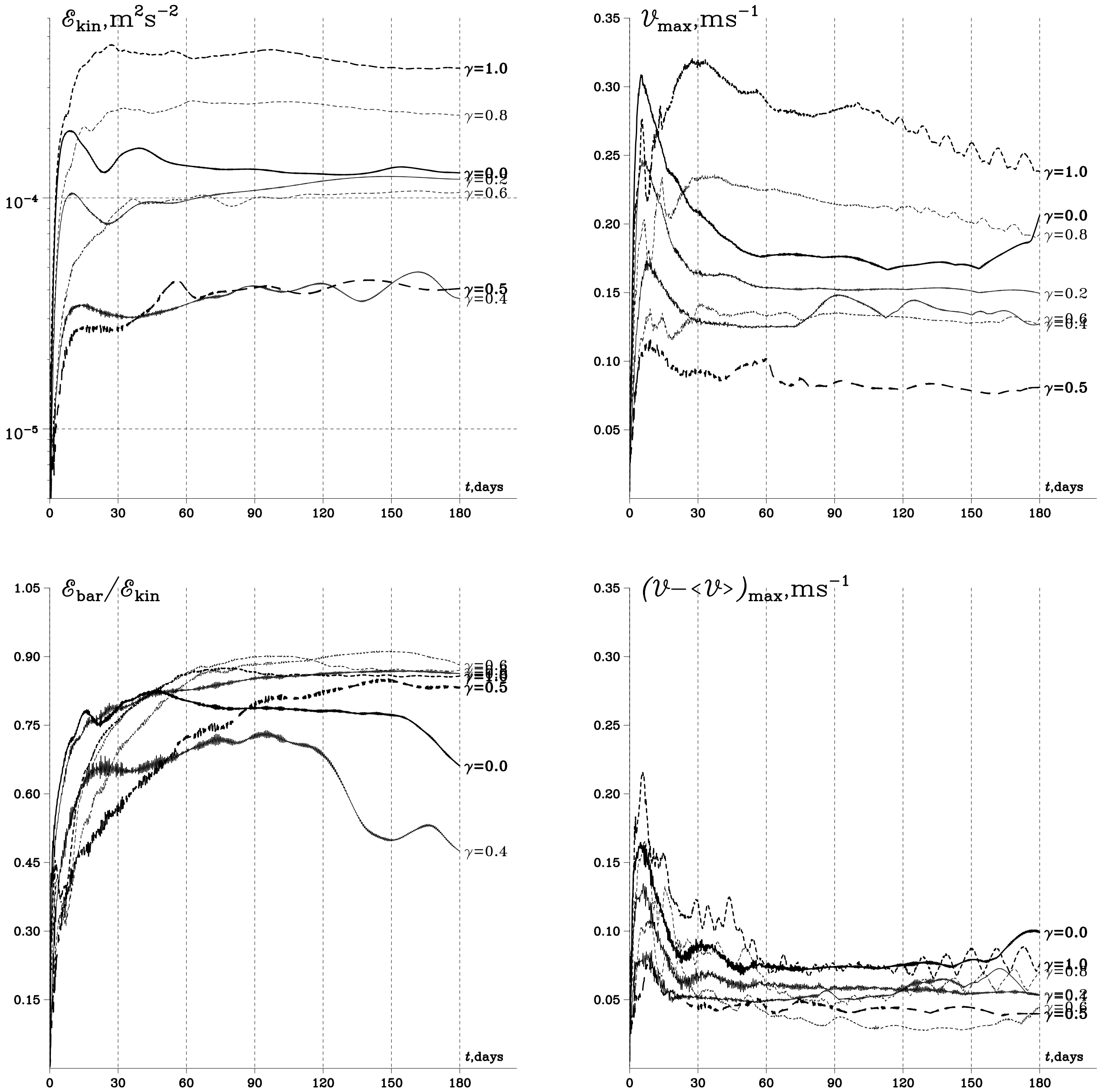

Figure 5. Time histories of net kinetic energy $\mathcal{E}_{\rm kin}$; fraction of barotropic kinetic energy $\mathcal{E}_{\rm bar}/\mathcal{E}_{\rm kin}$; maximum velocity $V_{\rm max}$; and maximum baroclinic velocity $|V - < V >|_{\rm max}$ for a coarse-resolution Seamount test problem on a $(48\times48\times11$ grid) for different values of weighting parameter γ. Solid lines are for $0 \le \gamma \le 0.5$, dashed are for $\gamma > 0.5$. Bold lines are for $\gamma = 0$ (POM Jacobian), $\gamma = 1$ (weighted Jacobian of Song, 1998) and $\gamma = 0.5$ ("optimum" weighting). Note that baroclinic velocity error is relatively insensitive to the choice of γ, and after long-term integration the error becomes predominantly barotropic.

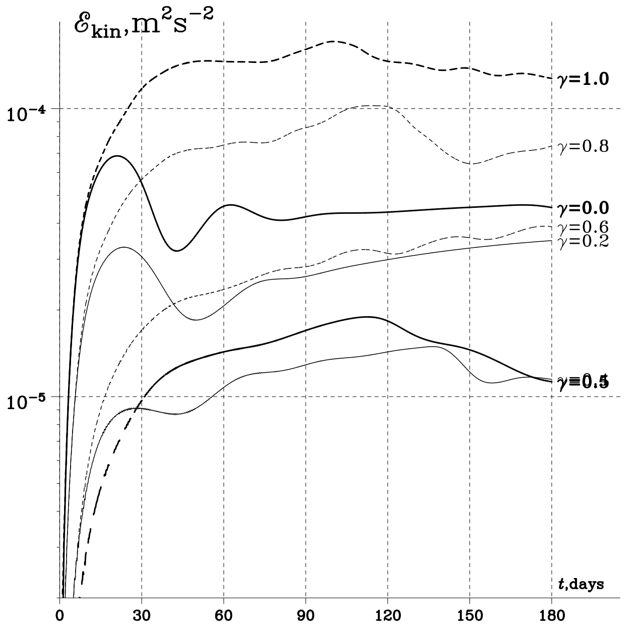

Figure 6. Time history of total energy $\mathcal{E}_{\rm kin}$ for Seamount test problem on $96 \times 96 \times 22$ grid (all conditions are the same as on Fig. 5, except the grid resolution).

z-coordinate. However, in addition to that, due to coordinate slopes in a σ-model, there is a similar link between mid-point interpolations of ρ in along-σ directions in PGF and horizontal advection schemes (cf., (A.13) in Appendix A). However, experience to date shows that in practice an energetically consistent pair of PGF and advection schemes can be easily defeated in terms of error level by an energetically non-consistent pair (e.g., Beckmann & Haidvogel, 1993, as well as experience reported here). Another difficulty here is that analytical proof of energetic consistency is possible only for relatively simple schemes for advection and PGF, and for idealized linear Equation of State of sea water.

The existence of γ corresponding to the minimal error and optimality of the half-and-half blend is very striking, especially after similar behavior was observed in different model configurations (e.g., Fig. 6, where grid resolution is doubled in comparison with Fig. 5, and $\gamma = 0.5$ still maintains its one-order-of-magnitude edge over $\gamma = 0$ or 1). After discovering this phenomenon, practical oceanic modelers did not waste any time in search for its explanation before putting it to use, making it by far the most heavily used PGF scheme in the SCRUM/ROMS[7] community. Yet, it has to be emphasized that this choice has no mathematical foundation and is purely empirical in its nature, for example there is no reason to expect that $\gamma = 0.5$ will be universally optimal for any combination of stratification, bottom topography and grid resolution.

[7] ROMS – Regional Oceanic Modeling System.

5. A Density-Jacobian with Monotonized Cubic Polynomial Fits

Sensitivity to the choice of z_* as well as consideration of alternative forms of density Jacobian lead us to a conclusion that all means to solve the σ-coordinate PGF problem, while staying within the second-order accurate methods, have been exhausted without producing a decisive result. In this section we seek an extension of the Jacobian scheme to higher orders of accuracy. As shown before, the original second-order Jacobian retains a high degree of symmetry and can be equivalently represented in several different forms. Since it is unlikely that a high-order scheme would retain all these symmetries, different versions may be derived depending which second-order prototype is used as the starting point.

We find that a particularly attractive path is to start with the *pseudo-flux* form (2.11) stemming from Green's theorem (2.14). The proposed approach is based on cubic polynomial reconstruction for z and ρ and subsequent analytical integration. Therefore, our goal is to compute

$$-\iint\limits_{\mathcal{A}} \left.\frac{\partial\rho}{\partial x}\right|_z \mathrm{d}x\,\mathrm{d}z\,, \tag{5.1}$$

where $\mathcal{A}$ is the shaded area in Fig. 7. This problem is equivalent to computation of the contour integral,

$$\begin{aligned}-\oint \rho\mathbf{dz} = FX_{i,k+\frac{1}{2}} + FC_{i+\frac{1}{2},k+1} \\ -FX_{i+1,k+\frac{1}{2}} - FC_{i+\frac{1}{2},k}\,,\end{aligned} \tag{5.2}$$

which consists of four segments, two along the side facets,

$$FX_{i,k+\frac{1}{2}} = \int\limits_{s_{i,k}}^{s_{i,k+1}} \rho\frac{\partial z}{\partial s}\,\mathrm{d}s\,, \tag{5.3}$$

and two along the upper and lower facets,

$$FC_{i+\frac{1}{2},k} = \int\limits_{\xi_{i,k}}^{\xi_{i+1,k}} \rho\frac{\partial z}{\partial \xi}\,\mathrm{d}\xi\,. \tag{5.4}$$

In both cases integrals are understood as line integrals and (ξ, s) are the transformed curvilinear coordinates onto which the physical coordinates (x, z) are mapped. In the case where both ρ and z are approximated by segments of linear functions, analytical integration of (5.3)–(5.4) leads to (2.11.

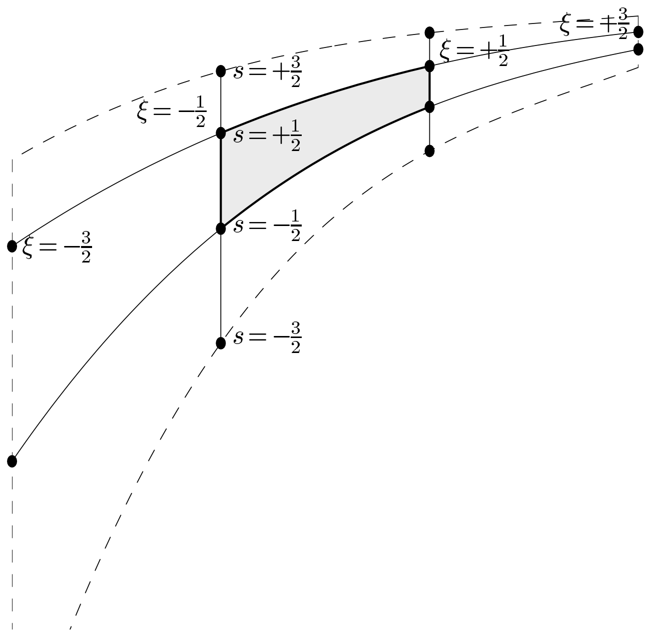

Figure 7. Stencil for pressure-gradient scheme with cubic polynomial fits. Bullets indicate ρ and z points involved in computation of integral of $\left.\frac{\partial\rho}{\partial x}\right|_z$ over shaded area. Because cubic interpolation is used to reconstruct coordinate lines, this appears to be a smooth version of Fig. 1.

The next possibility is to use 4-point cubic Lagrange polynomial fit for ρ, which passes exactly through points $\rho_{i,k-1}$, $\rho_{i,k}$, $\rho_{i,k+1}$, and $\rho_{i,k+2}$ (z is treated similarly), and then integrate analytically between the points $\rho_{i,k}$ and $\rho_{i,k+1}$:

$$f(\xi)=f^{(0)}+f^{(1)}\xi+f^{(2)}\frac{\xi^2}{2}+f^{(3)}\frac{\xi^3}{6}\,, \tag{5.5}$$

where

$$\begin{aligned}
f^{(0)} &= \frac{9}{16}\left(f_{\frac{1}{2}}+f_{-\frac{1}{2}}\right)-\frac{1}{16}\left(f_{\frac{3}{2}}+f_{-\frac{3}{2}}\right)\\
f^{(1)} &= \frac{9}{8}\left(f_{\frac{1}{2}}-f_{-\frac{1}{2}}\right)-\frac{1}{24}\left(f_{\frac{3}{2}}-f_{-\frac{3}{2}}\right)\\
f^{(2)} &= \frac{1}{2}\left(f_{\frac{3}{2}}-f_{\frac{1}{2}}-f_{-\frac{1}{2}}+f_{-\frac{3}{2}}\right)\\
f^{(3)} &= f_{\frac{3}{2}}-3f_{\frac{1}{2}}+3f_{-\frac{1}{2}}-f_{-\frac{3}{2}}\,.
\end{aligned} \tag{5.6}$$

Here we introduce a local fractional coordinate $\xi\in\left(-\frac{1}{2};+\frac{1}{2}\right)$ for the distance between the points. The coefficients (5.6) coincide with fourth-order approximations for mid-point value $f^{(0)}$ and first derivative $f^{(1)}$ and second-order approximations for the second $f^{(2)}$ and third derivatives $f^{(3)}$; this is sufficient to approximate the integral,

$$\int\limits_{-\frac{1}{2}}^{+\frac{1}{2}} f(\xi)\,\mathrm{d}\xi = f^{(0)}-\frac{1}{24}f^{(2)}, \tag{5.7}$$

with fourth order of accuracy. An obvious drawback of this approach is that it is not guaranteed that the right-side limit of the first derivative of the polynomial segment used between points k and $k+1$ matches the left-side limit of segment between $k+1$ and $k+2$ (since these polynomials are obtained from different quartets of points). We therefore abandon the requirement that the cubic polynomial fit pass exactly through extreme points of its stencil, and instead demand that derivatives at $\xi=\pm\frac{1}{2}$ are equal to prescribed values $d_{\pm\frac{1}{2}}$ (whose approximation will be separately specified). This leads to an alternative set of coefficients for (5.5),

$$\begin{aligned}
f^{(0)} &= \frac{f_{\frac{1}{2}}+f_{-\frac{1}{2}}}{2}-\frac{d_{\frac{1}{2}}-d_{-\frac{1}{2}}}{8}\\
f^{(1)} &= \frac{3}{2}\left(f_{\frac{1}{2}}-f_{-\frac{1}{2}}\right)-\frac{d_{\frac{1}{2}}+d_{-\frac{1}{2}}}{4}\\
f^{(2)} &= d_{\frac{1}{2}}-d_{-\frac{1}{2}}\\
f^{(3)} &= 6\left(d_{\frac{1}{2}}+d_{-\frac{1}{2}}\right)-12\left(f_{\frac{1}{2}}-f_{-\frac{1}{2}}\right)\,.
\end{aligned} \tag{5.8}$$

It can be verified that (5.5)–(5.8) guarantees that

$$f\left(\pm\frac{1}{2}\right)=f_{k\pm\frac{1}{2}} \qquad \text{and} \qquad \left.\frac{\partial f}{\partial\xi}\right|_{\xi=\pm\frac{1}{2}}=d_{\pm\frac{1}{2}}\,. \tag{5.9}$$

Substitution of polynomial fits (5.5) for both $\rho(\xi)$ and $z(\xi)$ into integrals (5.3)–(5.4) and integration yields

$$\begin{aligned}
\int\limits_{-\frac{1}{2}}^{+\frac{1}{2}}\rho\frac{\partial z}{\partial\xi}\mathrm{d}\xi &= \int\limits_{-\frac{1}{2}}^{+\frac{1}{2}}\left[\rho^{(0)}+\rho^{(1)}\xi+\rho^{(2)}\frac{\xi^2}{2}\right.\\
&\qquad\left.+\rho^{(3)}\frac{\xi^3}{6}\right]\cdot\left[z^{(1)}+z^{(2)}\xi+z^{(3)}\frac{\xi^2}{2}\right]\mathrm{d}\xi\\
&= \rho^{(0)}z^{(1)}+\frac{1}{24}\rho^{(0)}z^{(3)}+\frac{1}{24}\rho^{(2)}z^{(1)}\\
&\quad+\frac{1}{12}\rho^{(1)}z^{(2)}+\frac{1}{320}\rho^{(2)}z^{(3)}+\frac{1}{480}\rho^{(3)}z^{(2)}\,,
\end{aligned} \tag{5.10}$$

which can be used in conjunction with either (5.6) or (5.8).

After substitution of expressions for $\rho^{(0)}...\rho^{(3)}$ and $z^{(1)}...z^{(3)}$ via (5.8), (5.10) becomes

$$\begin{aligned}
\int\limits_{-\frac{1}{2}}^{+\frac{1}{2}}\rho\frac{\partial z}{\partial\xi}\mathrm{d}\xi &= \frac{\rho_{+\frac{1}{2}}+\rho_{-\frac{1}{2}}}{2}\left(z_{+\frac{1}{2}}-z_{-\frac{1}{2}}\right)\\
-\frac{1}{10}\Bigg\{&\left(d_{+\frac{1}{2}}-d_{-\frac{1}{2}}\right)\left[z_{+\frac{1}{2}}-z_{-\frac{1}{2}}-\frac{dz_{+\frac{1}{2}}+dz_{-\frac{1}{2}}}{12}\right]\\
&-\left(dz_{+\frac{1}{2}}-dz_{-\frac{1}{2}}\right)\left[\rho_{+\frac{1}{2}}-\rho_{-\frac{1}{2}}-\frac{d_{+\frac{1}{2}}+d_{-\frac{1}{2}}}{12}\right]\Bigg\}\,,
\end{aligned} \tag{5.11}$$

where

$$d_{\pm\frac{1}{2}} = \left.\frac{\partial\rho}{\partial\xi}\right|_{\xi=\pm\frac{1}{2}} \quad \text{and} \quad dz_{\pm\frac{1}{2}} = \left.\frac{\partial z}{\partial\xi}\right|_{\xi=\pm\frac{1}{2}} . \quad (5.12)$$

The terms in curly brackets in (5.11) can be interpreted as high-order correction to the trapezoidal integration rule used in (2.11). The remarkable antisymmetry of these terms stems from the property

$$\int_{-\frac{1}{2}}^{+\frac{1}{2}} \rho\frac{\partial z}{\partial\xi}\mathrm{d}\xi = \rho_{+\frac{1}{2}}z_{+\frac{1}{2}} - \rho_{-\frac{1}{2}}z_{-\frac{1}{2}} - \int_{-\frac{1}{2}}^{+\frac{1}{2}} z\frac{\partial\rho}{\partial\xi}\mathrm{d}\xi\,, \quad (5.13)$$

leading to exact antisymmetry of the discrete Jacobian,

$$\mathcal{J}(\rho,z) = -\mathcal{J}(z,\rho)\,, \quad (5.14)$$

now extended to potentially higher orders of accuracy.

The formulation of the PGF algorithm (5.2), (5.3), (5.4), and (5.11) is now complete, with the exception that application of (5.11) requires an estimate of derivatives $d_{\pm\frac{1}{2}}$ and $dz_{\pm\frac{1}{2}}$. These can be computed, for example, from the condition of continuity of the second derivatives using cubic spline formalism, which leads to a tri-diagonal problem

$$d_{j-1} + 4d_j + d_{j+1} = 3\left(f_{j+1} - f_{j-1}\right)\,, \quad (5.15)$$

where $j = 1, \ldots, N$ is either horizontal or vertical grid index. This results in a compact fourth-order interpolation, which is generally more accurate than conventional finite-difference methods (McCalpin, 1994, Chu & Fan, 1997) as long as the interpolated fields are sufficiently smooth on the grid, but, as we will soon demonstrate, it is prone to oscillations and is not robust if there are sudden changes in gradient of the field from one grid interval to the next. In the simplest case derivatives $d_{+\frac{1}{2}}$ are estimated as finite differences,

$$d_{+\frac{1}{2}} = \frac{f_{+\frac{3}{2}} - f_{-\frac{1}{2}}}{2} = \frac{\Delta^+ + \Delta^-}{2}\,, \quad (5.16)$$

where

$$\Delta^- = f_{+\frac{1}{2}} - f_{-\frac{1}{2}} \quad \text{and} \quad \Delta^+ = f_{+\frac{3}{2}} - f_{-\frac{1}{2}} \quad (5.17)$$

are the elementary differences on the left and right sides from point $f_{+\frac{1}{2}}$. Substitution of (5.16) into (5.8) leads to the same expressions for $f^{(0)}$ and $f^{(2)}$ as in (5.6), and consequently the same integral approximation (5.7). However, $f^{(1)}$ and $f^{(3)}$ are different; moreover, $f^{(1)}$ in (5.8) using (5.16) approximates the first derivative with only second-order accuracy, while $f^{(3)}$ is off by a factor of 3 in comparison with the corresponding value from (5.6). Although the polynomial fit defined by (5.5)–(5.16) already produces fourth-order accuracy, it has the disadvantage of producing spurious oscillations if the grid values are not smooth.

If alternatively to (5.16) we define

$$d_{+\frac{1}{2}} = 2\Bigg/\left[\frac{1}{\Delta^+} + \frac{1}{\Delta^-}\right] = \frac{2\Delta^+\Delta^-}{\Delta^+ + \Delta^-}\,, \quad (5.18)$$

as long as Δ^+ and Δ^- have the same sign, and

$$d_{+\frac{1}{2}} = 0\,, \quad (5.19)$$

if $\Delta^+\Delta^- \leq 0$, then it is guaranteed that both $d_{+\frac{1}{2}}$ and $d_{-\frac{1}{2}}$ have the same sign as $f_{+\frac{1}{2}} - f_{-\frac{1}{2}}$, and

$$\begin{aligned} \left|d_{+\frac{1}{2}}\right| &< 2\cdot\min\left\{\left|f_{+\frac{1}{2}} - f_{-\frac{1}{2}}\right|\,,\,\left|f_{+\frac{3}{2}} - f_{+\frac{1}{2}}\right|\right\} \\ \left|d_{-\frac{1}{2}}\right| &< 2\cdot\min\left\{\left|f_{+\frac{1}{2}} - f_{-\frac{1}{2}}\right|\,,\,\left|f_{-\frac{1}{2}} - f_{-\frac{3}{2}}\right|\right\} \end{aligned} \quad (5.20)$$

i.e., at least no more than $2\left|f_{+\frac{1}{2}} - f_{-\frac{1}{2}}\right|$ in both cases, which is sufficient to prove that the first derivative of cubic polynomial fit (5.5)–(5.8),

$$\frac{\partial f}{\partial\xi} = f^{(1)} + f^{(2)}\xi + \frac{f^{(3)}\xi^2}{2} \quad (5.21)$$

maintains its sign to be the same as $f_{+\frac{1}{2}} - f_{-\frac{1}{2}}$ throughout the whole interval of ξ within its area of definition,

$$\left(f_{+\frac{1}{2}} - f_{-\frac{1}{2}}\right)\frac{\partial f}{\partial\xi} \geq 0 \qquad \forall\xi: \quad -\frac{1}{2} \leq \xi \leq +\frac{1}{2}\,. \quad (5.22)$$

In its turn, it guarantees that

$$\left.\begin{aligned} & f_{-\frac{1}{2}} \leq f(\xi) \leq f_{+\frac{1}{2}} \\ \text{or} & \\ & f_{-\frac{1}{2}} \geq f(\xi) \geq f_{+\frac{1}{2}} \end{aligned}\right\} \forall\xi: \quad -\frac{1}{2} \leq \xi \leq +\frac{1}{2}\,, \quad (5.23)$$

regardless of the values $f_{-\frac{3}{2}}$ and $f_{+\frac{3}{2}}$ at the extreme points of the stencil.

Another advantage of (5.18) over (5.16) is its ability to "absorb" nonuniformity of the grid without loss of accuracy in a manner described in Treguier, *et al*, 1996. Suppose that discretized field $\{\rho_k\,, k = 1, N\}$ is defined at locations $\{\rho_k\,, k = 1, N\}$, such that $\Delta z_{k+\frac{1}{2}} \equiv z_{k+1} - z_k \neq \Delta z_{k-\frac{1}{2}} \equiv z_k - z_{k-1}$. Then the second-order accurate approximation for $\partial\rho/\partial z$ at location k is

$$\left.\frac{\partial\rho}{\partial z}\right|_{z=z_k} = \frac{\Delta z_{k-\frac{1}{2}}\frac{\rho_{k+1}-\rho_k}{\Delta z_{k+\frac{1}{2}}} + \Delta z_{k+\frac{1}{2}}\frac{\rho_k-\rho_{k-1}}{\Delta z_{k-\frac{1}{2}}}}{\Delta z_{k+\frac{1}{2}} + \Delta z_{k-\frac{1}{2}}}\,, \quad (5.24)$$

which is derived by assuming a parabolic fit for $\rho = \rho(z)$ (such that it produces exact values of ρ_{k-1}, ρ_k and ρ_{k+1}

in their respective locations), analytically differentiating, and substituting $z = z_k$. Since

$$\left.\frac{\partial \rho}{\partial z}\right|_{z=z_k} = \frac{\partial \rho / \partial s|_{s=s_k}}{\partial z / \partial s|_{s=s_k}}\,, \qquad (5.25)$$

(5.16) leads to

$$\left.\frac{\partial \rho}{\partial z}\right|_{z=z_k} = \frac{(\rho_{k+1}-\rho_k)+(\rho_k-\rho_{k-1})}{\Delta z_{k+\frac12}+\Delta z_{k-\frac12}}\,, \qquad (5.26)$$

which is only first-order accurate because it evaluates the derivative at the location $(z_{k+1}+z_{k-1})/2$ rather than the desired z_k. Similarly, (5.25) in conjunction with (5.18) leads to

$$\left.\frac{\partial \rho}{\partial z}\right|_{z=z_k} = \frac{\Delta\rho_{k+\frac12}\Delta\rho_{k-\frac12}\left(\Delta z_{k+\frac12}+\Delta z_{k-\frac12}\right)}{\left(\Delta\rho_{k+\frac12}+\Delta\rho_{k-\frac12}\right)\Delta z_{k+\frac12}\Delta z_{k-\frac12}}\,, \qquad (5.27)$$

where $\Delta z_{k+\frac12}$ and $\Delta\rho_{k+\frac12} = \rho_{k+1}-\rho_k$ are elementary differences of z and ρ respectively. For the purpose of analysis of (5.27) we assume that field $\rho = \rho(z)$ is locally represented as the sum of linear background and small perturbation,

$$\rho(z) = \alpha z + \rho'(z)\,, \qquad (5.28)$$

and prove that under such conditions (5.27) agrees with (5.24) within second-order accuracy.

Substitution of (5.28) into (5.24) yields

$$\left.\frac{\partial \rho}{\partial z}\right|_{z=z_k} = \alpha + \frac{\Delta z_{k-\frac12}\partial\rho'_{k+\frac12}+\Delta z_{k+\frac12}\partial\rho'_{k-\frac12}}{\Delta z_{k-\frac12}+\Delta z_{k+\frac12}}\,, \qquad (5.29)$$

where we have introduced

$$\partial\rho'_{k+\frac12} = \frac{\Delta\rho'_{k+\frac12}}{\Delta z_{k+\frac12}} = \frac{\rho'_{k+1}-\rho'_k}{\Delta z_{k+\frac12}}\,. \qquad (5.30)$$

Substitution of (5.28) into (5.27) yields

$$\left.\frac{\partial \rho}{\partial z}\right|_{z=z_k} = \left\{\alpha + \frac{\Delta z_{k+\frac12}\Delta\rho'_{k-\frac12}+\Delta z_{k-\frac12}\Delta\rho'_{k+\frac12}}{\Delta z_{k+\frac12}\Delta z_{k-\frac12}} + \frac{\Delta\rho'_{k+\frac12}\Delta\rho'_{k-\frac12}}{\alpha\Delta z_{k+\frac12}\Delta z_{k-\frac12}}\right\} \Bigg/ \left[1+\frac{\Delta\rho'_{k+\frac12}+\Delta\rho'_{k-\frac12}}{\alpha\left(\Delta z_{k+\frac12}+\Delta z_{k-\frac12}\right)}\right]\,, \qquad (5.31)$$

so far without any approximation. Now we assume that the second term in square brackets is much smaller than the preceding 1 and apply a Taylor expansion,

$$\frac{1}{1+x} = 1 - x + x^2 - \dots\,, \qquad (5.32)$$

retaining only linear terms with respect to $\Delta\rho'$:

$$\begin{aligned}\left.\frac{\partial \rho}{\partial z}\right|_{z=z_k} &= \alpha + \frac{\Delta z_{k+\frac12}\Delta\rho'_{k-\frac12}+\Delta z_{k-\frac12}\Delta\rho'_{k+\frac12}}{\Delta z_{k+\frac12}\Delta z_{k-\frac12}} \\ &\quad - \frac{\Delta\rho'_{k+\frac12}+\Delta\rho'_{k-\frac12}}{\Delta z_{k+\frac12}+\Delta z_{k-\frac12}} + \mathcal{O}\left(\left(\frac{\Delta\rho'}{\alpha\Delta z}\right)^2\right) \qquad (5.33)\\ &= \alpha + \partial\rho'_{k-\frac12}+\partial\rho'_{k+\frac12} \\ &\quad - \frac{\partial\rho'_{k+\frac12}\Delta z_{k+\frac12}+\partial\rho'_{k-\frac12}\Delta z_{k-\frac12}}{\Delta z_{k+\frac12}+\Delta z_{k-\frac12}} + \mathcal{O}\left(\left(\frac{\partial\rho'}{\alpha}\right)^2\right)\,,\end{aligned}$$

which then can be easily transformed into (5.29). In its turn, this verifies that harmonic averaging of elementary differences (5.18) results in second-order accurate evaluation of the first derivative on a nonuniform grid as long as the approximated function is smooth in the sense that change of its first derivative within two consecutive unequal grid intervals is small relative to the derivative itself.

Cubic spline (5.15), algebraic (5.16), and harmonic (5.18) averaging require boundary conditions for the interpolated fields, since their respective formulas cannot be applied near the boundaries directly. These boundary conditions arise from the need to use an extended stencil (in comparison with basic second-order schemes) and are essentially artificial; this is a common problem for high-order discretizations. In principle, these boundary conditions can be avoided by shortening the stencil near the boundary, which is equivalent to lowering the order of accuracy there. Lateral boundaries present somewhat lesser difficulty since one often applies Neumann (no-normal-gradient) conditions to the elementary differences $\rho_{i+1,j,k}-\rho_{i,j,k}$ on the coast line, which are typically implemented via an appropriate masking rules for a coast line of arbitrary shape. These boundary conditions are physically justifiable even in a stratified case, if it is implied that the corresponding differences $z_{i+1,j,k}-z_{i,j,k}$ also vanish, hence differencing of ρ is horizontal, and no-normal-gradient is physically consistent with no-flux lateral boundary conditions for heat and salt. Vertical boundaries are more difficult to treat, especially near the bottom, because grid resolution is often coarse, and physically justifiable conditions are elusive. In this case an extrapolation rule must be used near the boundary.

- Neumann: $\partial f/\partial s = 0$ at locations corresponding to $s_{N+\frac12}$ and $s_{\frac12}$, i.e., on the physical boundaries of the domain, which are at half-intervals outside f_N and f_1, respectively,

$$d_N = \frac{6}{5}\left(f_N - f_{N-1}\right) - \frac{7}{15}d_{N-1} \qquad (5.34)$$

$$d_1 = \frac{6}{5}\left(f_2 - f_1\right) - \frac{7}{15}d_2. \qquad (5.35)$$

- Linear extrapolation: $\partial^2 f/\partial s^2 = 0$ at locations of f_N and f_1),

$$d_N = \frac{3}{2}\left(f_N - f_{N-1}\right) - \frac{1}{2} d_{N-1} \tag{5.36}$$

$$d_1 = \frac{3}{2}\left(f_2 - f_1\right) - \frac{1}{2} d_2\,, \tag{5.37}$$

where we have assumed that all quantities on the r.h.s. are known.

The use of (5.34)–(5.35) is justified only if Neumann boundary conditions are physically justified; otherwise, the use of (5.34)–(5.35) can be interpreted as formal reduction of order of accuracy (to the first order) near the boundary. Similarly, (5.36)–(5.37) is equivalent to assumption of a linear distribution of the interpolated field within the grid box adjacent to the boundary, which is formally second-order accurate. In principle, formally more accurate extrapolation formulas can be derived; however, according to our practical experience, going beyond second-order accuracy near the boundary makes the resultant algorithm extremely non-robust in the case of coarse resolution. Note that harmonic averaging (5.18) guarantees that

$$\left|d_{N-1}\right| < 2\left|f_N - f_{N-1}\right|\,, \tag{5.38}$$

and that d_{N-1} has the same sign as $f_N - f_{N-1}$. Therefore (5.36) guarantees that (i) d_N always maintains the same sign as both $f_N - f_{N-1}$ and d_{N-1}, and (ii) d_N does not exceed $\frac{3}{2}\left(f_N - f_{N-1}\right)$, regardless of non-smoothness of grid data within the three points adjacent to the boundary.

Fig. 8 compares density profiles $\rho(z)$ reconstructed by the three interpolation methods discussed here for the case of step-like profile. As expected, on a hydrostatically inconsistent grid, interpolation along σ-slope results in greater vertical distances between grid points (Fig. 8, second column), making it more difficult for the interpolation scheme. As the result, spline and algebraic averaging tend to oscillate, while harmonic averaging produces a robust (though not very accurate) monotonic profile.

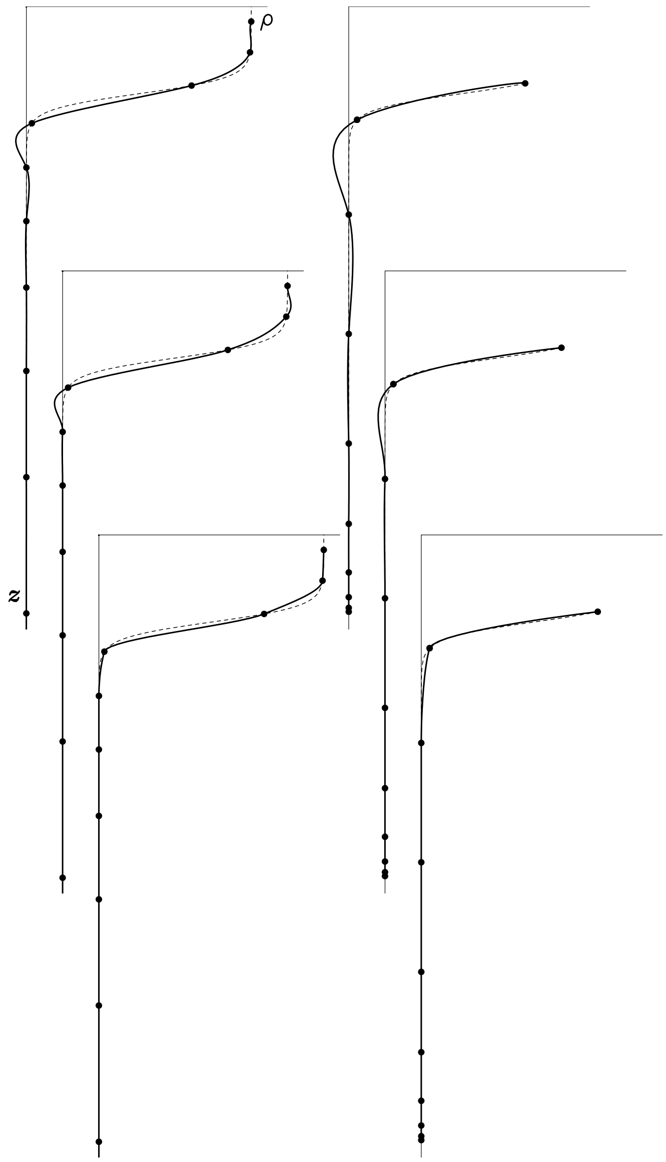

Figure 8. Comparison of three interpolation methods for a step-like profile: **upper row** — both z and ρ are interpolated as functions of s or ξ using cubic spline (5.15); black dots correspond to the actual data points; solid curves represent interpolated profiles, and dashed — the exact profiles. **middle row** — local cubic polynomial based on algebraic averaging of elementary differences (5.16). **bottom row** — using harmonic averaging (5.18). **Left column** — interpolation in vertical direction; **right column** — interpolation along σ-slope across the location of extreme r_x on Fig. 4 resulting in a more concentrated placement of points near the bottom, where σ-surfaces tend to be more horizontal, but effectively coarser resolution near the thermocline; the uppermost data pont on the profile corresponds to the horizontal location above the top of Seamount.

Density-Jacobian Algorithm

We summarize the proposed algorithm[8] as the following sequence:

- Compute and store in provisional arrays elementary vertical differences of $\Delta\rho_{i,k+\frac{1}{2}} = \rho_{i,k+1} - \rho_{i,k}$ and $\Delta z_{i,k+\frac{1}{2}} = z_{i,k+1} - z_{i,k}$ for all $k = 1, \ldots, N-1$.

[8]This algorithm is known as `prsgrd32.F` in the ROMS code.

• Compute $d_{i,k}$ and $dz_{i,k}$, which are harmonic averages of $\Delta\rho_{i,k\pm\frac{1}{2}}$ and $\Delta z_{i,k\pm\frac{1}{2}}$ respectively, using (5.18) for all $k = 2, \dots, N-1$.

• Apply boundary conditions at top and bottom to d and dz using an appropriate extrapolation rule, say (5.36)–(5.37). (Once computation d and dz is complete, provisional variables $\Delta\rho$ and Δz are no longer needed and may be discarded).

• At the upper half of top-most grid box, compute and store in a provisional array,

$$FX_{i,N+\frac{1}{2}} = \left[\rho_{i,N} + \frac{1}{2}(\zeta_i - z_{i,N})\frac{\rho_{i,N}-\rho_{i,N-1}}{z_{i,N}-z_{i,N-1}}\right] \times (\zeta_i - z_{i,N})$$

(derived from the assumption of a linear profile for ρ within the upper half of the top-most grid box), after which compute and store

$$\begin{aligned} FX_{i,k+\frac{1}{2}} = \int_{(\xi,s)_{i,k}}^{(\xi,s)_{i,k+1}} \rho\frac{\partial z}{\partial s}\mathrm{d}s = \frac{\rho_{i,k+1}+\rho_{i,k}}{2}(z_{i,k+1}-z_{i,k}) \\ -\frac{1}{10}\left\{(d_{i,k+1}-d_{i,k})\left[z_{i,k+1}-z_{i,k}-\frac{dz_{i,k+1}+dz_{i,k}}{12}\right]\right. \\ \left. -(dz_{i,k+1}-dz_{i,k})\left[\rho_{i,k+1}-\rho_{i,k}-\frac{d_{i,k+1}+d_{i,k}}{12}\right]\right\} \end{aligned}$$

for $k = 1, \dots, N-1$. (Once all FXs are computed, d and dz may be discarded).

• Compute and store elementary differences along σ-coordinates, $\Delta'\rho_{i+\frac{1}{2},k} = \rho_{i+1,k} - \rho_{i,k}$ and $\Delta' z_{i+\frac{1}{2},k} = z_{i+1,k} - z_{i,k}$. Apply masking rules to them similar to rules for horizontal velocity components;

• Compute $d'_{i,k}$ and $dz'_{i,k}$, which are harmonic averages of $\Delta\rho_{i\pm\frac{1}{2},k}$ and $\Delta z_{i\pm\frac{1}{2},k}$ respectively using (5.18). (Once this step is performed, discard $\Delta'\rho$ and $\Delta' z$.)

• Compute and store

$$\begin{aligned} FC_{i+\frac{1}{2},k} = \int_{(\xi,s)_{i,k}}^{(\xi,s)_{i+1,k}} \rho\frac{\partial z}{\partial \xi}\mathrm{d}\xi = \frac{\rho_{i+1,k}+\rho_{i,k}}{2}(z_{i+1,k}-z_{i,k}) \\ -\frac{1}{10}\left\{\left(d'_{i+1,k}-d'_{i,k}\right)\left[z_{i+1,k}-z_{i,k}-\frac{dz'_{i+1,k}+dz'_{i,k}}{12}\right]\right. \\ \left. -\left(dz'_{i+1,k}-dz'_{i,k}\right)\left[\rho_{i+1,k}-\rho_{i,k}-\frac{d'_{i+1,k}+d'_{i,k}}{12}\right]\right\} \end{aligned}$$

for all $k = 1, \dots, N$.

• Finally, assuming that $FC_{i+\frac{1}{2},N+1} \equiv 0$, compute

$$\begin{aligned} -\mathcal{AJ}_{i+\frac{1}{2},k+\frac{1}{2}} = FX_{i,k+\frac{1}{2}} + FC_{i+\frac{1}{2},k+1} \\ -FX_{i+1,k+\frac{1}{2}} - FC_{i+\frac{1}{2},k}, \end{aligned}$$

and perform its vertical integration

$$-\Delta x\left[\left.\frac{\partial P}{\partial x}\right|_z\right]_{i+\frac{1}{2},k} = -g\sum_{k'}^{N}\mathcal{AJ}_{i+\frac{1}{2},k'+\frac{1}{2}}, \qquad (5.39)$$

for all $k = N, N-1, \dots, 1$ (starting from top and proceeding downward), after which all FXs and FCs may be discarded. (Since sums in (5.39) for different k can be computed recursively, there is no need to store $\mathcal{AJ}_{i+\frac{1}{2},k+\frac{1}{2}}$ in a temporary array.)

Sigma-coordinate Primitive Form

As with the second-order Jacobian, this algorithm can be algebraically transformed into a σ-Coordinate primitive form which resembles (1.1). This implies that the $P_{i,k}$ field is computed first at all $\rho_{i,k}$ points by means of vertical integration[9],

$$P_{i,N} = g\left[\rho_{i,N} + \frac{1}{2}(\zeta_i - z_{i,N})\frac{\rho_{i,N}-\rho_{i,N-1}}{z_{i,N}-z_{i,N-1}}\right] \times (\zeta_i - z_{i,N}),$$

and

$$\begin{aligned} P_{i,k} = P_{i,k+1} + g\frac{\rho_{i,k+1}+\rho_{i,k}}{2}(z_{i,k+1}-z_{i,k}) \\ -\frac{g}{10}\left\{(d_{i,k+1}-d_{i,k})\left[z_{i,k+1}-z_{i,k}-\frac{dz_{i,k+1}+dz_{i,k}}{12}\right]\right. \\ \left. -(dz_{i,k+1}-dz_{i,k})\left[\rho_{i,k+1}-\rho_{i,k}-\frac{d_{i,k+1}+d_{i,k}}{12}\right]\right\} \end{aligned}$$

for all $k = N-1, \dots, 1$ going downward, after which

$$-\Delta x\left[\left.\frac{\partial P}{\partial x}\right|_z\right]_{i+\frac{1}{2},k} = P_{i,k} - P_{i+1,k} - g\cdot FC_{i+\frac{1}{2},k}, \qquad (5.40)$$

where $FC_{i+\frac{1}{2},k}$ is computed the same way as in the previous section.

Note that $FC_{i+\frac{1}{2},k}$ has obvious similarity with the second term in the r.h.s. of (1.6), and within second-order accuracy it is interpreted simply as the product of ρ and local slope of σ-coordinate. The more accurate fourth-order scheme (5.40) computes $FC_{i+\frac{1}{2},k}$ as the integral of the last term in (1.6) along the lower facet of curvilinear trapezoidal element shown as the shaded area in Fig. 7. Although it produces a result algebraically identical to the

[9]This algorithm is known as `prsgrd32A.F` in the ROMS code

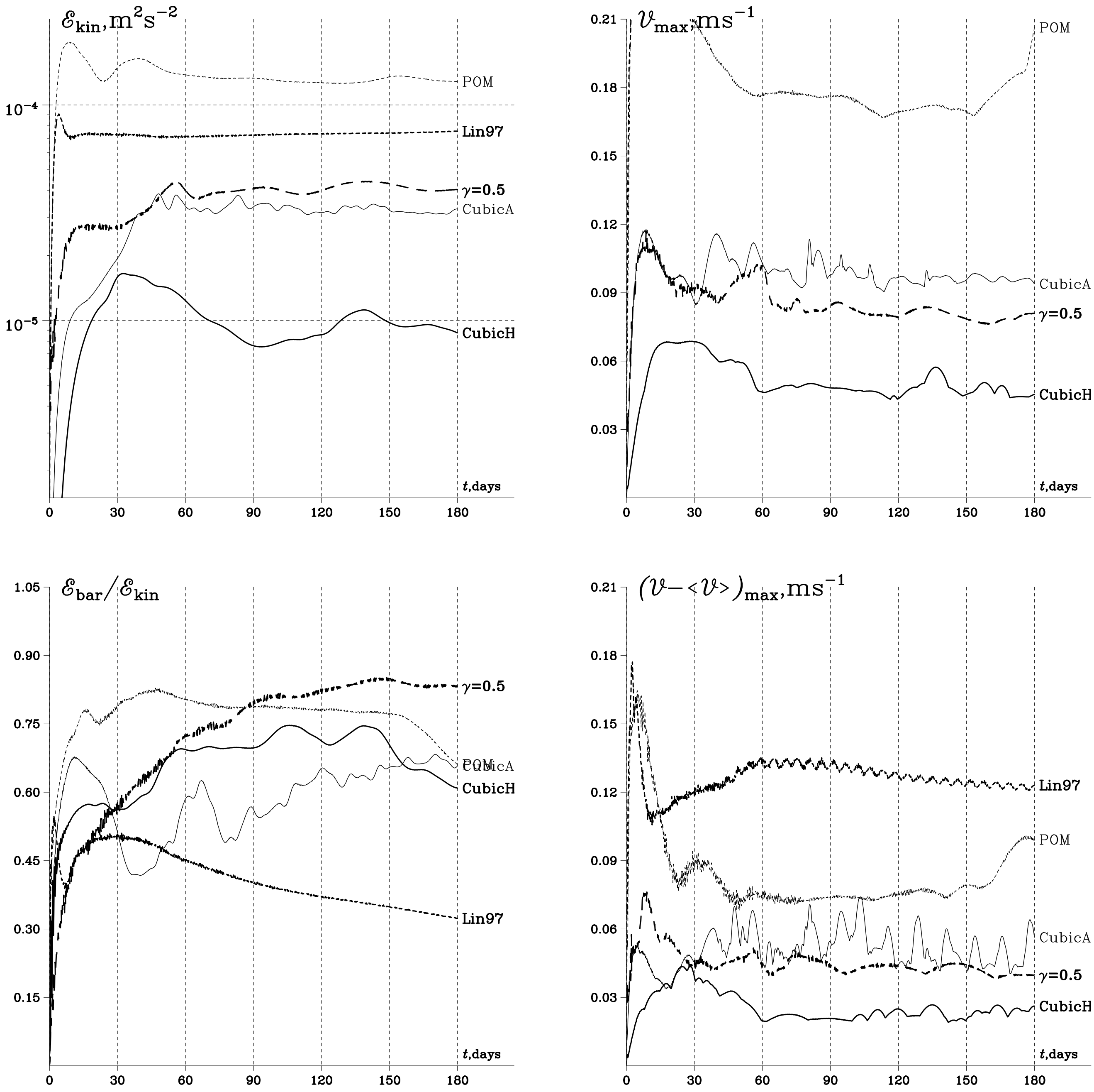

Figure 9. Same as Fig. 5, but for a different set of pressure-gradient schemes. *Cubic H* – method described in the previous section using (5.11) as integration rule with harmonic averaging of elementary slopes by (5.18); *Cubic A* – the same as *Cubic H*, but harmonic averaging is replaced with algebraic mean (5.16); *POM* – POM scheme (same as $\gamma = 0$); $\gamma = 0.5$ – optimum "half-and-half" blend of standard and weighted Jacobians; *Lin97* – Lin's, 1997 finite-volume method (pressure Jacobian scheme). Note that maximum velocity error $V_{\max}$ is outside the plotted range for *Lin97*.

algorithm described in the previous section, the present form offers some technical advantages by eliminating the need to store $FC_{i+\frac{1}{2},k}$ in provisional arrays, since no differencing of FCs is present in (5.40). This results in a more compact code overall.

6. Further Seamount Tests

Fig. 9 shows time histories of all six error measures defined above in a format similar to Fig. 5. Among the previously tested schemes we retain for comparison are the original $\gamma = 0$ (labeled as POM), the optimal density-Jacobian with $\gamma = 0.5$, and the Lin, 1997, finite-volume method. We include two versions of our proposed schemes, one using harmonic averaging of elementary slopes (labeled *Cubic H* on Fig. 9) and one using algebraic averaging (labeled *Cubic A*). At coarse resolution *Cubic H* shows the lowest error by all measures with a substantial edge. At the same time, *Cubic A* and $\gamma = 0.5$ results are comparable, consistent with the previous experience that straightforward attempts to increase the order of accuracy of the scheme do not produce any actual gain in accuracy under realistic simulation conditions like those in the present test problem. Note that the vertical grid spacing on Fig. 4 reaches $1200m$ near the bottom, which exceeds the e-folding scale of $500m$ for the initial $\rho(z)$ in (4.7); similarly, in places with extreme values of $r_x = 2.4$, the vertical distance between consecutive grid points along σ-coordinate lines may reach $800m$. In both cases the consecutive differences of ρ in (5.16) may be different by more than a factor of three, which unavoidably causes oscillation of cubic interpolant and a corresponding increase of error of the PGF scheme. In contrast to *Cubic A*, harmonic slope averaging (5.18) used by *Cubic H* effectively suppresses oscillations, resulting in smallest error on the coarse grid.

In comparison with $\gamma = 0$ and $\gamma = 0.5$, *Cubic H* and *Cubic A* produce somewhat smaller error in the barotropic mode relative to total kinetic energy (cf., panels $\mathcal{E}_{\mathrm{bar}}/\mathcal{E}_{\mathrm{kin}}$ and $\langle V\rangle_{\max}$, especially in the fine resolution case where $\mathcal{E}_{\mathrm{bar}}/\mathcal{E}_{\mathrm{kin}}$ falls below 40%). This is encouraging because erroneous barotropic flow does not have tendency to decrease due to advective compensation mechanism (Mellor *et al*, 1998), which makes it potentially more dangerous type of error in comparison with the baroclinic one.

Our results for improved PGF accuracy invite comparisons with the previously published ones (Beckmann & Haidvogel, 1993,1997; McCalpin, 1994; Chu & Fan, 1997, 1998; Mellor *et al*, 1998; Song, 1998). Doing so, however, is difficult because despite the similarity of the problem set up, crucial differences remain, and we find that the results are highly sensitive to values and forms of viscous operators used, topographic roughness parameters r_D (4.6), differences in vertical grid stretching resulting in different extreme values of r_x (2.10), many of which are not reported in the original papers. Producing such a comprehensive comparison is beyond the scope of this study, and we just restrict ourselves here to demonstrating the sensitivity of the velocity error to the value of the horizontal viscosity; see Fig 10, where in all cases we use the *Cubic H* PGF scheme. As expected, increase of horizontal viscosity results in the decrease of erroneous velocity amplitude; however most of the sensitivity occurs at early times, where the error can be easily reduced by an order of magnitude by choosing viscosity well within the range of that is reported in the literature cited above. Long-term error exhibits a somewhat weaker sensitivity, and increasing viscosity does not decrease the error as much as at early times. We believe that this is partly attributable to the form of discretized viscous operator, which itself can produces spurious currents. (In all computations presented here we used a lateral viscous operator in form of symmetric stress tensor, Shchepetkin & O'Brien, 1996, which is also similar to that of POM, but not of Beckmann & Haidvogel, 1993,1997, and McCalpin, 1994.)

In all cases the levels of energy are at least one order of magnitude higher than that of geostrophically balanced flow caused by the hydrostatic error produced by initial ρ field, which supports a primarily dynamic cause for the errors shown in Figs. 5 and 9.

7. Effect of Seawater Compressibility

Most previously known PGF schemes, including standard and weighted Jacobians, *Lin 97*, etc, are linear algorithms in the sense that an additive change to a given set of density values $\{\rho_k\}$ causes an additive change in the reconstructed profile $\mathcal{P}\left[\rho_k\right]$ and the pressure gradient,

$$\frac{\partial \mathcal{P}}{\partial x}\left[\rho^{(1)}_{i,j,k}+\rho^{(2)}_{i,j,k}\right] = \frac{\partial \mathcal{P}}{\partial x}\left[\rho^{(1)}_{i,j,k}\right] + \frac{\partial \mathcal{P}}{\partial x}\left[\rho^{(2)}_{i,j,k}\right], \quad (7.1)$$

where $\left\{\rho^{(1)}_{i,j,k}\right\}$ and $\left\{\rho^{(2)}_{i,j,k}\right\}$ are two arbitrary sets of grid-box values. This property is a basis for the common practice in σ-modeling of subtracting a predefined background stratification from *in situ* ρ in order to reduce PGF errors. However, the property (7.1) is no longer valid for algorithms which use monotonicity constraints, such as (5.18), and, as we will see, adding or subtracting an arbitrary background ρ profile may significantly degrade the accuracy of computation of PGF. Nonlinear monotonicity constraints usually detect and prevent situations where the derivatives of the reconstructed interpolants

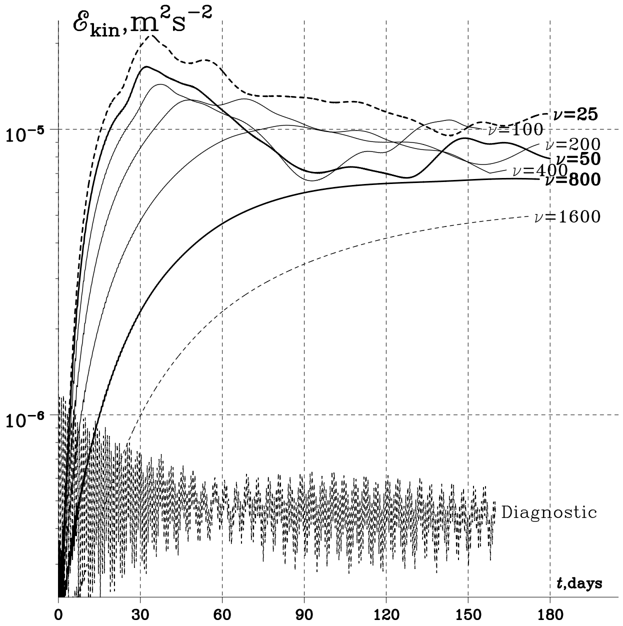

Figure 10. Sensitivity of $\mathcal{E}_{\rm kin}$ to viscosity. Labels $\nu = 25, 50, \ldots, 1600$ at the end of each curve indicate value of viscosity in m^2/s. *Diagnostic* – in this test run density field was kept constant, resulting in flow geostrophically balanced with spurious pressure gradient. This error level provides comparative measure of the error in hydrostatic balance for the initial density field. Grid resolution is $48 \times 48 \times 11$.

have the opposite sign to the difference of the nearest adjacent grid-point values. Taking into account the compressibility of seawater causes difficulty because the only physically meaningful principle of monotonicity here is positive gravitational stability of a stratified fluid, which is not equivalent to maintaining the sign of the derivative of the reconstructed *in situ* ρ profile.

The Equation of State (EOS) for seawater, e.g., Millero *et al*, 1980, is usually written as

$$\rho = \rho(T, S, P)\,, \tag{7.2}$$

where ρ, T, S and P are *in situ* density, temperature, salinity, and pressure respectively. This equation was reformulated by Mellor 1991, Jackett & McDougall, 1995, to allow input of potential temperature, salinity, and depth instead of P,

$$\rho = \rho(\theta, S, z)\,, \tag{7.3}$$

which is more suitable for use in oceanic models because potential temperature (not *in situ* temperature) and salinity are the advectively conserved quantities. Replacement of *in situ* P by depth effectively neglects the effects of baroclinicity due to compressibility in computation of ρ by replacing $g\int \rho {\rm d}z$ with $g\rho_0 z$. The resultant difference is formally within the accuracy of the Boussinesq approximation and is acceptably small for any realistic oceanographic situation. In the case of an incompressible EOS,

$$\rho = \rho(\theta, S)\,, \tag{7.4}$$

the monotonicity constraint of the reconstruction algorithm guarantees that if all differences,

$$\rho_k - \rho_{k+1} \equiv \rho\left(\theta_k, S_k\right) - \rho\left(\theta_{k+1}, S_{k+1}\right) > 0\,, \qquad k = 1, \ldots, N{-}1 \tag{7.5}$$

are positive, then the reconstructed profile is also everywhere positively stratified. This can no longer be guaranteed if EOS includes compressibility. The discretized (7.3) is

$$\rho_k = \rho\left(\theta_k, S_k, z_k\right) \quad k = 1, \ldots, N\,, \tag{7.6}$$

while the compressible analog of the stability condition (7.5) translates into

$$\rho\left(\theta_k, S_k, z_{k+\frac{1}{2}}\right) - \rho\left(\theta_{k+1}, S_{k+1}, z_{k+\frac{1}{2}}\right) > 0\,, \qquad k = 1, \ldots, N{-}1\,, \tag{7.7}$$

where differencing is performed in an adiabatic fashion, since $\rho\left(\theta_k, S_k, z_{k+\frac{1}{2}}\right)$ and $\rho\left(\theta_{k+1}, S_{k+1}, z_{k+\frac{1}{2}}\right)$ are brought to the common level of $z_{k+\frac{1}{2}}$, which in the simplest case is equal to $\frac{1}{2}\left(z_k + z_{k+1}\right)$. Because of this feature (7.7) is not equivalent to just

$$\rho_k - \rho_{k+1} > 0\,, \quad k = 1, \ldots, N{-}1 \tag{7.8}$$

where ρ_k are computed by (7.6). In fact, because of compressibility,

$$\rho_k - \rho_{k+1} \;>\; \rho\left(\theta_k, S_k, z_{k+\frac{1}{2}}\right) - \rho\left(\theta_{k+1}, S_{k+1}, z_{k+\frac{1}{2}}\right)\,,$$

there is the possibility that the r.h.s. can become negative while the l.h.s. remains positive.

To address this problem we decompose the EOS (cf., Jackett & McDougall, 1995),

$$\rho = \frac{\rho_1(\theta, S)}{1 + z/K(\theta, S, z)}\,, \tag{7.9}$$

where $\rho_1(\theta, S)$ is the density at the pressure of 1 atmosphere (i.e., $z = 0$) and $K(\theta, S, z)$ is the bulk secant modulus, which takes compressibility into account. Both $\rho_1(\theta, S)$ and $K(\theta, S, z)$ are approximated by polynomial fits of θ, S, $S^{1/2}$, and z. Furthermore, (7.9) may be rewritten as

$$\rho = \frac{\rho_0 + \rho_1'(\theta, S)}{1 + z\,/\left(K_0 + K'(\theta, S, z)\right)}\,, \tag{7.10}$$

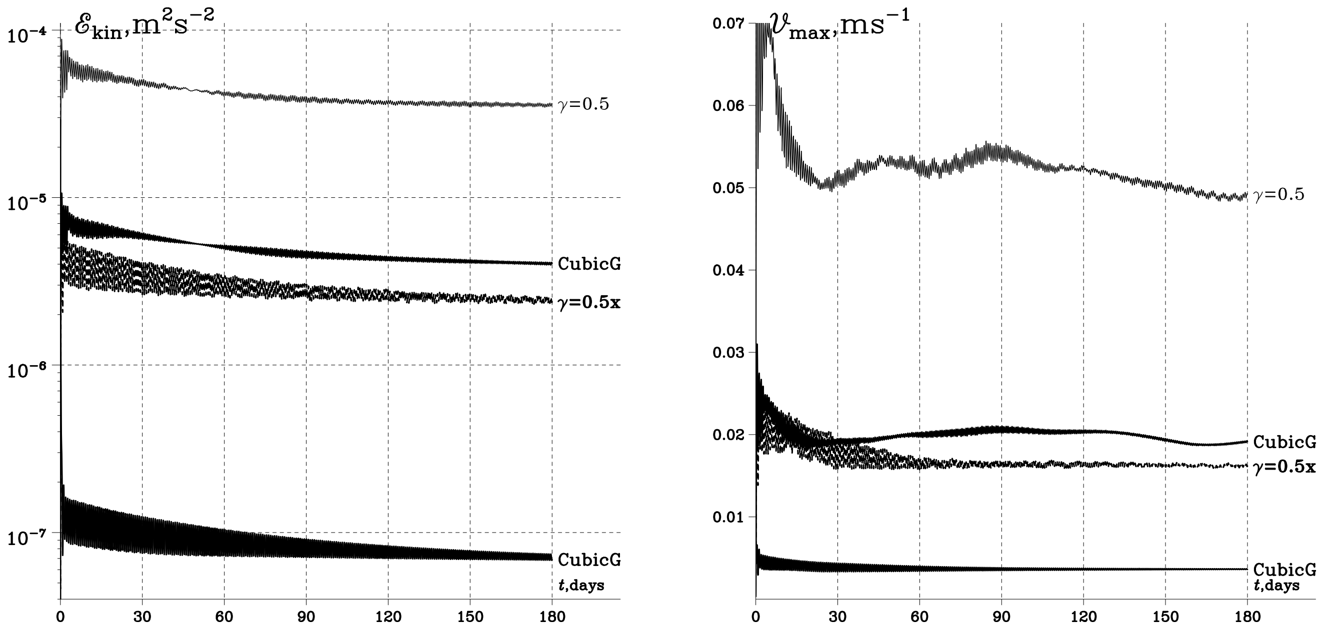

Figure 11. Time history of kinetic energy $\mathcal{E}_{\text{kin}}$ and maximum velocity error V_{max} for Seamount test problem with uniform temperature and salinity ($\theta = 4^0C$ and $S = 33\,^0/_{00}$) using full, nonlinear compressible EOS (7.9) . Two upper curves labeled *Cubic H* and $\gamma = 0.5$ correspond to the resolution of $48 \times 48 \times 11$, grid points, while two lower curves are for the doubled resolution of $96 \times 96 \times 22$.

where ρ_0 and K_0 are the leading-order, constant terms in the original polynomial fits for $\rho_1(\theta, S)$ and $K(\theta, S, z)$. Since $\rho_1'(\theta, S, z) \ll \rho_0 = 999.84\ kg/m^3$ and $K'(\theta, S, z) \ll K_0 = 190925\ m$, as well as $z \ll K_0$ for any reasonable depth within the range of 0-11000 m, one can expand (7.10) in a Taylor series,

$$\rho = \rho_0 \left[1 - \frac{z}{K_0} + \left(\frac{z}{K_0}\right)^2 + ...\right] + \\ +\rho_1' \left[1 - \frac{z}{K_0} + ...\right] + \qquad (7.11) \\ +\frac{\rho_0 K'}{K_0} \left[\frac{z}{K_0} + \frac{(K'+z)^2}{K_0^2} + ...\right] .$$

The first term on the second line is the usual baroclinic ρ perturbation, while the first term on the third line is the leading-order contribution to PGF due to the joint effect of compressibility and baroclinicity (commonly known as thermobaricity). All terms on the first line depend on z only, and, therefore, they should not contribute to PGF; however, as we will demonstrate, they turn out to be a major source of PGF error in σ models. In principle, both second-order Jacobian and our new scheme produce zero error, if density is a linear function of z (such as the leading term on the first line of (7.11)), but the remaining terms are nonlinear and their polynomial fits are not exact, resulting in nonzero PGF error.

To illustrate the severity of the problem we set up a Seamount test problem in which temperature and salinity are set to be uniform, $\theta = 4^0C$ and $S = 33\,^0/_{00}$, and ρ is computed using the full EOS (7.9); thus, ρ is a function of z only and varies only due to compressibility. The results are shown on Fig. 11, in a format similar to Fig. 5. The overall level of errors is comparable with that on Figs. 5–9 for similar algorithms and resolutions, with some qualitative differences in spatial distributions and temporal behavior of this new type of error, resulting in a maximum erroneous velocity of 2 and 5 cm/s for coarse-resolution implementations of the $\gamma = 0.5$ and Cubic H schemes, respectively. This indicates that the inclusion of compressibility in the straightforward way most likely causes more inaccuracy in the velocity field due to σ-coordinate PGF errors than the inaccuracy caused by unphysically neglecting compressibility effects altogether (i.e., using just $\rho_1(\theta, S)$ instead of $\rho(\theta, S, z)$ from (7.9) for the purpose of PGF computation). The problem is further aggravated by the fact that there is no advective compensation mechanism, cf., Mellor *et al*, 1994, for this kind of error, resulting in an erroneous velocity field determined purely from geostrophic balance with hydrostatic PGF error generated by nonlinear terms on the first line of (7.11). If the Coriolis frequency is set to zero (as on the Equator), there is nothing to balance the erroneous PGF and the model becomes unstable. Unlike the case of Fig. 5, now we do not observe any significant sensitivity to the choice of reference level z_* (see (4.1), nor do we see any significant growth of energy of the barotropic mode.

To cure this problem, one must somehow exclude the large terms in (7.11), which are functions of z only, cf., Mellor *et al*, 1994, Dukowicz, 2001. Thus, within the accuracy of the Boussinesq approximation and for the purpose of PGF computation, we therefore can use a simplified equation of state,

$$\rho = \rho_1'(\theta, S) + \frac{\rho_0 K'(\theta, S, z)\cdot z}{K_0^2}\,, \tag{7.12}$$

which still retains a nonlinear dependency of ρ on T and S. Alternatively, one may subtract

$$\rho_{\rm bak}(z) = \frac{\rho_0}{1+z/K_0} \tag{7.13}$$

from (7.10), which, after cancellation of all large terms yields,

$$\rho = \frac{\rho_1'\left(K_0+K'\right)\left(K_0+z\right)+\rho_0 K'\cdot z}{\left(K_0+K'+z\right)\left(K_0+z\right)}\,, \tag{7.14}$$

which can be used as an alternative to (7.10) without any EOS approximation at all. Furthermore, one can absorb further leading terms depending only from z into K_0 in (7.13), $K_0 = K_0^{(0)} + K_0^{(1)}z + K_0^{(2)}z^2$, which produces an even more accurate cancellation of the vertical ρ gradient due solely to compressibility.

A ρ field computed by (7.12) or (7.14) can be considered to be the dynamically relevant density, since it retains only terms which have a nontrivial contribution to the PGF. In both cases an effort has been made to remove the dominant terms which cause the distinction between adiabatic (7.7) and *in situ* (7.8) ρ gradients, and therefore they are more appropriate for use in a monotonicity-preserving reconstruction algorithm. To demonstrate the practical consequences of replacing (7.10) with (7.12) and (7.14), we compute ρ using the realistic data shown on the left in Fig. 12 using incompressible EOS (7.4) and three different versions for treatment of compressibility, (7.9), 7.12), and (7.14). In this example the vertical gradient of *in situ* ρ is at least one order of magnitude greater than the adiabatic gradient below z=500 m depth. Although reasonably close in the upper 500 m, vertical derivatives of the newly introduced quantities may differ significantly from the desired adiabatic derivative in the abyssal part and may even have a different sign, which makes them unsuitable for the use in a monotonicity-preserving reconstruction algorithm[10].

[10] The fact that it is impossible to define a field whose spatial derivatives are equivalent to adiabatic derivatives of *in situ* ρ (i.e., a globally defined potential density) is discussed in Jackett & McDougall, 1995. They show that "potential density" may be defined only locally in the context of adiabatic differentiation.

The fundamental limitation of the techniques described thus far is that they rely upon additive cancellation of errors by subtracting an *a priori* chosen function of z from ρ, which is assumed to be close enough to the actual *in situ* ρ. Hence, errors may be reduced significantly but not eliminated completely, and the whole approach remains too sensitive to the choice of global parameters such as ρ_0, K_0 (which implicitly depend on globally chosen reference values for potential temperature and salinity). We therefore are motivated to develop a new EOS representation which does not rely on such cancellation. To do this, we first note that

$$\left.\frac{\partial\rho\left(\theta,S,z\right)}{\partial x}\right|_z = \left.\frac{\partial\rho}{\partial\theta}\right|_{S,z}\left.\frac{\partial\theta}{\partial x}\right|_z + \left.\frac{\partial\rho}{\partial S}\right|_{\theta,z}\left.\frac{\partial S}{\partial x}\right|_z\,, \tag{7.15}$$

which translates into

$$\mathcal{J}\left(\rho,z\right) = -\alpha\mathcal{J}\left(\theta,z\right)+\beta\mathcal{J}\left(S,z\right)\,, \tag{7.16}$$

where

$$\alpha\left(\theta,S,P\right) = -\left.\frac{\partial\rho}{\partial\theta}\right|_{S,P}\qquad \beta\left(\theta,S,P\right) = +\left.\frac{\partial\rho}{\partial S}\right|_{\theta,P} \tag{7.17}$$

are thermal expansion and saline contraction coefficients defined (by EOS) in the usual thermodynamical sense, and $P = g\rho_0 z$ is hydrostatic pressure. Eq. (7.16) has an advantage over computing *in situ* ρ via EOS and then using it to compute $\mathcal{J}\left(\rho,z\right)$ because the nonlinearity of EOS (associated with nonlinear θ- and S-dependency as well as with compressibility) no longer contributes to errors of hydrostatic balance in the discretized Jacobian. Eq. (7.16) generates no erroneous flow if θ and S are spatially uniform (e.g., as in Fig. 11.

The remaining problem with (7.16) is the fact that it does not prevent spurious oscillations of the interpolated potential density, even if a non-oscillatory algorithm is used to interpolate θ and S[11]. And it almost doubles the computational cost, because two Jacobians are required. To address the first issue and to mitigate the cost, we note that the flux-difference algorithm (2.11) along with a cubic polynomial fit (5.11) and harmonic averaging (5.18) can be expressed entirely in terms of elementary differences of ρ,

$$d_{i,k+\frac{1}{2}} = \rho_{i,k+1} - \rho_{i,k} \tag{7.18}$$

and similar differences of ρ values adjacent in the horizontal (along-σ, with indices $i+1,k$ and i,k) and diagonal

[11] This may occur, for example, if gradients of θ and S tend to cancel each other in the sense of $\alpha\nabla\theta - \beta\nabla S \approx 0$, so that a non-oscillatory interpolation algorithm applied to θ and S separately does not "feel" the non-smoothness of potential density field in a situation where consecutive differences are much larger for θ and S than for potential density.

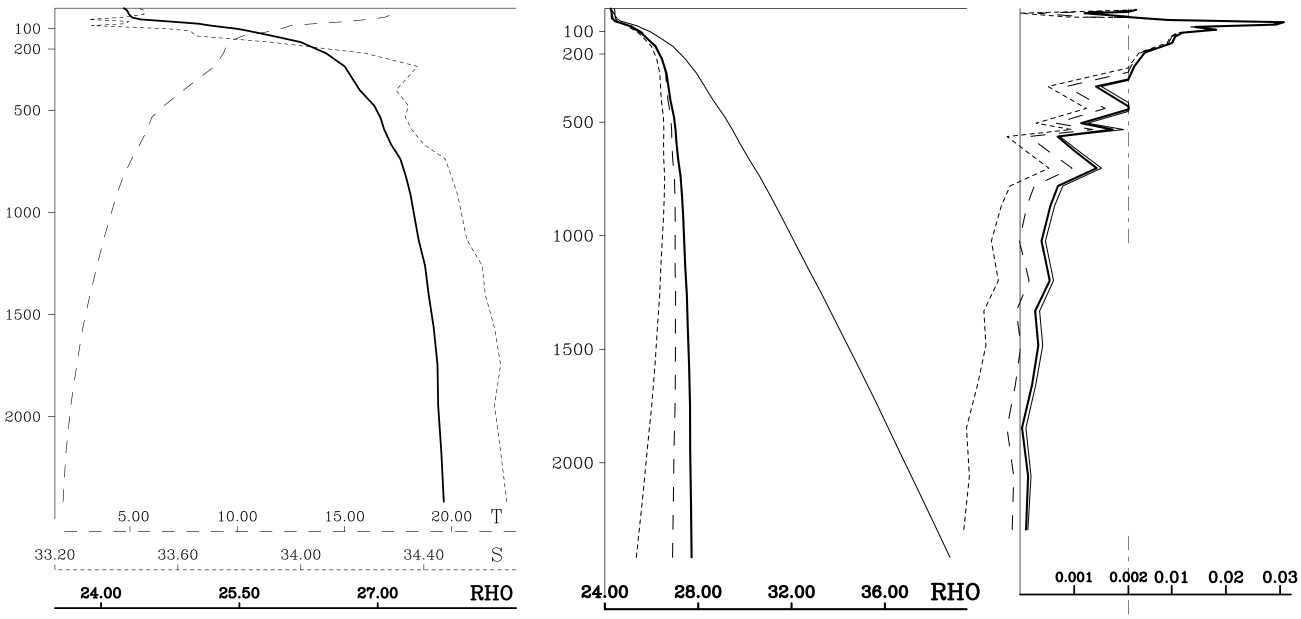

Figure 12. Left – An example of typical measured profiles of *in situ* temperature, salinity, and potential density (with the effect of compressibility removed and $\rho_0 = 1000$ subtracted). These profiles are measured within CalCOFI domain off the California coast. Courtesy of John Moisan. **Middle** – Effect of compressibility in different versions of EOS: *thick solid line* – ρ_1 – density with effects of compressibility removed (this is the same profile on the left); *thin solid line* – ρ – density *in situ* using full nonlinear EOS (7.9); *dotted line* – simplified EOS (7.12)with linearized compressibility effect; *dashed line* – dynamically relevant density $\rho - \rho_{\text{bak}}$ defined by (7.14). **Right** – Vertical derivatives of the corresponding profiles in the middle computed using simple finite differences for all cases, except for *in situ* density ρ (thin solid line), where adiabatic differencing (7.7)is used instead. Note stepped horizontal scale.

($i+1, k+1$ and i, k) directions. This is evident from the fact that all terms in curly brackets in (5.11) already depend only on such differences, and any combination of the preceding terms—the second-order fluxes (2.12)—can be rewritten into the diagonal Jacobian (2.5), which contains only simple diagonal differences but no midpoint averages. Then (7.16) can be discretized by replacing elementary ρ differences with adiabatic differences,

$$\begin{aligned} d^{(\text{ad})}_{i,k+\frac{1}{2}} &= \left[\rho_{i,k+1} - \rho_{i,k}\right]\big|_{\text{ad}} \\ &= -\frac{\alpha_{i,k+1} + \alpha_{i,k}}{2}\left[\theta_{i,k+1} - \theta_{i,k}\right] \\ &\quad + \frac{\beta_{i,k+1} + \beta_{i,k}}{2}\left[S_{i,k+1} - S_{i,k}\right] , \end{aligned} \tag{7.19}$$

which are harmonically averaged in a manner of (5.18), hence enforcing the non-oscillatory property of the cubic interpolant (5.11) and maintaining the sign of the stratification.

The algorithm just described by-passes computation of ρ completely at the expense of the need to compute two fields, α and β as functions of θ, S, and z. Although it does not involve any approximation to EOS, the passive compressibility terms, cf., (7.11), are "differentiated out" at the stage of replacing $\rho_{\text{in situ}}$ with α and β. The computational cost is still very high, in part because of extra work the modified PGF algorithm due to replacement of elementary ρ differences with adiabatic ones via (7.19), and, more significantly, in the EOS part, where the cost is doubled because both α and β are approximately as expensive as $\rho_{\text{in situ}}$. Therefore, we seek practical simplifications that efficiently capture the dynamical effects of compressible EOS. We first note that (7.10) can be approximated by an expansion (cf., Sun, 1999),

$$\rho\left(\theta, S, z\right) = \rho_1'\left(\theta, S\right) + \sum_{n=1}^{n_{\max}} q_n\left(\theta, S\right) \cdot z^n , \tag{7.20}$$

with, in principle, an arbitrary accuracy, depending on the value of $n_{\max}$, and (7.12) can be viewed as the simplest truncation with $n_{\max} = 1$. A detailed assessment of the accuracy of this truncation relevant to the PGF computation—i.e., the ability to produce accurate α and β—is given in Appendix B. We furthermore note that for each n taken separately,

$$\begin{aligned} \mathcal{J}\left(q_n z^n, z\right) &= \frac{\partial}{\partial \xi}\left(q_n z^n\right)\frac{\partial z}{\partial s} - \frac{\partial z}{\partial \xi}\frac{\partial}{\partial s}\left(q_n z^n\right) \\ &= \frac{\partial q_n}{\partial \xi} z^n \frac{\partial z}{\partial s} - z^n \frac{\partial z}{\partial \xi}\frac{\partial q_n}{\partial s} = z^n \cdot \mathcal{J}\left(q_n, z\right) , \end{aligned} \tag{7.21}$$

hence,

$$\mathcal{J}\left(\rho\left(\theta,S,z\right),\,z\right)=\mathcal{J}\left(\rho_1'\left(\theta,S\right),\,z\right)+\sum_{n=1}^{n_{\max}}z^n\cdot\mathcal{J}\left(q_n\left(\theta,S\right),\,z\right),\tag{7.22}$$

which can be used as an alternative to (7.16) or to the straightforward computation of PGF from *in situ* ρ. On the other hand,

$$z^n\cdot\mathcal{J}\left(q_n,z\right)=\mathcal{J}\left(q_n,\frac{z^{n+1}}{n+1}\right),\tag{7.23}$$

so instead of first computing *in situ* ρ [or any substitute quantity for it in the framework of (7.12)–(7.14)] and then using it for computation of horizontal ρ gradient, we can directly compute the contribution from each individual q_n term in $\mathcal{J}\left(\rho(\theta,S,z),\,z\right)$.

A remarkable consequence of (7.23) in the case $n=1$ is that a linear combination of discrete Jacobians,

$$\mathcal{J}\left(q_1 z,z\right)=\frac{1}{3}\Big\{\mathcal{J}\left(q_1 z,z\right)+\mathcal{J}\left(q_1,z^2\right)\Big\},\tag{7.24}$$

vanishes identically if q_1 itself is a linear function of z, even if both Jacobians in the r.h.s. fail to vanish if taken separately. This leads to a replacement of pseudo-fluxes (2.12) with[12]

$$F'''=\left\{\frac{\rho_1''+\rho_1'}{2}+q_1''\frac{2z''+z'}{6}+q_1'\frac{z''+2z'}{6}\right\}\left(z''-z'\right),$$

where prime and double prime stand for the corresponding pairs of indices 21, 42, 43, and 31 in (2.12). The resulting scheme produces no PGF error, not only if ρ is a linear function of z (as in the case of second-order Jacobian), but also if q_1 is linear in z, hence *in situ* density $\rho_1+q_1 z$ is quadratic in z, even though we use the same 2×2-point stencil of the second-order scheme. This property is especially valuable since most of the PGF errors associated with compressibility occur in the abyss, where one cannot rely solely on the order of accuracy of the PGF scheme because the vertical resolution is typically quite coarse there.

We now describe modifications to the Cubic H algorithm in the case of compressible EOS (7.20) that prevent spurious negative stratification due to oscillation of cubic polynomial fits for ρ. For the sake of simplicity and computational efficiency we restrict ourselves to the choice of $n_{\max}=1$.[13] To illustrate the practical accuracy of of this choice, we note that the adiabatic derivative of (7.20) (cf., (7.7)) with respect to transformed coordinate s (similarly ξ) is

$$\left.\frac{\partial\rho\left(\theta,S,z\right)}{\partial s}\right|_{ad}=\frac{\partial\rho_1'\left(\theta,S\right)}{\partial s}+\sum_{n=1}^{n_{\max}}z^n\frac{\partial q_n\left(\theta,S\right)}{\partial s},\tag{7.25}$$

where the contribution of all terms under summation is expected to be much smaller than the leading term on the r.h.s.. This is manifested by the fact that these terms are responsible for the difference between the thick and thin solid lines in the right panel of Fig. 12, and these two lines are very close to each other. This leads to the approximation of adiabatic differences (7.19) with

$$d^{(\mathrm{ad})}_{i,k+\frac{1}{2}}=\rho'_{1\,i,k+1}-\rho'_{1\,i,k}+\frac{z_{i,k+1}+z_{i,k}}{2}\left(q_{1\,i,k+1}-q_{1\,i,k}\right)$$

which in turn can be used to estimate *in situ* ρ derivatives at the non-staggered locations,

$$\left.\frac{\partial\rho}{\partial s}\right|_{i,k}=\frac{2d^{(\mathrm{ad})}_{i,k+\frac{1}{2}}\cdot d^{(\mathrm{ad})}_{i,k-\frac{1}{2}}}{d^{(\mathrm{ad})}_{i,k+\frac{1}{2}}+d^{(\mathrm{ad})}_{i,k-\frac{1}{2}}}+q_{1\,i,k}\left.\frac{\partial z}{\partial s}\right|_{i,k},\tag{7.26}$$

which are needed by (5.11) in order to compute pseudo-fluxes using cubic polynomial fits. The first r.h.s. term is harmonically averaged adiabatic differences of ρ. As in the case of (5.18)–(5.19), this term is reset to zero if $d^{(\mathrm{ad})}_{i,k+\frac{1}{2}}$ and $d^{(\mathrm{ad})}_{i,k-\frac{1}{2}}$ have opposite signs. Since the same harmonic averaging algorithm is used for both vertical and horizontal (along σ) directions, different signs may occur even if the stratification is positive everywhere. (The expressions for adiabatic differences in the horizontal direction are exactly the same as the vertical ones, except that the index i gets increments ±1, while the index k is kept constant.) The second term in the r.h.s. of (7.26) is proportional to the gradient of ρ caused by compressibility and P changes in a neutrally stratified fluid. This adiabatic gradient separates positive and negative stratification, so that replacing the harmonic averaging (5.18) with (7.26)

[12] An identical result may be obtained by analytical integration of quadratic fit $\left[q'\left(z''-z\right)+q''\left(z-z'\right)\right]z/\left(z''-z'\right)$ over the interval from z' to z''.

[13] The method described here can easily be generalized to the case of $n_{\max}>1$ in EOS (7.20) by computing elementary adiabatic differences and the compressible term in (7.26) via

$$d^{(\mathrm{ad})}_{i,k+\frac{1}{2}}=\rho'_{1\,i,k+1}-\rho'_{1\,i,k}+\sum_{n=1}^{n_{\max}}\left(q_{n\,i,k+1}-q_{n\,i,k}\right)\times\frac{{z_{i,k+1}}^n+{z_{i,k}}^n}{2}$$

and

$$d^{(0)}_{i,j}=\sum_{n=1}^{n_{\max}}q_{n\,i,k}\cdot n z^{n-1}_{i,k}\left.\frac{\partial z}{\partial s}\right|_{i,k}.$$

changes the monotonicity constraint (5.20) into

$$
\begin{array}{ll}
& d_{i,k}^{(0)} \le d_{i,k} \le d_{i,k}^{(0)} + 2\delta \\
\text{or} & \\
& d_{i,k}^{(0)} \le d_{i,k} \le d_{i,k}^{(0)} - 2\delta \\
\text{or} & \\
& d_{i,k}^{(0)} \ge d_{i,k} \ge d_{i,k}^{(0)} + 2\delta \\
\text{or} & \\
& d_{i,k}^{(0)} \ge d_{i,k} \ge d_{i,k}^{(0)} - 2\delta
\end{array}
\qquad (7.27)
$$

where $d_{i,k}$ is the *in situ* ρ derivative, $d_{i,k}^{(0)} \equiv q_{1\,i,k}\partial z/\partial s$,

$$\delta = \text{minmod}\left(d_{i,k-\frac{1}{2}} - d_{i,k}^{(0)}\,,\, d_{i,k+\frac{1}{2}} - d_{i,k}^{(0)}\right)$$

and the function *minmod* is equal to the smallest of its arguments by absolute value, if all of them have the same sign, or zero, if the signs are different.

The new compressible EOS PGF scheme differs from the original Cubic H scheme only in the procedure of computing ρ derivatives via harmonic averaging of adiabatic differences (7.26), while all subsequent steps in the algorithm remain the same. This method has the following properties:

- PGF error due to compressibility of seawater with uniform θ and S has been eliminated completely, regardless of particular choice of reference values ρ_0, K_0, etc. Hence, it is not necessary to repeat the experiment of Fig. 11 using the new approach;
- Unlike $\rho\,(\theta, S, z)$, both $\rho_1'(\theta, S)$ and $q_1(\theta, S)$, do not explicitly depend on z which allows us to split the derivative of *in situ* ρ into adiabatic and compressible parts. Hence, a straightforward application of harmonic averaging (5.18) to the adiabatic term guarantees positive stratification along the interpolated profile as long as the discrete values are positively stratified.
- The computational cost of this new PGF scheme and the associated EOS does not exceed significantly the cost of the original Cubic H scheme and EOS.

8. Realistic Tests for the Atlantic Ocean

In order to illustrate the practical effects of the new PGF scheme and alternative treatment of compressibility, we include results from several realistic Atlantic Ocean simulations. The model bathymetry shown on Fig. 13 is the same as in Haidvogel *et al*, 2000, with 3/4 degree spatial resolution and S-coordinate stretching parameters

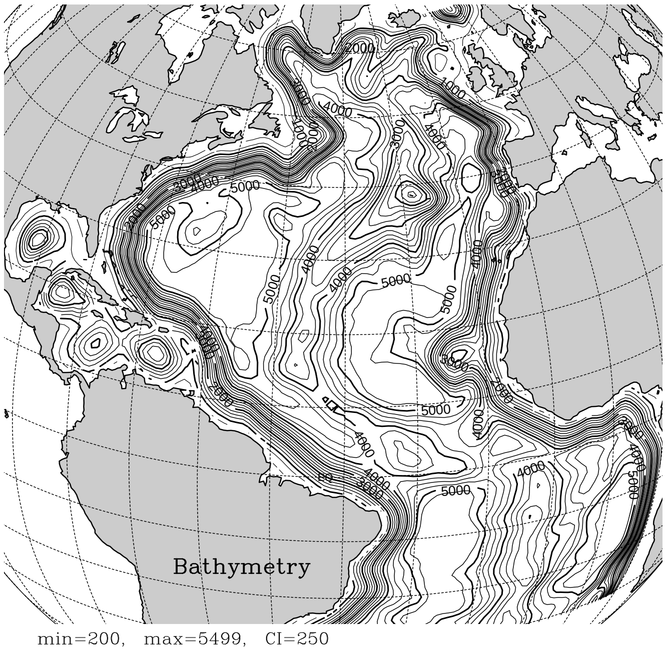

Figure 13. Model Bathymetry for a 3/4 degree-resolution Atlantic Ocean simulation

$\vartheta = 5$, $\vartheta_b = 0.4$, and $h_{\min} = 200$m, which translate into a maximum topographic "r-factor" of 0.195 and a maximum σ-grid stiffness ratio of $r_x = 3.82$. Hence, despite its relatively smooth appearance, this model topography causes a strong violation of the hydrostatic consistency criterion and a relatively large change of bottom depth per horizontal grid interval compared to common σ-modeling practices. The test results reported here may be also considered as verification of robustness of the newly designed algorithm with respect to coarse vertical resolution and a non-smooth ρ field, which has been recognized as a major concern for PGF schemes with higher than second-order accuracy, Kliem & Pietrzak, 1999.

For the flat-stratification test problem, the wind stress and surface heat and fresh-water fluxes are set to zero, and we choose a horizontally uniform potential temperature profile (in ${}^0C$),

$$\theta = 0.2 + 6\exp\{-|z|/2500\} + 20\exp\{-|z|/250\} \quad (8.1)$$

and a uniform salinity $S = 35^0/_{00}$. The amplitude and e-folding scales for this profile are representative of an instantaneous profile in a selected location in the tropical Atlantic (where, as we will see, the largest PGF errors occur), rather than basin-scale averaged profile. We believe that this is more appropriate, since PGF errors are controlled by local profiles, while a horizontally averaged profile tends to be much smoother. (For a similar test, Mellor *et al*, 1994, chose an e-folding scale of 1000 m, which is also comparable with horizontally averaged profiles re-

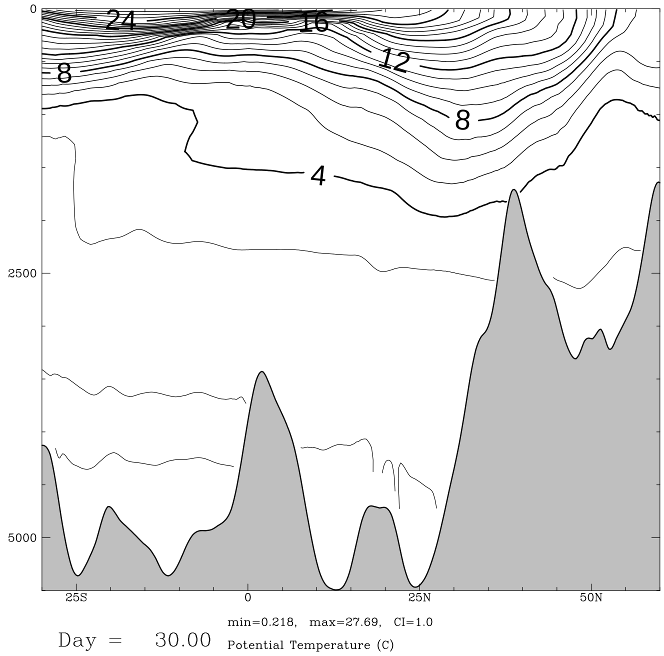

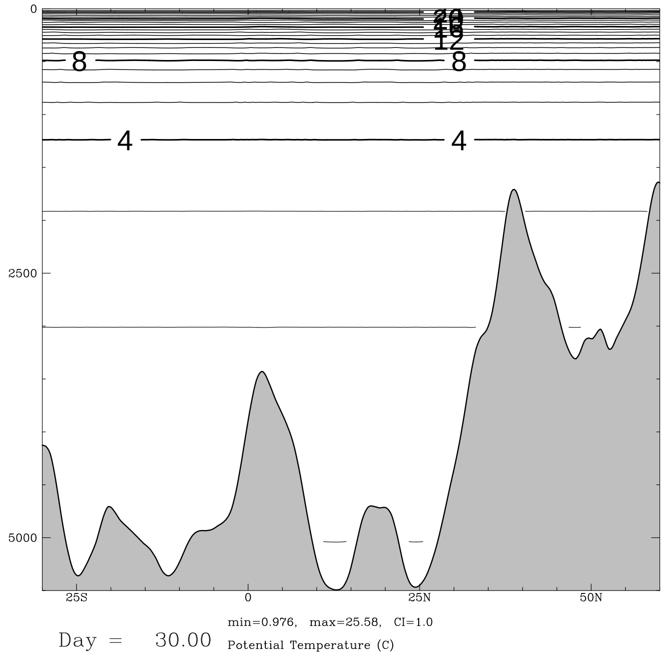

Figure 14. Potential temperature cross-section at 30^0W: **left** – from Levitus data; **right** – profile (8.1) for flat stratification tests. In both cases the contour interval is 1^0C.

ported in Haidvogel *et al*, 2000.) A comparison of our idealized profile with measurements is shown on Fig. 14. Note that our profile has comparable abyssal stratification, thermocline depth, and steepness of transition from the abyss to the thermocline. The advection scheme for material tracers is 4th-order, centered, and with harmonic averaging of elementary differences—similar to that for the Seamount problem. There is no material diffusion of any kind, neither vertical, horizontal, nor implicit via upstream-biased advection. A 4th-order centered scheme is used for momentum advection. The horizontal viscosity is 500 m^2/s.

The flow pattern after a 60-day spin up using POM Jacobian ($\gamma = 0$) and realistic EOS with compressibility turned OFF is shown in the top-left panel of Fig. 15. We find that the maximum errors for this test problem (as well the other tests reported later) occur between depths of 1000 to 1500 meters, so we choose 1500 meters as the representative level to display. The error pattern on the top-left panel is typical for σ-models. It is characterized by spurious flow along topographic slopes especially near the Equator. The error is around 3 cm/s near the Gulf-Stream area and off the North-American coast. We see a visualized mid-Atlantic ridge, closed circulation in the Caribbean abyss, and strong jets along the Equator. The largest errors occur off the Brazilian coast near Equator, 15 cm/s, which is not surprising, since stronger currents are required to achieve geostrophic balance with a given spurious PGF at lower latitudes. The weighted $\gamma = 0.5$ scheme produces comparable, but approximately 40% larger, currents and an overall similar error pattern in this test (Fig. 15, top right). Remarkably, the direction of spurious currents is reversed in comparison with the $\gamma = 0$ results. Varying the weighting factor reveals an optimal choice of $\gamma = 0.21$ for minimum mean error. This is similar to the Seamount problem experiments, except that here the optimal value is different, indicating that there is no universally optimal choice. Finally, the Cubic H scheme (Fig. 15, lower left) results in a dramatic decrease of errors and an overall change in the error pattern. It is no longer possible to see coherent currents along topographic slopes and mid-Atlantic ridge. The largest errors still occur near Equator, but now the flow pattern there has a more random character.

Turning compressibility back ON causes a dramatic increase of errors almost everywhere, which is manifested by appearance of currents along topographic slopes (Fig. 16 , top left). Although still, with somewhat smaller amplitude, the compressible Cubic H errors are more comparable with that for the second-order $\gamma = 0$ and $\gamma = 0.5$ schemes, rather than for the Cubic H case shown in the previous incompressible Fig. 15. Again, the most significant errors occur near the Equator. There is no advective compensation mechanism for PGF errors generated by a vertical ρ profile due to compressibility of seawater with uniform θ, S. Consequently, this kind of error may

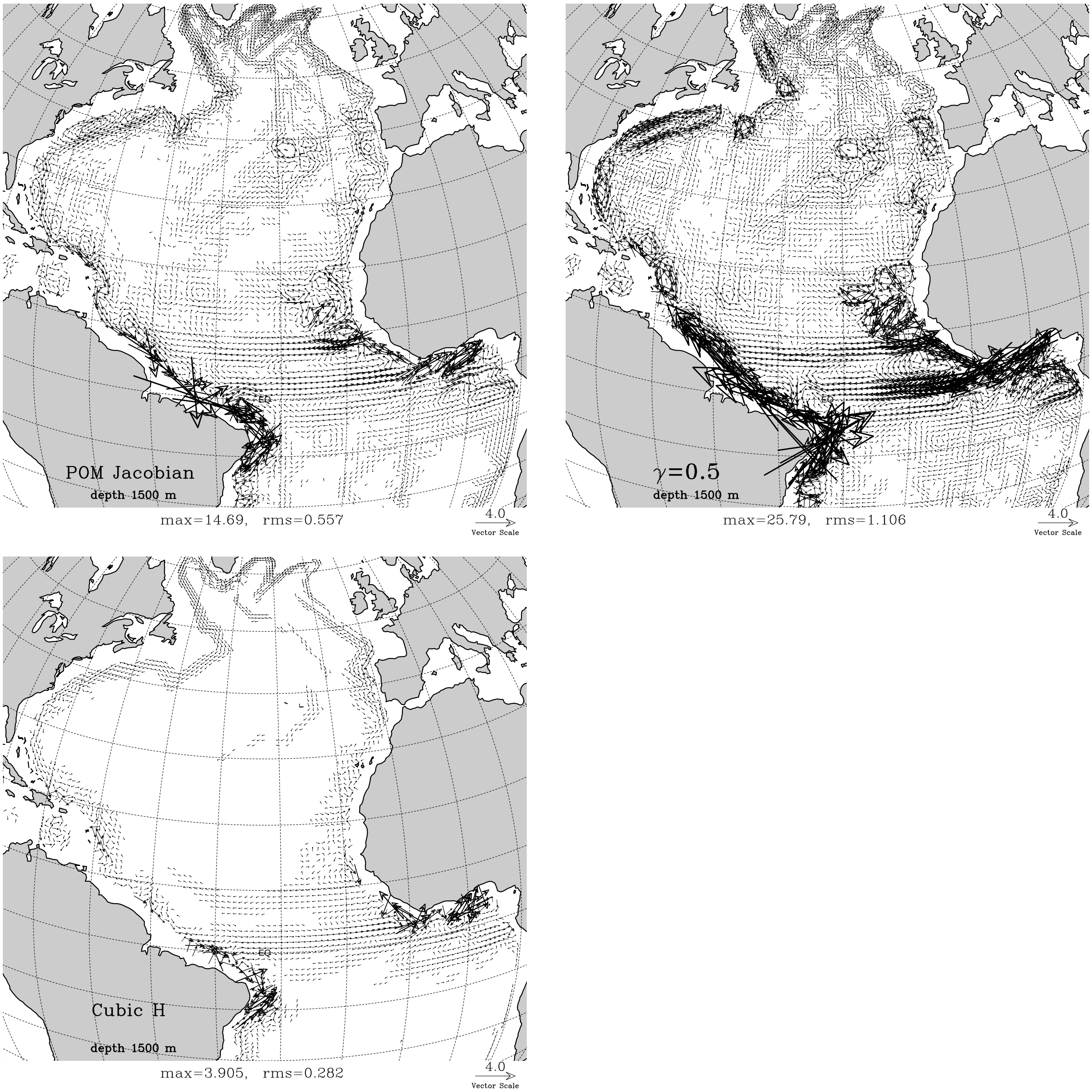

Figure 15. Spurious currents from a flat-stratification, pressure-gradient error test problem for a realistic bathymetry Atlantic Ocean model configuration after 60 days of simulations, starting from rest initial condition. In all three cases shown here, EOS compressibility effects were turned OFF completely by setting $\rho_{\mathrm{in\,situ}}(\theta, S, z) = \rho_1(\theta, S)$; Velocity scale is in cm/sec; vectors with magnitude smaller that 0.05 cm/s are not shown. **Top-left** – POM Jacobian ($\gamma = 0$); **Top-right** – $\gamma = 0.5$-scheme; Note that for $\gamma = 0$ and 0.5 flow directions are opposite near Brazilian coast, where the largest errors occur. **Lower-left** – *Cubic H* pressure-gradient algorithm.

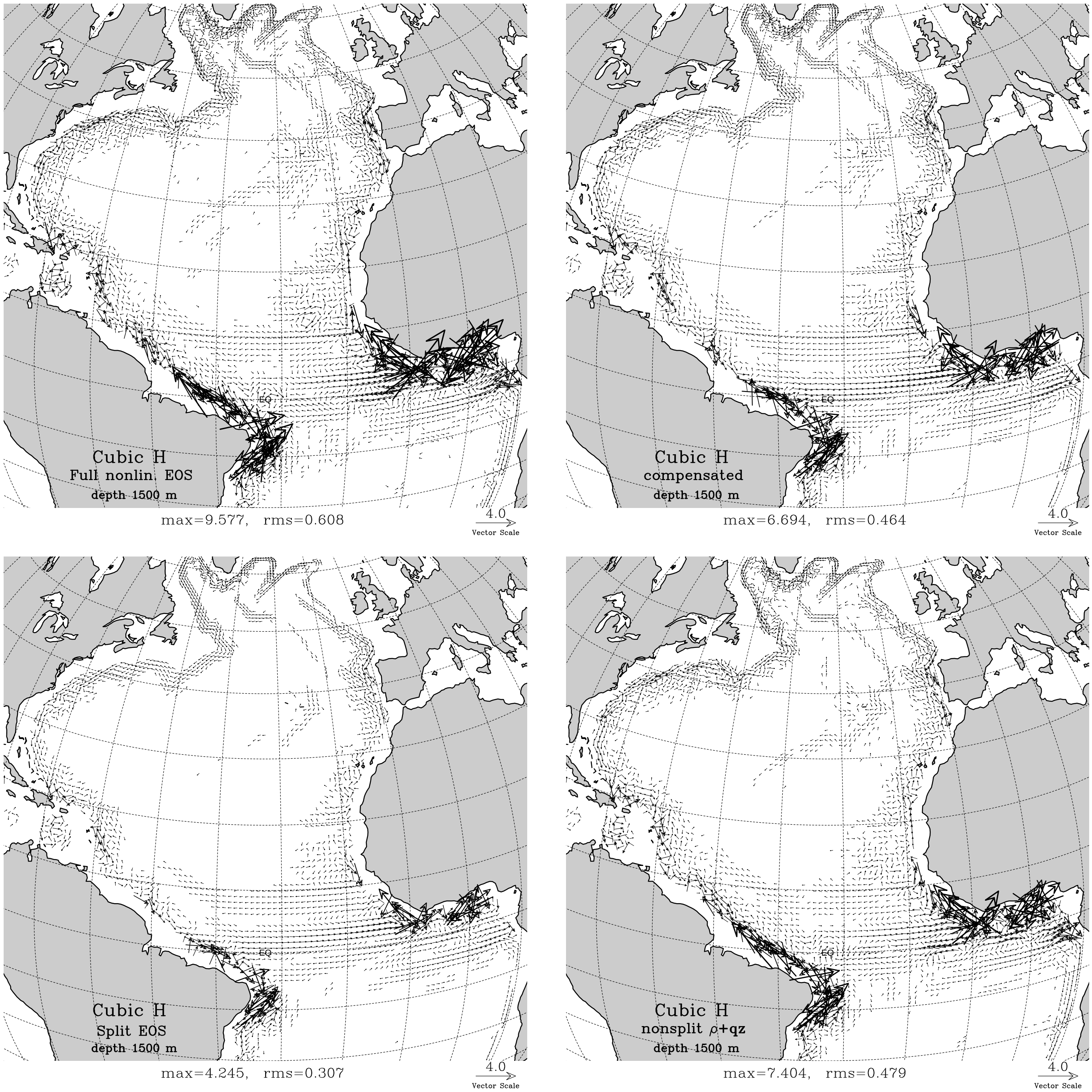

Figure 16. The same as on Fig. 15, except that now *Cubic H* – family algorithms are used in combination with different treatment of compressibility: **lop-left** – EOS (7.9) retaining all nonlinear compressibility terms; **top-right** – same as on the left, but most of the passive vertical density gradient is removed by subtracting $\rho_0/\left(1-0.1|z|/K_{00}\right)$ resulting in (7.14); **lower-left** – modified *Cubic H* algorithm in combination with EOS split into incompressible and compressible parts $\rho = \rho_1\left(\theta,S,z\right) + q_1\left(\theta,S,z\right)|z|$, thus allowing computation of derivative of density via harmonic averaging of adiabatic differences (7.26); **lower-right** – control experiment where EOS is the same as on the left, but ρ_1 and q_1 terms are combined at the stage of computation of *in-situ* density, which is then used in the original non-split version of *Cubic H*. This is equivalent to just linearization of compressibility effects.

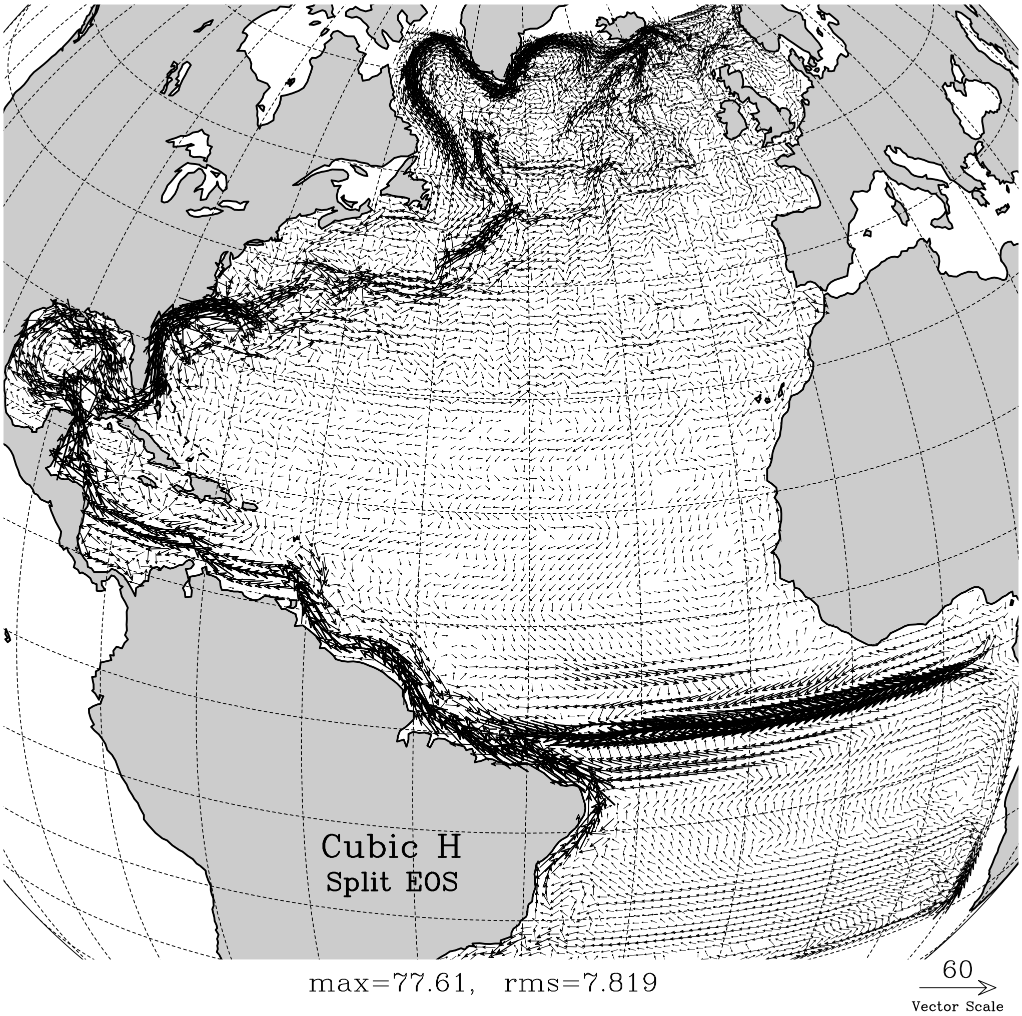

Figure 17. Near-surface currents time-averaged over 6-month period after 3-year spin up of North-Atlantic model simulation starting from Levitus climatological initial conditions and running under realistic wind and thermodynamic forcing, using modified *Cubic H* + (7.26) pressure-gradient algorithm and split EOS (7.20) with $n_{\max} = 1$ (same combination as on lower-left panel of Fig. 16).

be balanced only by Coriolis or viscous forces. Subtraction of the dominant part of the mean passive compressibility term, $\rho_0/\left(1-|z|/K_{00}\right)$, reduces the error to some extent, but it fails to produce any significant benefit in the Equatorial region (Fig. 16, top right). On the other hand, splitting EOS into an incompressible part and a term proportional to depth (7.20) and computing derivatives of ρ via harmonic averaging of adiabatic differences (7.26) avoids any noticeable increase of error associated with compressibility (Fig. 16, lower left).

One might suggest that this reduction of error, in comparison with a straightforward computation of PGF using *in situ* ρ, is explained mainly by the effective linearization of compressibility effects in the first-order truncation of (7.20) with $n_{\max} = 1$. To explore this possibility, we made an alternative calculation in which we used the same EOS, $\rho = \rho_1(\theta, S) + q_(\theta, S) \cdot z$ (cf., (7.20) with $n_{\max} = 1$), but now the ρ_1 and $q_1 z$ terms were combined into *in situ* ρ, which is then used in the original Cubic H scheme. The result is shown in Fig. 16, lower right. Although the level of error there is slightly smaller than when using full nonlinear EOS (cf., Fig. 15, lower right), it is closer to it than t is to the results with the split or incompressible EOS (i.e., Fig. 16, lower left, or Fig. 15, lower left). Since the two compressible algorithms here differ only in the computation of ρ derivatives—specifically the choice of the reference gradient considered "neutral" by the monotonicity-enforcement algorithm, (7.27) vs. (5.20)—this indicates

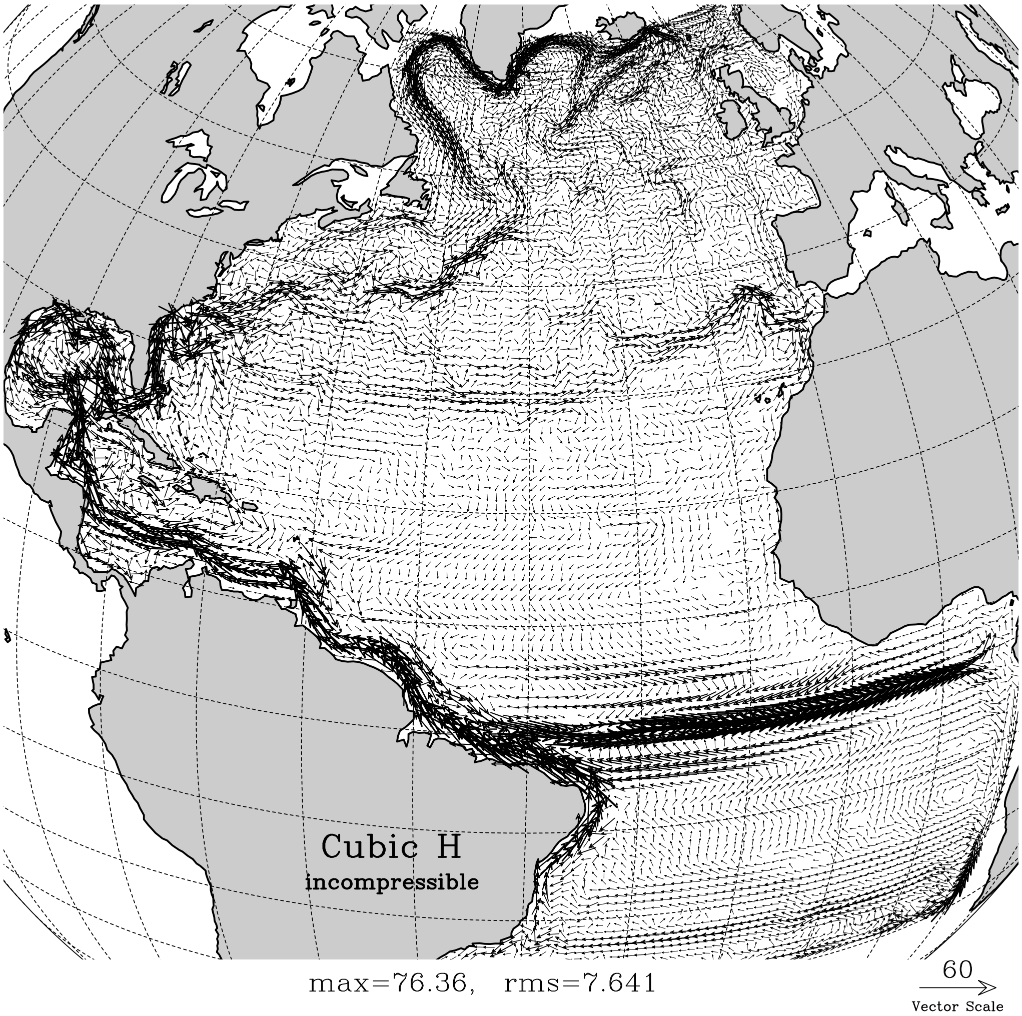

Continuation of Fig. on the previous page: now compressibility terms are turned OFF. Although qualitatively similar in its main features, energetics and maximum values of velocity to the case shown on the left, this solution is characterized by approximately 40% weaker, and prematurely separating, Gulf Stream, and a spurious east-bound current near Azores heading toward the Gibraltar.

that the main influence on the PGF error is this feature, not the linearization of the compressibility terms in EOS. Despite the striking similarity of incompressible Cubic H errors (Fig. 15, lower left) and compressible, split-EOS (7.26), Cubic H errors (Fig. 16, lower left), these two methods actually produce quite different solutions under conditions of realistic temperature, salinity and forcing, where, in addition to small hydrostatic error, the scheme should be accurate in the dynamically relevant PGF. Moreover, we will see that neglecting compressibility results in a completely wrong dynamical response.

Fig. 17 shows six-month averaged, near-surface currents from two different solutions for the Atlantic Ocean under realistic wind stress, heat, and fresh-water flux forcing, starting from a Levitus (θ, S) climatology and running for a three-year spin-up period before the time-averaging begins. The averaging period corresponds to the spring-summer season. Unlike the flat-stratification test problem, where there is no mixing of temperature and salinity, the realistic simulation cannot be made without material diffusion due to both physical and numerical reasons. So in all the realistically forced simulations reported here, fourth-order centered advection is replaced with third-order, upstream-biased advection, but still with no explicit horizontal diffusion. The KPP scheme is used as the parameterization of the vertical mixing processes, Large *et al*, 1994. The first solution uses the modified Cubic H PGF algorithm with harmonic averaging of adiabatic differences (7.26) of ρ and split EOS (7.20) with $n_{\max} = 1$ (i.e., the same combination as for Fig. 16,

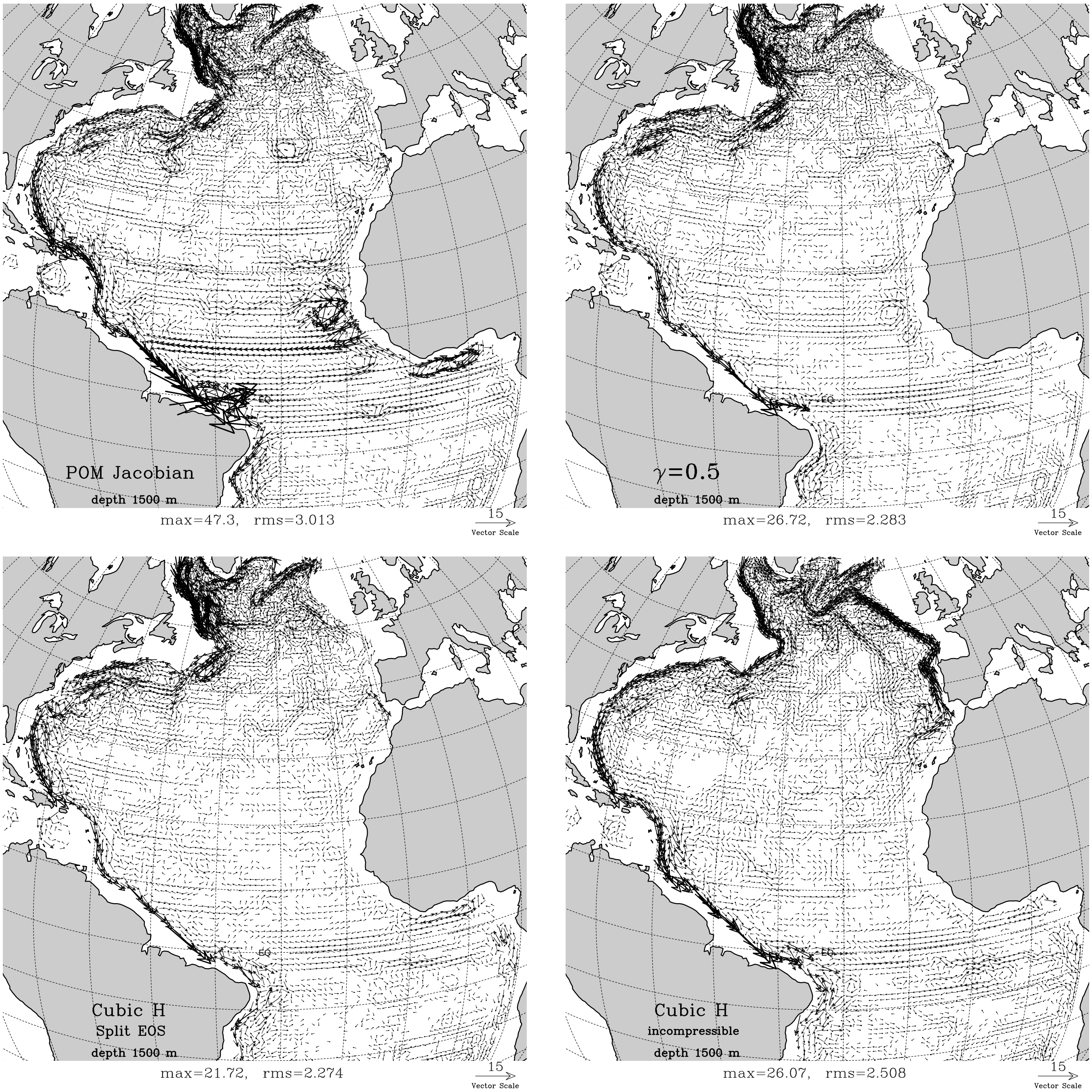

Figure 18. Same as in Fig. 17 , but at depth 1500 m, instead of near-surface, and for four different pressure-gradient algorithms: **top-left** – POM Jacobian ($\gamma = 0$), EOS by (7.14) ; **top-right** – $\gamma = 0.5$, same EOS as on top-left. Note the difference in amplitude of Deep Western Boundary Current (DWBC) off coast of Brazil; **lower-left** – modified *Cubic H*+(7.26) in combination with EOS (7.20) ; **lower-right** – *Cubic H*, compressibility terms turned OFF. Note spurious northward current off coast of Portugal, which continues toward north-west along the topographic slope. This current is due to model response to θ, S of Mediterranean outflow, and is caused by wrong temperature expansion and saline contraction coefficients because of neglect of thermobaric effect. This current is completely absent in the other three solutions. Also note artificially intensified and narrower DWBC in comparison with lower-left panel.

lower left). This combination produces what we consider a physically plausible result in the sense that all primary features—such as correct Gulf Stream separation point—are present and broadly consistent with measurements. The second solution differs from the first one only by turning OFF compressibility terms (the same EOS and PGF combination as in Fig. 15, lower left). Although qualitatively similar in its main features to the first solution, the second solution is characterized by an approximately 40% weaker and prematurely separating Gulf Stream, as well as a spurious eastward current near the Azores heading towards Gibraltar. We do not show the near-surface velocities from two other solutions — $\gamma = 0$ and $\gamma = 0.5$ schemes with EOS (7.14), which retains nonlinear compressibility, but does not contain passive vertical ρ gradient — with the exception of minor differences in Gulf Stream separation site, these are rather similar to the first solution on Fig. 17 and interpreting their differences is not straightforward. On the other hand, comparing the mid-depth currents from all four solutions is more informative since there are larger differences (Fig. 18). Among these solutions the one on the lower-right panel, [Cubic H + incompressible EOS], is anomalous among the others: it has a narrower and more intense Deep Western Boundary Current (DWBC), especially in the Gulf Stream area; a spurious current system off coast of Portugal, which extents towards the northwest; and a northward current along the African coast, which is completely absent on the other three solutions. Examination of temperature and salinity fields (not shown here) reveals that the spurious current off coast of Portugal is due to the response to the Mediterranean outflow[14] combined with erroneous α and β because of neglect of the thermobaric effect. When these two coefficients are correct, the PGF contributions due to temperature and salinity gradients approximately cancel each other, resulting in a very small PGF gradient (as occurs in the other three solutions), hence weak geostrophically balanced currents. In fact, under these conditions (as seen in Appendix B), α may be off by as much as 50%, if its compressibility dependence is neglected. As the simulation continues, the temperature and salinity fields adjust toward a new state, resulting in a different circulation—the narrow jet along the coast of Portugal continuing northwestward. This current advects the Mediterranean water northward along the coast, ultimately maintaining a strong cross-shore gradient, which maintains the current itself in a "self-locking" mechanism. No such current occurs in the solution shown on the right. Instead there is much weaker current going northwestward from Gibraltar, separating from the coast at approximately 38^0N, and heading toward the west. This is the expected behavior from observations, Haidvogel *et al*, 2000. The three remaining solutions—top left, top right, and lower left—are qualitatively similar to each other. This indicates that they are predominantly controlled by the underlying physics, not by their numerical errors, but there are still differences worth pointing out. The most striking distinction is the intensity of DWBC off the Brazilian coast.

POM scheme ($\gamma = 0$) gives approximately twice the peak velocity there and a noticeable increase in the energy (indicated by the increase in rms velocity from approximately 2.3 cm/sec to 3.0 cm/sec). The other two schemes—[Cubic H + (7.26)] and $\gamma = 0.5$—are quite similar by these measures. Comparison of these results with the flat-stratification test (cf., Fig. 15) suggests that a plausible explanation of the difference between $\gamma = 0$ and $\gamma = 0.5$ results in Fig. 18 lies in the hydrostatic PGF error: $\gamma = 0$ produces southward flow near the Brazilian coast in the flat stratification test problem, which is in the same direction as the stronger DWBC on Fig. 15. On the other hand, the hydrostatic error of $\gamma = 0.5$ is opposite to DWBC, which is consistent with its smaller velocities in the realistic forcing experiment. The overall sensitivity of DWBC to the choice of weighting parameter γ is comparable to the differences among the three major classes of models, z-, sigma-, and isopycnic coordinate, Beckmann, 1998, and Willebrand, *et al*, 2001. The DWBC results with [Cubic H + (7.26)] are in between the other two, but closer to $\gamma = 0.5$. Besides the intensity of the DWBC, Fig. 18 shows other differences between $\gamma = 0$ and $\gamma = 0.5$: the appearance of possibly spurious vortex structures off the African coast in the Gulf of Guinea and Canary Islands, as well as the generation of Rossby waves near the Equator manifested by alternating east-west bands in the velocity field, which are tracks of stronger, westward-traveling vortex structures in the case of $\gamma = 0$.

Making a firm conclusion about which of the three solutions is physically the most accurate is beyond the scope of this paper, so we merely point out that the sensitivity of the answers to the choices among the POM Jacobian and $\gamma = 0, ..., 0.5$ in the Song, 1998, family of schemes and the non-robustness of the "optimal" choice of γ in different configurations all motivate the search for higher-order alternatives, such as Cubic H. We also notice that evaluating a PGF scheme solely by its hydrostatic error, (i.e., the flat-stratification test problem) does not necessarily guarantee an accurate simulation in realistic cases. For example, POM Jacobian performs better than $\gamma = 0.5$ in the flat-stratification test shown on Fig. 15; however, $\gamma = 0$ results in the realistic simulation (Fig. 18) has

[14] In this model configuration Mediterranean outflow is simulated by specifying point-sources in the vicinity of Gibraltar Strait, where θ, S are artificially maintained at their climatological values.

some features that seem likely to be spurious.

Our experience also shows that the straightforward inclusion of compressibility in *in situ* ρ calculations for PGF causes a significant increase of hydrostatic PGF error compared to EOS without compressibility. This error results in spurious currents that are the largest near the Equator, due to the diminished Coriolis frequency there. On the other hand, disregarding compressibility completely (motivated by the desire to reduce PGF error) causes significant errors in realistic simulations due to physically wrong responses of the model to temperature and salinity forcing. Our new method for splitting the compressibility terms allows us to obtain physically correct responses without increase of hydrostatic error.

9. Summary

Although PGF errors can be eliminated completely only if isosurfaces of the vertical coordinate are aligned with either geopotential surfaces or isopycnals, these two choices of the vertical coordinate have difficulties in accurately representing the top and bottom boundary conditions. This leaves σ-models as preferred, if accurate topographic and shallow-water, free-surface effects are the highest priority. Therefore, the goal of minimizing PGF errors in σ-models remains important for oceanic modeling.

An analysis of one the more successful PGF schemes to date, the second-order Jacobian, shows that, in addition to approximating the desired terms of the continuous equations with second-order accuracy, it also has important symmetries and can be written in several alternative but equivalent forms. The latter lead to different versions of high-order accuracy generalizations, depending of which form is chosen as the prototype. We find the pseudo-flux form particularly attractive. This gives the possibility of rewriting the Jacobian in the form of a contour integral, and we propose a fourth-order accurate method based on this form. In doing so we preserve the property of the original scheme that treats ρ and z as functions of transformed coordinates in a symmetric, mutually interchangeable way. Our new approach is based on reconstruction of ρ and z as continuous and continuously differentiable polynomial functions of transformed coordinates with subsequent analytical integration. Similarly to its prototype, our new method can be equivalently transformed between Density-Jacobian and σ-coordinate primitive forms. We analyze the causes of previous experience of non-robustness and limited applicability of high-order schemes designed in the past, and we pay special attention to the prevention of the appearance of spurious oscillations of polynomial interpolants in the cases where ρ can no longer be treated as a smooth field on the grid. We also develop special measures to avoid loss of accuracy associated with the use of spatially nonuniform grids that are commonly used in oceanic modeling.

Historically σ-coordinate PGF errors have been attributed mainly to hydrostatic cancellation errors. Thus, the primary focus of many previously proposed schemes has been to address this particular problem while much less attention has been paid to derived conservation properties of the discretized PGF. Our experience shows that it is not entirely the right perspective because as the model's ρ field evolves the actual magnitude of spurious velocities may become very much larger than that determined from geostrophic balance with the erroneous PGF associated with a horizontally uniform initial $\rho(z)$ field. Specifically we observe significant growth of erroneous barotropic flow in a manner previously described as "a σ error of the second kind" (Mellor *et al*, 1998).

Realistic oceanic modeling requires taking into account the compressibility of seawater. Accurate representation of this effect is especially difficult in σ-models, because the straightforward inclusion of compressibility into the EOS causes a large, dynamically passive, background vertical profile of *in situ* ρ associated with compressibility of seawater with uniform temperature and salinity. Although in theory this background profile should not generate any PGF, it is shown to be a major source of PGF error in models due to the combination of the usual numerical noncancellation in the absence of compressibility (σ-error) and the largeness of this passive compressibility effect compared to the stable stratification, particularly in the abyss where vertical resolution is typically very coarse. Furthermore, this background compressibility interferes with non-oscillatory interpolation algorithms because physically neutral stratification is no longer equivalent to the absence of a vertical gradient in ρ. To address these difficulties, we have devised a new treatment of compressibility effects that splits ρ into terms evaluated at atmospheric surface pressure and terms with compressibility, in order to isolate the latter from adding to the PGF error as it does when total ρ is used in the calculation. The new EOS formulation is shown to be sufficiently accurate, compared to the standard EOS formulation, for reliable usage in oceanic models.

Acknowledgements This study was supported by grants N00014-98-1-0165 and N00014-00-1-0249 from the Office of Naval Research. All computations presented here were performed in National Center for Supercomputing Applications (NCSA) sponsored by National Science Foundation.

Appendix A: On Discrete Energetic Consistency of High-Order PGF Schemes

Song & Wright, 1998, (hereafter SW98), show that the second-order equal-weighted[15] density-Jacobian scheme in combination with second-order, centered advection for density guarantees exact conservation of total (kinetic + potential) energy of the discretized system. In this Appendix we show that their derivation can be extended to a more general case where two-point, linear interpolation of ρ in both PGF and advection schemes is replaced with a more general, potentially high-order accurate interpolation. For brevity we present here only discrete equations. Reader should be refered to SW98 for their continuous prototypes.

Since both the original second-order and our new scheme can be rewritten in pseudo-flux form, the x-component of the PGF with sign and scaling as it appears in the r.h.s. of the finite-volume momentum equation for $u_{i+\frac{1}{2},k}$ is

$$PX_{i+\frac{1}{2},k} \equiv -\widetilde{\Delta H}^{x}_{i+\frac{1}{2},k} \left.\frac{\partial p}{\partial x}\right|_{z} = \widetilde{\Delta H}^{x}_{i+\frac{1}{2},k} \sum_{k'=k}^{N} \left(FX_{i,k'+\frac{1}{2}} - FX_{i+1,k'+\frac{1}{2}} + FCX_{i+\frac{1}{2},k'+1} - FCX_{i+\frac{1}{2},k'} \right) \qquad \text{(A.1)}$$

$$= -\widetilde{\Delta H}^{x}_{i+\frac{1}{2},k} \left\{ \delta_x \left. \sum_{k'=k}^{N} FX_{k'+\frac{1}{2}} \right|_{i+\frac{1}{2}} + FCX_{i+\frac{1}{2},k} \right\},$$

where δ_x denotes elementary 2-point differencing over one grid interval, $\delta_x q_{i+\frac{1}{2}} = q_{i+1} - q_i$ and $\delta_x q_i = q_{i+\frac{1}{2}} - q_{i-\frac{1}{2}}$, hence the result is always placed half-way between the points at which the original quantity is defined. For notational simplicity we also assume a Cartesian grid with $\Delta x = \Delta y = 1$, and we omit the factor g/ρ_0 from the definitions of PGF and potential energy below; $\widetilde{\Delta H}^{x}_{i+\frac{1}{2},k}$ denotes height of control volume element surrounding $u_{i+\frac{1}{2},k}$, which in the simplest case can be approximated by second-order mid-point averaging $\widetilde{\Delta H}^{x}_{i+\frac{1}{2},k} = \left(\Delta H_{i,k} + \Delta H_{i+1,k}\right)/2$, but in general it may be done by an arbitrary interpolation scheme, e.g., a fourth-order scheme. In any case $\Delta H_{i,k} = z_{i,k+\frac{1}{2}} - z_{i,k-\frac{1}{2}}$ is vertical spacing of arbitrarily stretched vertical grid, so neither $z_{i,k+\frac{1}{2}} \neq \left(z_{i,k} + z_{i,k+1}\right)/2$ nor $z_{i,k} \neq \left(z_{i,k-\frac{1}{2}} + z_{i,k+\frac{1}{2}}\right)/2$; Further in (A.1) FX and FCX are "pseudo-fluxes" which in the simplest case are computed as

$$FX_{i,k+\frac{1}{2}} = \left.\left(\overline{\rho}^{s}\delta_s z\right)\right|_{i,k+\frac{1}{2}} \qquad \text{and} \qquad FCX_{i+\frac{1}{2},k} = \left.\left(\overline{\rho}^{x}\delta_x z\right)\right|_{i+\frac{1}{2},k}, \qquad \text{(A.2)}$$

where $\overline{\rho}^{s}$ and $\overline{\rho}^{x}$ are mid-point averaged values of density. It is implied that the surface value $FCX_{i+\frac{1}{2},N+1} \equiv 0$ in the first line of (A.1). Model variables are placed on a C-grid and their permissible index ranges and boundary conditions are given by

$$\begin{array}{lllll}
z, \rho_{i,j,k} & i = 1, \ldots, L & j = 1, \ldots, M & k = 1, \ldots, N & \\
u_{i+\frac{1}{2},j,k} & i = 0, \ldots, L & & & u_{\frac{1}{2},j,k} = u_{L+\frac{1}{2},j,k} = 0 \\
v_{i,j+\frac{1}{2},k} & & j = 0, \ldots, M & & v_{i,\frac{1}{2},k} = u_{i,M+\frac{1}{2},k} = 0 \\
\omega_{i,j,k+\frac{1}{2}} & & & k = 0, \ldots, N & \omega_{i,j,\frac{1}{2}} = \omega_{i,j,N+\frac{1}{2}} = 0\,.
\end{array} \qquad \text{(A.3)}$$

After substitution of (A.2) into (A.1), the later becomes equivalent to Eq. (2.6) and, ultimately, (2.22) from SW98, with the exception of the top-most grid interval: it should be noted that Eqs. (2.6), (2.7), (2.22), and (2.25) from SW98 overshoot vertical index inside the summation by requiring values of ρ (b in their notation) and z at vertical index $N+1$ (via $\overline{b}^{s}_{N+\frac{1}{2}}$ and $\delta_s z_{N+\frac{1}{2}}$), which are not available. This means that a special rule for the computation of $FX_{N+\frac{1}{2}}$ is required to fix this problem. We do not specify this rule at this moment, but assume that $PX_{i+\frac{1}{2},N}$ can be still cast in pseudo-flux form[16].

In the following analysis we assume that instead of using (A.2), $FX_{i,k+\frac{1}{2}}$ and $FCX_{i+\frac{1}{2},k}$ are computed by an arbitrary, potentially high-order accurate, interpolation method. Another distinction from SW98 is that we do not

[15] also called *Standard Jacobian* in SW98

[16] Strictly speaking this is not the case for the POM and SCRUM models. Although to our best knowledge, the algorithm for computation of $PX_{i+\frac{1}{2},N}$ has never been published in the literature, it can be easily recovered from the code itself: $PX_{i+\frac{1}{2},N} = -\frac{1}{2} g \widetilde{\Delta H}^{x}_{i+\frac{1}{2},N} \left(\zeta_i - z_{i,N} + \zeta_{i+1} - z_{i+1,N}\right)\left(\rho_{i+1,N} - \rho_{i,N}\right)$, which simply neglects the fact that $\rho_{i+1,N}$ and $\rho_{i,N}$ are placed at different geopotential surfaces. (The finite-difference version of SPEM (v. 5.1) and SCRUM have a similar treatment.) Besides the usual "leak" of vertical stratification into horizontal PGF, this formulation does not provide pseudo-flux continuity between the elements N and $N-1$ of the vertical grid. In the derivation presented here we assume that both these drawbacks are repaired.

restrict ourselves to the case of zero free-surface disturbance, despite the fact that (A.1) does not explicitly contain the free-surface term $PX_{i+\frac{1}{2},\zeta}$, as it occurs in (2.6)–(2.7) from SW98. Below in (A.21)–(A.23) we also show that the free-surface contribution can be naturally cast in flux-difference form of (A.1).

Multiplication of (A.1) by $u_{i+\frac{1}{2},k}$ and summation over all indices i yields,

$$\begin{aligned}\sum_{i=1}^{L-1} \widetilde{\Delta H}^{x}_{i+\frac{1}{2},k} u_{i+\frac{1}{2},k} PX_{i+\frac{1}{2},k} &= \sum_{i=1}^{L-1} \widetilde{\Delta H}^{x}_{i+\frac{1}{2},k} u_{i+\frac{1}{2},k} \left\{ -\delta_x \left(\sum_{k'=k}^{N} FX_{k'+\frac{1}{2}} \right)_{i+\frac{1}{2}} - FCX_{i+\frac{1}{2},k} \right\} \\ &= \sum_{i=1}^{L} \left\{ \delta_x \left(\widetilde{\Delta H}^{x}_{k} u_k \right)\Big|_i \left(\sum_{k'=k}^{N} FX_{i,k'+\frac{1}{2}} \right) \right\} - \sum_{i=1}^{L-1} \widetilde{\Delta H}^{x}_{i+\frac{1}{2},k} u_{i+\frac{1}{2},k} FCX_{i+\frac{1}{2},k} \,,\end{aligned} \tag{A.4}$$

where in order to obtain the second line from the first we have applied summation by parts in a manner similar to the transition from Eq. (2.22) to (2.23) in SW98, where we assume no-flux boundary conditions $u_{\frac{1}{2}} = u_{L+\frac{1}{2}} = 0$, so that the index range in the leftmost sum in the second line can be extended as necessary to include side velocity points (it should be noted that the expressions inside the leftmost sum and its inner sum in the second line are now placed at density point $\rho_{i,k}$ on horizontally staggered C-grid).

After similar manipulation with PY-terms, we derive the contribution of PGF into net kinetic energy tendency,

$$\begin{aligned}\left.\frac{dKE}{dt}\right|_{PGF} &= \sum_{k=1}^{N}\sum_{j=1}^{M}\sum_{i=1}^{L-1} \widetilde{\Delta H}^{x}_{i+\frac{1}{2},j,k} u_{i+\frac{1}{2},j,k} PX_{i+\frac{1}{2},j,k} + \sum_{k=1}^{N}\sum_{j=1}^{M-1}\sum_{i=1}^{L} \widetilde{\Delta H}^{y}_{i,j+\frac{1}{2},k} v_{i,j+\frac{1}{2},k} PY_{i,j+\frac{1}{2},k} \\ &= \sum_{i=1}^{L}\sum_{j=1}^{M}\sum_{k=1}^{N} \left\{ \left[\delta_x \left(\widetilde{\Delta H}^{x}_{k} u_k \right) + \delta_y \left(\widetilde{\Delta H}^{y}_{k} v_k \right) \right]\Big|_i \left(\sum_{k'=k}^{N} FX_{i,k'+\frac{1}{2}} \right) \right\} \\ &- \sum_{i=1}^{L-1}\sum_{j=1}^{M}\sum_{k=1}^{N} \widetilde{\Delta H}^{x}_{i+\frac{1}{2},j,k} u_{i+\frac{1}{2},j,k} FCX_{i+\frac{1}{2},j,k} - \sum_{i=1}^{L}\sum_{j=1}^{M-1}\sum_{k=1}^{N} + \widetilde{\Delta H}^{y}_{i,j+\frac{1}{2},k} v_{i,j+\frac{1}{2},k} FCY_{i,j+\frac{1}{2},k} \,.\end{aligned} \tag{A.5}$$

Applying discrete continuity equation

$$\frac{\partial}{\partial t} \Delta H_{i,j,k} + \delta_x \left(\widetilde{\Delta H}^{x}_{k} u_k \right) + \delta_y \left(\widetilde{\Delta H}^{y}_{k} v_k \right) + \delta_s \omega = 0, \tag{A.6}$$

where $\Delta H_{i,j,k}$ and levels $z_{k+\frac{1}{2}}$ follow evolution of free surface,

$$\frac{\partial z_{k+\frac{1}{2}}}{\partial t} = \frac{h + z_{k+\frac{1}{2}}}{h+\zeta} \cdot \frac{\partial \zeta}{\partial t} \qquad k = 1, \dots, N \,, \qquad z_{\frac{1}{2}} \equiv -h \,, \quad \text{and} \quad z_{N+\frac{1}{2}} \equiv \zeta \,, \tag{A.7}$$

(hence (A.6) should be understood as the definition of vertical velocities $\omega_{i,j,k+\frac{1}{2}}$ as the mass fluxes across *moving* grid-box interfaces $z_{i,j,k+\frac{1}{2}}$), the first term in the r.h.s. of (A.5) may be further rewritten as

$$\begin{aligned}\sum_{k=1}^{N} \left\{ \left(-\frac{\partial}{\partial t} \Delta H_{i,j,k} - \delta_s \omega \right) \left(\sum_{k'=k}^{N} FX_{i,j,k'+\frac{1}{2}} \right) \right\} &= - \sum_{k=1}^{N-1} \left\{ \left(\frac{\partial z_{i,j,k+\frac{1}{2}}}{\partial t} + \omega_{i,j,k+\frac{1}{2}} \right) \left(\sum_{k'=k}^{N} FX_{i,j,k'+\frac{1}{2}} \right.\right. \\ \left.\left. - \sum_{k'=k+1}^{N} FX_{i,j,k'+\frac{1}{2}} \right) \right\} - \frac{\partial z_{i,j,N+\frac{1}{2}}}{\partial t} FX_{i,j,N+\frac{1}{2}} &= - \sum_{k=1}^{N-1} \omega_{i,j,k+\frac{1}{2}} FX_{i,j,k+\frac{1}{2}} - \sum_{k=1}^{N} \frac{\partial z_{i,j,k+\frac{1}{2}}}{\partial t} FX_{i,j,k+\frac{1}{2}} \,.\end{aligned} \tag{A.8}$$

To derive this we have used top and bottom kinematic boundary conditions $\omega_{N+\frac{1}{2}} = \omega_{\frac{1}{2}} = 0$, and $\partial z_{\frac{1}{2}}/\partial t = 0$ [note that $\partial z_{N+\frac{1}{2}}/\partial t \equiv \partial \zeta/\partial t \neq 0$ due to evolving free surface].

The discretized density equation is

$$\frac{\partial}{\partial t} \left(\Delta H_{i,j,k} \rho_{i,j,k} \right) = -\delta_x \left(\widehat{\rho}^{x} \cdot \widetilde{\Delta H}^{x}_{k} u_k \right) - \delta_y \left(\widehat{\rho}^{y} \cdot \widetilde{\Delta H}^{y}_{k} v_k \right) - \delta_s \left(\widehat{\rho}^{s} \cdot \omega \right) \,, \tag{A.9}$$

where $\widehat{\rho}^{x}_{i+\frac{1}{2},j,k}$ the result of mid-point interpolation of ρ (to the location of $u_{i+\frac{1}{2},j,k}$) using an arbitrary interpolation method, which is not necessarily linear and not necessarily the same for all directions x, y, s. Multiplying (A.9) by $z_{i,j,k}$ and applying summation by parts, we derive

$$\sum_{i=1}^{L}\sum_{j=1}^{M}\sum_{k=1}^{N} z_{i,j,k}\frac{\partial}{\partial t}\left(\Delta H_{i,j,k}\rho_{i,j,k}\right) = -\sum_{i=1}^{L}\sum_{j=1}^{M}\sum_{k=1}^{N} z_{i,j,k}\left\{\delta_x\left(\widehat{\rho}^{x}\cdot\widetilde{\Delta H}^{x}_{k}u_k\right)+\delta_y\left(\widehat{\rho}^{y}\cdot\widetilde{\Delta H}^{y}_{k}v_k\right)+\delta_s\left(\widehat{\rho}^{s}\cdot\omega\right)\right\}$$

$$= \sum_{i=1}^{L-1}\sum_{j=1}^{M}\sum_{k=1}^{N}\widehat{\rho}^{x}_{i+\frac{1}{2},j,k}\cdot\widetilde{\Delta H}^{x}_{i+\frac{1}{2},j,k}u_{i+\frac{1}{2},j,k}\delta_x z_{i+\frac{1}{2},j,k} \tag{A.10}$$

$$+\sum_{i=1}^{L}\sum_{j=1}^{M-1}\sum_{k=1}^{N}\widehat{\rho}^{y}_{i,j+\frac{1}{2},k}\cdot\widetilde{\Delta H}^{y}_{i,j+\frac{1}{2},k}v_{i,j+\frac{1}{2},k}\delta_y z_{i,j+\frac{1}{2},k}+\sum_{i=1}^{L}\sum_{j=1}^{M}\sum_{k=1}^{N-1}\widehat{\rho}^{s}_{i,j,k+\frac{1}{2}}\cdot\omega_{i,j,k+\frac{1}{2}}\delta_s z_{i,j,k+\frac{1}{2}}\,.$$

Also note that

$$\sum_{i=1}^{L}\sum_{j=1}^{M}\sum_{k=1}^{N} z_{i,j,k}\frac{\partial}{\partial t}\left(\Delta H_{i,j,k}\rho_{i,j,k}\right) = \underbrace{\frac{\partial}{\partial t}\sum_{i=1}^{L}\sum_{j=1}^{M}\sum_{k=1}^{N} z_{i,j,k}\Delta H_{i,j,k}\rho_{i,j,k}}_{\frac{dPE}{dt}} - \sum_{i=1}^{L}\sum_{j=1}^{M}\sum_{k=1}^{N}\Delta H_{i,j,k}\rho_{i,j,k}\frac{\partial z_{i,j,k}}{\partial t} \tag{A.11}$$

Comparison of (A.10) with (A.5), along with (A.8) and (A.11), indicates that in order to guarantee energetic consistency,

$$\left.\frac{dKE}{dt}\right|_{PGF}+\frac{dPE}{dt}=0\,, \tag{A.12}$$

it is sufficient to ensure that

$$\begin{array}{llll} FX_{i,j,k+\frac{1}{2}} = \widehat{\rho}^{s}_{i,j,k+\frac{1}{2}}\delta_s z_{i,j,k+\frac{1}{2}} & \text{for all} & & k=1,\,\ldots,N-1 \\ FCX_{i+\frac{1}{2},j,k} = \widehat{\rho}^{x}_{i+\frac{1}{2},j,k}\delta_x z_{i+\frac{1}{2},j,k} & \text{everywhere,} & \text{where} & u_{i+\frac{1}{2},j,k}\neq 0 \\ FCY_{i,j+\frac{1}{2},k} = \widehat{\rho}^{y}_{i,j+\frac{1}{2},k}\delta_y z_{i,j+\frac{1}{2},k} & \text{everywhere,} & \text{where} & v_{i,j+\frac{1}{2},k}\neq 0\,, \end{array} \tag{A.13}$$

and

$$-\sum_{k=1}^{N} FX_{i,j,k+\frac{1}{2}}\frac{\partial z_{i,j,k+\frac{1}{2}}}{\partial t}+\sum_{k=1}^{N}\Delta H_{i,j,k}\rho_{i,j,k}\frac{\partial z_{i,j,k}}{\partial t}=0\,, \tag{A.14}$$

which leads to the following set of conclusions:

- Discrete energetic consistency can be shown if: (*i*) discrete PGF scheme can be written in pseudo-flux form; and (*ii*) ρ used in PGF is the same, or linearly related to that in the advection equation; and (*iii*) interpolation algorithms used in computation of pseudo-fluxes FX, FCX, and FCY are the same as corresponding interpolations in discrete advection for density. Details of the vertical coordinate (such as vertical stretching or order of interpolation) to compute $\widetilde{\Delta H}^{x}_{i+\frac{1}{2},j,k}$ from $\Delta H_{i,j,k}$ do not destroy the consistency, as long as the same method is used in continuity, density, and momentum equations.
- The second-order scheme corresponds to the setting of $\widehat{\rho}^{x}_{i+\frac{1}{2},j,k}=\overline{\rho}^{x}_{i+\frac{1}{2},j,k}$ in (A.13) (similarly in other two directions), which is energetically consistent. Alternatively one can chose

  $$\widehat{\rho}_{i+\frac{1}{2},j,k}=-\frac{1}{16}\rho_{i-1,j,k}+\frac{9}{16}\rho_{i,j,k}+\frac{9}{16}\rho_{i+1,j,k}-\frac{1}{16}\rho_{i+2,j,k} \tag{A.15}$$

  or even a more sophisticated method (e.g., using harmonic averaging of elementary slopes to prevent spurious oscillations) and still retain energetic consistency. However, no choice results in fourth-order accuracy for both

PGF and advection. This fundamental limitation stems from the second-order accurate definition of potential energy,

$$PE = \iiint \rho z \, \mathrm{d}x \, \mathrm{d}y \, \mathrm{d}z \approx \sum_{i,j,k} \rho_{i,j,k} \Delta H_{i,j,k} z_{i,j,k} \,. \tag{A.16}$$

- Violation of the pseudo-flux form in the uppermost grid element, common practice of subtracting background profile $\rho = \rho_{\mathrm{bak}}(z)$ from density field before computing PGF (motivated by the desire to reduce hydrostatic errors in PGF) as well as the use of nonlinear (realistic) equation of state of seawater destroy energetic consistency, cf., Gerdes, 1993.

- Since both sums (A.14) are at least second-order discrete approximations to the same continuous integral,

$$\int_{-h}^{\zeta} \rho \frac{\partial z}{\partial t} \mathrm{d}z \tag{A.17}$$

  this equation already holds within the order of accuracy. Assuming[17] that $z_{i,j,k} = \frac{1}{2}\left(z_{i,j,k+\frac{1}{2}} + z_{i,j,k-\frac{1}{2}}\right)$, the second sum in (A.14) may be rewritten as

$$\sum_{k=1}^{N} \Delta H_k \rho_k \frac{\partial z_k}{\partial t} = \sum_{k=1}^{N-1} \frac{\rho_k \Delta H_k + \rho_{k+1} \Delta H_{k+1}}{2} \cdot \frac{\partial z_{k+\frac{1}{2}}}{\partial t} + \frac{1}{2} \rho_N \Delta H_N \frac{\partial z_N}{\partial t} \,, \tag{A.18}$$

  which suggests

$$FX_{k+\frac{1}{2}} = \frac{\rho_k \Delta H_k + \rho_{k+1} \Delta H_{k+1}}{2} \,, \quad k = 1, ..., N-1, \quad \text{and} \quad FX_{N+\frac{1}{2}} = \frac{\rho_N \Delta H_N}{2} \tag{A.19}$$

  to achieve exact cancellation in (A.14). Unless vertical grid spacing is uniform, this choice is different from $FX_{k+\frac{1}{2}} = (\rho_k + \rho_{k+1})(\Delta H_k + \Delta H_{k+1})/4$ used in the original second-order scheme. This discrepancy comes from the fact that definition of discrete potential energy (A.11) corresponds to the assumption of a piecewise-constant distribution of ρ within each vertical grid box ΔH_k, while second-order Jacobian assumes linear profiles between each pair of z_k and z_{k+1}.

Eq. (A.13) does not restrict the algorithm for computation of $FX_{i,j,N+\frac{1}{2}}$ at the uppermost grid point. We therefore propose the following method:

$$\rho^{(\mathrm{surf})} = \rho_N + \frac{\rho_N - \rho_{N-1}}{z_N - z_{N-1}} \left(z_{N+\frac{1}{2}} - z_N\right) \,, \tag{A.20}$$

where $z_{N+\frac{1}{2}} \equiv \zeta$ corresponds to free surface, after which

$$FX_{N+\frac{1}{2}} = \frac{\rho^{(\mathrm{surf})} + \rho_N}{2} \left(z_{N+\frac{1}{2}} - z_N\right) \,, \tag{A.21}$$

and

$$PX_{i,N} = \widetilde{\Delta H}^{x}_{i+\frac{1}{2},N} \left(FX_{i,N+\frac{1}{2}} - FX_{i+1,N+\frac{1}{2}} - FXC_{i+\frac{1}{2},N}\right) \,, \tag{A.22}$$

which repairs the inaccuracy of the original scheme at the top-most grid level (e.g., PGF now vanishes identically everywhere if ρ is a linear function of z). Eq. (A.22) already contains the contribution due to PGF due to free-surface disturbance: e.g., assuming that $FXC_{i+\frac{1}{2},N} = \frac{1}{2}(\rho_{i,N} + \rho_{i+1,N})(z_{i+1,N} - z_{i,N})$ and setting $\rho^{(\mathrm{surf})}_i = \rho^{(\mathrm{surf})}_{i+1} = \rho_{i,N} = \rho_{i+1,N} = \rho_0$ results in

$$PX_{i,N} = \widetilde{\Delta H}^{x}_{i+\frac{1}{2},N} \rho_0 \left(z_{i,N+\frac{1}{2}} - z_{i+1,N+\frac{1}{2}}\right) = \widetilde{\Delta H}^{x}_{i+\frac{1}{2},N} \rho_0 \left(\zeta_i - \zeta_{i+1}\right) \,. \tag{A.23}$$

[17]This choice corresponds to the finite-volume interpretation of non-uniform vertical grid, where $z_{i,j,k\pm\frac{1}{2}}$ are coordinates of grid-boxs interfaces, while $z_{i,j,k}$ are grid-box averaged z.

The usual argument in favor of using an energetically consistent pair of PGF and advection schemes is based on oceanic simulations being typically long-term integrations, so that one can be fearful of accumulation of erroneous energy conversion even when it is within the numerical order of accuracy at each time step. However, the potential energy defined above is computed with respect to a state where all mass is concentrated at $z = 0$, i.e., the unperturbed free surface. This state is not achievable, because PE is defined without taking into account constraints of incompressibility and Lagrangian conservation of density. A more physically meaningful definition of potential energy is *available potential energy* (APE), which respects both these constraints. The main argument behind this concept lies in the fact that as long as fluid parcels are move up and down while maintaining their density, potential energy released in such rearrangement is converted into kinetic energy, and once a state in which each fluid parcel is in hydrostatic equilibrium with its surrounding is achieved, no more potential energy can be released. Although exact Eulerian mass conservation is often imposed in oceanic models, maintaining ρ for each Lagrangian parcel is usually possible only within the numerical accuracy of the advection scheme[18]. This leads to a situation in which an energetically consistent pair does not guarantee the absence of spurious generation of kinetic energy, because numerical advection can alter PE and APE in a nonphysical way (via advective errors), making it available for KE production while maintaining $KE+PE$. This agrees with practical experience to date, where one can modify either PGF or advection independently (thus abandoning exact $KE + PE$ conservation) and observe an overall beneficial outcome for the accuracy of model solution.

Appendix B: Assessment of Taylor Expansion for Seawater Compressibility

To facilitate our analysis we rewrite seawater EOS from Jackett & McDougall, 1995 (hereafter JM95) as

$$\rho_{\text{in situ}}(\theta,S,z) = \frac{\rho_0 + \rho_1'(\theta,S)}{1-0.1z/\left[K_{00}+K'(\theta,S,z)\right]} = \frac{\rho_0}{1-0.1z/K_{00}} + \rho_1' + \frac{0.1z}{K_{00}+K'-0.1z}\left[\rho_1' - \frac{\rho_0 K'}{K_{00}-0.1z}\right], \quad \text{(B.1)}$$

so far without any approximation. Here $\rho_0 = const$, $K_{00} = const$, $K' = K_0' + K_1 z + K_2 z^2$, where $K_0 = K_0(\theta,S)$, $K_1 = K_1(\theta,S)$, $K_2 = K_2(\theta,S)$, as well as $\rho_1' = \rho_1'(\theta,S)$ are expressed in as polynomials of powers of θ, S and $S^{1/2}$; $z > 0$ is depth, which in the context of EOS substitutes for *in situ* pressure $P = \rho_0 g z$ (thus neglecting nonuniformity of ρ field when computing compressibility effects); $\rho_0 = 1000\,\text{kg/m}^3$ is reference density; and $g = 9.81\text{m/s}^2$ is acceleration of gravity. Since $\rho_1' \ll \rho_0 = const$ with an associated small parameter $\rho_1'/\rho_0 \leq 3\times10^{-3}$, and since

$$0.1z\,,\ K_1 z \ll K_0 \equiv K_{00} + K_0'\,, \qquad K_0' \leq K_{00}\,, \quad \text{and} \quad K_2 z^2 \leq K_1 z\,, \quad \text{(B.2)}$$

the r.h.s of (B.1) is dominated by its first term, $\rho_0/(1-0.1z/K_{00})$, which does not contribute to the horizontal PGF, because it is a function of z only. The smallness of the leftmost inequality in (B.2) can be estimated from a typical value speed of sound c of seawater,

$$\frac{1}{c^2} = \left.\frac{\partial\rho}{\partial p}\right|_{\theta,S} = \frac{1}{\rho_0 g}\left.\frac{\partial\rho}{\partial p}\right|_{\theta,S} \approx \frac{1}{\rho_0 g}\cdot\frac{0.1\rho_0}{K_0}\,, \quad \text{hence} \quad \frac{0.1z}{K_0} = \frac{gz}{c^2} = \frac{9.81\cdot 6\times10^3}{1500^2} = 2.5\times10^{-2}\,, \quad \text{(B.3)}$$

where we use $z = 6000$m, and $c = 1500\text{m/s}^2$ for this estimate. The terms $0.1z$ and $K_1 z$ are assumed to be of the same order. The other two inequalities in (B.2) mean that terms proportional to z and z^2 never dominate K_0. Furthermore, $K_0(\theta,S) = K_{00} + K_0'(\theta,S) \approx 19092.6 + 209.8\theta + 104.4S + \ldots$, hence $K_0' \leq K_{00} = const$ in the sense that terms dependent on θ and S never dominate the preceding K_{00}; however, they are not sufficiently small to be used in a Taylor expansion accurate enough for practical purposes. This estimate also explains why removing a background $\rho(z)$ profile, essentially $\rho_0/(1-0.1z/K_{00})$, has only limited success in reducing PGF errors.

Retaining only terms which contribute to horizontal PGF and using the two small parameters identified above, the Taylor series expansion of (B.1) results in

$$\rho(\theta,S,z) = \rho_1' + 0.1\frac{\rho_1' - \rho_0 K_0'/K_{00}}{K_{00}+K_0'}z - 0.1(\rho_0+\rho_1')\frac{K_1 - 0.1}{(K_{00}+K_0')^2}z^2 + \mathcal{O}\left(\left(\frac{z}{K_0}\right)^3\right) = \rho_1' + q_1 z + q_2 z^2\,, \quad \text{(B.4)}$$

[18]With the exception of isopycnic-coordinate models, where it can be done exactly by conserving the volume of each isopycnal layer.

which has a form appropriate for computation of PGF, cf., (7.20). As follows from (7.15)–(7.17), for accurate computation of horizontal ρ and PGF, it is sufficient that EOS produces correct estimate for temperature-expansion α and saline-contraction β coefficients, while *in situ* ρ is irrelevant for this purpose. Therefore, to assess possible errors associated with the use of (B.4), we compare the α and β it produces with the original coefficients produced by the EOS from JM95.

Properties of the original EOS from JM95 are illustrated in Fig. 19, where $\rho_{\text{in situ}}$, α, and β are plotted as function of potential temperature θ and salinity S at four different depths $z = 0$. There is overall increase of $\rho_{\text{in situ}}$ with depth z, and in addition to that, there is change in slope of isopycnals with depth on the left column in Fig. 19, which is primary due to the thermobaric effect. There is a local maximum of freshwater ρ at $\theta = 4^0C$, $z = 0$, which shifts to smaller temperature and eventually disappears with increase of P (depth). Middle column shows a significant dependency of α on depth; e.g., for $\theta = 5^0C$ and $S = 33^0/_{00}$, α changes from 0.1 to 0.25 when z goes from 0 to 6000 m. β is more uniform in θ, S-space, with the exception of the limit of low salinity, and it has a relatively weak dependency on depth. As follows from Fig. 19, disregarding the thermobaric effect completely, hence using just $\rho'_1(\theta, S)$ for computation of PGF, results in an underestimate of the ρ gradient in the abyss by as much as 60%. Therefore, one needs to retain terms linear and perhaps quadratic in z in (B.4). In both approximations the resulting α and β are quite close to their values produced by EOS from JM95; so, we show only deviations of α and β from the original ones in Fig. 20. The errors are quite significant within the whole range of possible values of θ and S, especially at maximum depth z=6000m and in the limit of largest temperature and small salinity (right-bottom corner of each plot). Indeed, errors in α may be as large as 30%, while errors in β about 15%. Fortunately in realistic oceanographic conditions temperature has a tendency to decrease with depth, resulting in a much smaller range of possible values, and a similar tendency occurs in salinity field. This fact is reflected by the dashed rectangle on each plot in Fig. 20, which outlines the *domain of relevance*, meaning that nearly all realistic combinations of θ, S should occur within it, and which shrinks with depth. Within this rectangle the errors are much smaller, and, remarkably, its location coincides with the area of minimal errors. The ranges of errors in α and β for θ, S within the domain of relevance are summarized in the following table:

EOS	$\rho' + q_1 z$		$\rho' + q_1 z + q_2 z^2$	
depth	error in α	error in β	error in α	error in β
1000	-0.0026 ... -0.0008	+0.0004 ... +0.0012	-0.003 ... -0.001	+0.0004 ... 0.0012
2500	-0.0040 ... +0.0005	0.0 ... +0.003	-0.007 ... -0.003	+0.002 ... +0.001
5000	-0.008 ... +0.007	-0.008 ... -0.006	-0.005 ... -0.015	-0.004 ... 0.0

This means that, at a maximum depth of z=5000m, given characteristic values of $\alpha = 0.25$ and $\beta = 0.8$, the errors do not exceed 3% for α and 3% for β for linear truncation and slightly less for quadratic. These estimates can be viewed as the worst-case realistic scenario, and, as seen from the table above, the errors are much smaller within the upper 2500 m, which is dynamically the most active part of the ocean. Both truncations provide viable approximations for EOS and offer significant reduction of errors in comparison with neglecting compressibility completely; however, the quadratic version offers no significant improvement to justify its extra complexity .

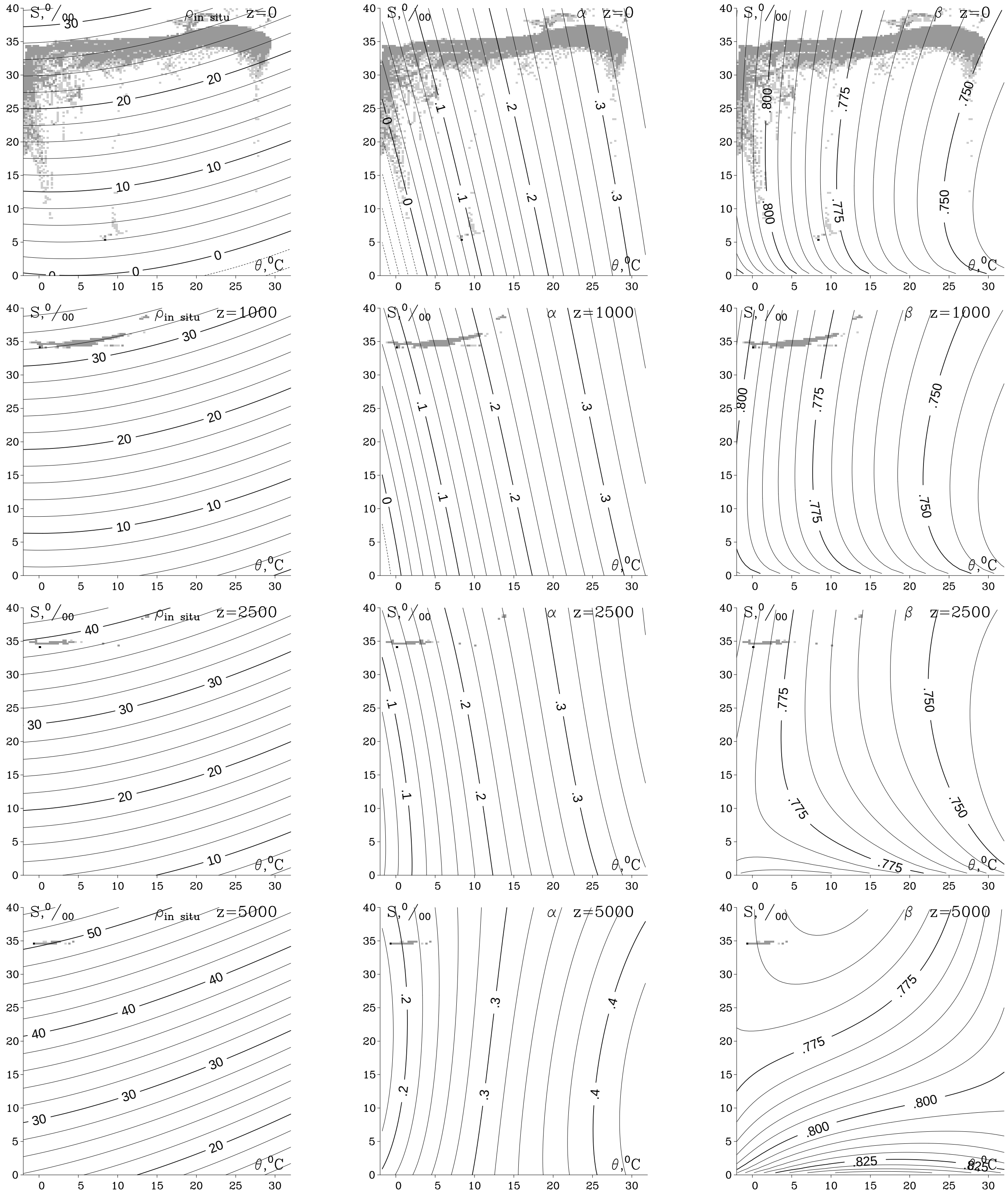

Figure 19. Density *in situ* ρ **(left)**, thermal expansion α **(middle)** and saline contraction coefficient β **(right)** as functions of potential temperature θ and salinity S at four different depths z = 0, 1000, 3000 and 6000 m. Light shading indicates availability (at least one record) of water with given temperature and salinity at each specified depth from annual database for World Ocean, Levitus 1994, while dark shading correspongs to the area containing at least 90% of all data at specified depth. Thermobaric effect is manifested by the change of angle of isopycnals with depth on $\rho\,(\theta, S)$ plot, left column.

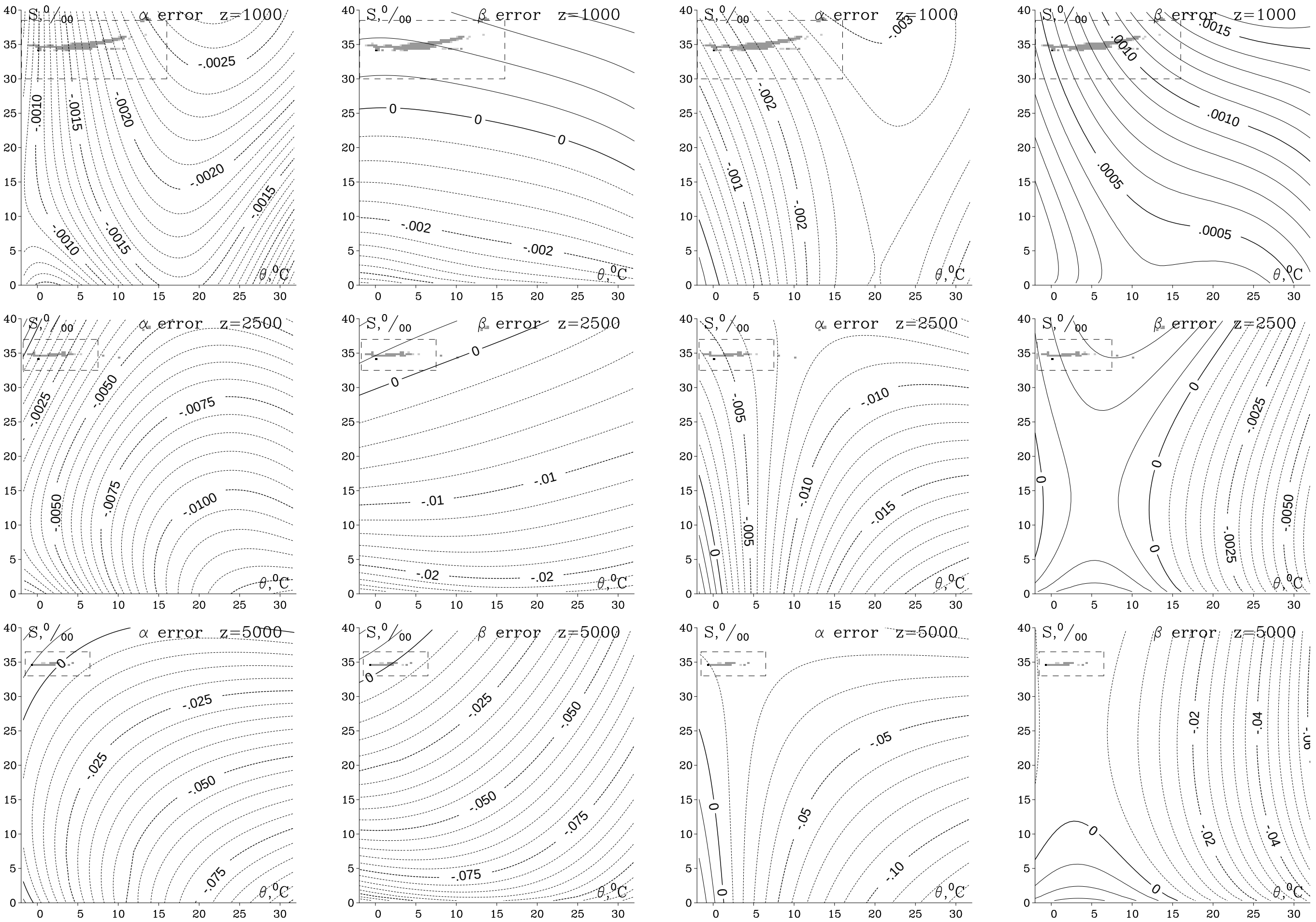

Figure 20. Errors in evaluation of thermal expansion α and salinity contaction β at three different depths, $z = 1000$, 3000, and 6000 m for linear **(left two columns)** and quadratic **(right two columns)** truncations of z-series of EOS from JM95. Errors are definded as deviations of α and β from their values computed form the original EOS (see Fig. on the previous page), which are considered as "exact" in this comparison. Dashed rectangle on each plot shows the *domain of relevance*, meaning that for realistic oceanographic conditions θ and S can occur only within this rectangle at each depth z.

References

Arakawa, A., and M. J. Suarez, 1983, Vertical differencing of the primitive equations in sigma coordinates. *Monthly Weather Review*, **111**, 34-45.

Beckmann, A., and D. B. Haidvogel, 1993: Numerical simulation of flow around a tall isolated seamount. Part. 1: Problem formulation and model accuracy. *Journ. Phys. Ocean.*, **23**, 1736-1753.

Beckmann, A., and D. B. Haidvogel, 1997: A numerical simulation of flow at Fieberling Guyot. *Journ. Geophys. Res.*, **102**, 5595-5613.

Beckmann, A., 1998: The representation of bottom boundary layer processes in numerical ocean circulation models. in *Ocean modeling and Parametrization*, E. P. Chassignet & J. Verron, editors. *Kluwer Acad. Pub.*, pp. 135-154.

Blumberg, A. F. and G. L. Mellor, 1987: A description of a three-dimensional coastal ocean circulation model. In *Three-dimensional Coastal Ocean Models*, ed. N. Heaps (Pub. AGU), pp. 1-16.

Chu, P. C. and C. Fan, 1997: Sixth-order difference scheme for sigma coordinate ocean models. *Journ. Phys. Ocean.*, **27**, 2064-2071.

Chu, P. C. and C. Fan, 1998: A three-point combined compact difference scheme. *Journ. Comp. Phys.*, **140**, 370-399.

Dukowicz, J. K., 2001: Reduction of density and pressure gradient errors in ocean simulations. *Journ. Phys. Ocean.*, **31**, 1915-1921.

Gary, J. M., 1973: Estimate of truncation error in transformed coordinate primitive equation atmospheric models. *Journ. Atmosph. Sci.*, **30**, 223-233.

Gerdes, R., 1993: A primitive equation ocean circulation model using a general vertical coordinate transfornmation. 1. Description

Haidvogel, D. B., H. Arango, K. Hedstrom, A. Beckmann, P. Rizzoli and A. F. Shchepetkin, 2000: Model evaluation experiments in the North Atlantic Basin: Simulations in non-linear terrain-following coordinates. *Dyn. Atmos. Oceans*, **32**, 239-281.

Haidvogel, D. B., A. Beckmann, D. C. Chapman, and R.-Q. Lin, 1993: Numerical simulation of flow around a tall isolated seamount: Part II: Resonant generation of trapped waves. *Journ. Phys. Ocean.*, **23**, 2373-3291.

Haidvogel, D. B., and A. Beckmann, 1999: Numerical Ocean Modeling. *Imperical College Press.*, London, 330 pages.

Haney, R. L., 1991: On the pressure gradient force over steep topography in sigma coordinate ocean models. *Journ. Phys. Ocean.*, **21**, 610-618.

Jackett, D. R. and T. J. McDougall, 1995: Minimal Adjustment of Hydrostatic Profiles to Achieve Static Stability. *Journ. Atmos. Oceanic Technology*, **12**, 381-389.

Janjic, Z. I., 1977: Pressure gradient force and advection scheme used for forecasting with steep and small scale topography. *Contrib. Atmos. Phys.*, **50**, 186–199.

Janjic, T., 1998: Comments on "A finite volume integration method for computing pressure gradient force in general vertical coordinates", *Q. J. R. Meteorol. Soc.,*, **124**, 2527–2529.

Kliem, N., and J. D. Pietrzak, 1999: On the pressure gradient errors in sigma coordinate ocean models: A comparison with laboratory experiments. *Journ. Geophys. Res.*, **104**, 29,781-29,799.

Large, W. G., J. C. McWilliams, and S. C. Doney, 1994: Oceanic vertical mixing: A review and a model with a nonlocal boundary layer parametrization. *Reviews Geophys.*, **32,4**, 363-403.

Leer, van B., 1977: Towards the Ultimate Conservative Difference Scheme III. Upstream-centered Finite-Difference Schemes for Ideal Compressible Flow. *Journ. Comp. Phys.*, **23**, 263-275.

Lin, Shian-Jiann, 1997: A finite volume integration method for computing pressure gradient force in general vertical coordinates. *Q. J. R. Meteorol. Soc.,*, **123**, 1749-1762.

Lin, Shian-Jiann, 1998: Reply to comments by T. Janjic on "A finite volume integration method for computing pressure gradient force in general vertical coordinates", *Q. J. R. Meteorol. Soc.,*, **124**, 2531–2533.

Mahrer, Y., 1984: An improved numerical approximation of the horizontal pressure gradients in a terrain-following coordinate system. *Monthly Weather Review*, **112**, 918-922

McCalpin, J. D., 1994: A comparison of second-order and fourth-order pressure gradient algorithms in a σ-coordinate ocean model. *Int. J. of Num. Meth. in Fluids*, **18** , 361-383.

Mellor, G. L., 1991: An equation of state for munerical models and estuaries. *Journ. Atmos. Oceanic Technology*, **1991**, 609-611.

Mellor, G. L., T. Ezer and L.-Y. Oey, 1994: The pressure gradient conundrum of sigma coordinate ocean models. *Journ. Atmos. Oceanic Technology*, **1994**, 1126-1134.

Mellor, G. L., L.-Y. Oey, and T. Ezer, 1998: Sigma coordinate pressure gradient errors and the seamount problem. *Journ. Atmos. Oceanic Technology*, **15**, 1122-1131.

Mesinger, F., and A. Arakawa, 1976: Numerical Methods used in atmospheric models, Vol. 1, GARP Publ. Ser. 17., World Meteor. Org., 64 pp.

Mesinger, F., 1982: On the convergence and error problems of the calculation of the pressure gradient force in sigma coordinate ocean models. *Geophys. Astrophys. Fluid Dyn.*, **19**, 105-117.

Mesinger, F. and Z. I. Janjic, 1985: Problems and numerical methods of the incorporation of mountains in atmospheric models. *Lect. Appl. Math.*, **22**, 81-120.

Michailovic, D. T., and Z. I. Janjic, 1986: Comparison of methods for reducing the error of the pressure gradient force in sigma-coordinate models. *Meteorol. Atmos. Phys.*, **35**, 177-184.

Millero, F. J., C.-T. Chen, A. Bradshaw, and K. Schleicher, 1980: A new high-pressure equation of state for seawater. *Deep-Sea Res.*, **27A**, 255-264.

Shchepetkin, A. F. and J. J. O'Brien, 1996: A Physically Consistent Formulation of Lateral Friction in Shallow Water Equation Ocean Models. *Monthly Weather Review*, **124**, 1285-1298.

Slordal, L. H., 1997: The pressure gradient force in sigma coordinate ocean models. *Int. J. of Num. Meth. in Fluids*, **24** , 987-1017.

Song, Y. T. and D. Haidvogel, 1994: A Semi-implicit ocean circullation model using a generalized topography following coordinate system, *Journ. Comp. Phys.*, **115**, 228-248.

Song, Y. T. 1998: A General Pressure Gradient Formulation for Ocean Models. Part I: Scheme Design and Diagnostic Analysis, *Monthly Weather Review*, **126**, 3213-3230

Song, Y. T. and D. G. Wright, 1998: A General Pressure Gradient Formulation for Ocean Models. Part II: Energy, Momentum and Bottom Torque Consistency, *Monthly Weather Review*, **126**, 3213-3230

Sun, S., R. Bleck, C. Rooth, J. Dukowicz, E. Cassignet, and P. Killworth, 1999: Inclusion of Thermobaricity in Isopycnic-Coordinate Ocean Models. *Journ. Phys. Ocean.*, **29**, 2719-2729.

Stelling, G. S., and J. A. Th. van Kester, 1994: On the approximation of horizontal gradients in sigma coordinates for bathymetry with steep bottom slopes. *Int. J. of Num. Meth. in Fluids*, **18** , 915-935.

Treguier, A. M., J. K. Dukowicz, and K. Bryan, 1996: Properties of nonuniform grids used in ocean general circullation ocean models. *Journ. Geophys. Res.*, **101**, 20877-20881.

Willebrand, J., B. Barnier, C. Böning, C. Dieterich, P.D. Killworth, C. LeProvost, Y. Jia, J.-M. Molines, A.L. New, 2001: Circulation characteristics in three eddy-permitting models of the North Atlantic. *Progress in Oceanography*, **48**, pp. 123-161.

This preprint was prepared with the AGU LaTeX macros v3.1. File pgf2 formatted 2003 March 26.